Velocity Characteristics in the Wake of an Oscillating Cylinder

by

Joshua Tolford Davis

B.S. Ocean Engineering
Florida Institute of Technology, 1999

Submitted to the Department of Ocean Engineering, MIT
in partial fulfillment of the requirements for the degree of

Master of Science in Ocean Engineering

at the

MASSACHUSETTS INSTITUTE OF TECHNOLOGY

September 2001

Author .....
Department of Ocean Engineering, MIT
August 10, 2001

Certified by .....
Michael S. Triantafyllou
Professor, Department of Ocean Engineering, MIT
Thesis Supervisor

Accepted by .....
Henrik Schmidt
Chairman, Department Committee on Graduate Students

Velocity Characteristics in the Wake of an Oscillating Cylinder

by

Joshua Tolford Davis

Submitted to the Department of Ocean Engineering, MIT
on August 10, 2001, in partial fulfillment of the
requirements for the degree of
Master of Science in Ocean Engineering

Abstract

This thesis describes the results of over 2000 experimental runs conduced at the MIT Ship Model Testing Tank. A rake of constant temperature anemometers is employed to study the spanwise velocity correlation and the vertical velocity profile downstream of a vibrating cylinder. Experiments involve either free vibration implemented through a force feedback system or forced sinusoidal motion. All experiments are conducted at a towing speed within the subcritical flow regime at $Re \approx 3 \times 10^4$. This thesis explores the connection between these downstream velocity properties and the vortex-induced vibrations of the cylinder. In addition to downstream velocities, experimental data include lift and drag forces and cylinder displacement. Vortices are found to be correlated along the entire length of the test cylinder only within a specific band of motion amplitudes and frequencies. Overall, forced oscillations produce vortices that are more organized and well correlated than those shed from a freely vibrating cylinder.

Thesis Supervisor: Michael S. Triantafyllou
Title: Professor, Department of Ocean Engineering, MIT

Acknowledgments

Foremost, I thank my parents, grandparents, aunts, and uncles for believing in all of my endeavors since the kindergarten science fair.

This thesis would not be possible without the tremendous support and direction of Professor Michael Triantafyllou and Dr. Franz Hover.

I owe a debt of gratitude to the machining wizardry of Fred Cote, existent in every piece of experimental hardware.

Ultra thanks go to Dominique Jeudy, Thalia Garalis, and the rest of the people that keep the Ocean Engineering department together.

Many thanks go to my fellow towtankers, including David Beal, Craig Martin, Anna Pauline Miranda Michel, Michael Sachinis, Jennifer Tam Lin, Professor Alexandra Techet, Muriel Thomas, and Albert Wu. Thank you for answering my daily barrage of stupid questions and for not voting me off the island. Of course, the towtank would not be the same without our Europeans: Andrin Landolt from ETHZ and Øyvind Haugsdal and Harald Tvelt from NTNU.

I could not have performed this study without the assistance of undergraduate researchers Marcus Dos Santos, Marisa Kirshbaum, Malima Wolf, Karl-Magnus McLetchie, Angus Kai McDonald, John Dise III, Mercedes Castelo, and Daniel Sura.

In memory of Robert Nesta Marley.

Contents

List of Figures

List of Tables

Chapter 1

Introduction

1.1 Vortex-Induced Vibrations of Bluff Bodies

Modern engineering practices often delegate the use of bluff, mainly cylindrical, bodies as primary structural elements. A bluff body is any structure that causes an incident flow to separate over a large section of that struture's surface [1]. Structures such as power transmission lines, offshore oil rig risers and moorings, and smokestacks are typically long, slender, cylindrical bodies that are subject to a transverse fluid current. In these situations, vortices develop on the structure's surface and are eventually shed into the downstream region. Over multiple cycles, this shedding phenomenon imparts alternating forces to the structure. The resulting vibratory response is termed *vortex-induced vibration*, or VIV. Because it increases fatigue loading, VIV can surreptitiously lead to premature failure of a structure. This chapter defines the relevant nondimensional parameters, describes the fundamentals of VIV theory, and describes previous research investigating the implications of downstream velocity correlation to this phenomenon.

1.1.1 Nondimensional Parameters

Several nondimensional parameters are necessary for discussion of VIV. This section defines and introduces all parameters referred to in this thesis. These definitions are

developed primarily from the texts by Blevins [1] and Newman [14].

Geometry

Mass Ratio The mass ratio is the ratio of the structure's mass to its displacement.

$$m^* = \frac{m}{\rho D^2 L} \tag{1.1}$$

where m is the mass of the structure, ρ is the fluid density, D is the characteristic diameter, and L is the characteristic length of the structure. It should be noted that this definition for mass ratio differs from others that consider added mass to be part of the structure's mass. This difference arises because the mass ratio discussed herein results from a virtual mass created through computer simulation.

Aspect Ratio The aspect ratio is the ratio of the structure's characteristic length to its characteristic diameter. It is an important factor in comparing the geometry of model tests to that of full-scale installations.

$$AR = \frac{L}{D} \tag{1.2}$$

Amplitude Ratio In the case of a vibrating structure, we normalize the zero-to-peak vibration amplitude by the structure's characteristic diameter to create the amplitude ratio.

$$\frac{A}{D} = \frac{vibration\ amplitude}{diameter} \tag{1.3}$$

where the vibration amplitude is the zero-to-peak amplitude.

Wake Position In describing characteristics of a structure's fluid wake, it is important to know the whereabouts of the point of inquiry; i.e. where a probe is located. The inline or streamwise position is normalized by the structure's diameter to yield the parameter $\frac{x}{D}$. Distance is measured from the centroid or central axis of the

structure.

$$\frac{x}{D} = \frac{downstream\ distance\ from\ centroid}{diameter} \tag{1.4}$$

$\frac{x}{D}$ is positive in the downstream direction.

The nondimensional lateral or transverse ($\frac{y}{D}$) and longitudinal or spanwise ($\frac{z}{D}$) positions are defined similarly.

$$\frac{y}{D} = \frac{vertical\ distance\ from\ centroid}{diamter} \tag{1.5}$$

$\frac{y}{D}$ is positive in the upward direction and negative in the downward direction.

$$\frac{z}{D} = \frac{longitudinal\ distance\ from\ centroid}{diameter} \tag{1.6}$$

When viewing a structure from an upstream location, $\frac{z}{D}$ is positive both to the right and left of the centroid. Figure 1-1 illustrates this coordinate system for a cylinder. Furthermore, these definitions can be extended to describe the separation of two points. For instance, $\frac{\Delta z}{D}$ defines the spacing of two points in the longitudinal direction.

$$\frac{\Delta z}{D} = \frac{spanwise\ separation}{diameter} \tag{1.7}$$

The values of these nondimensional separations are always positive.

N.B. In the case of a vibrating cylinder, all positions are measured from the mean location.

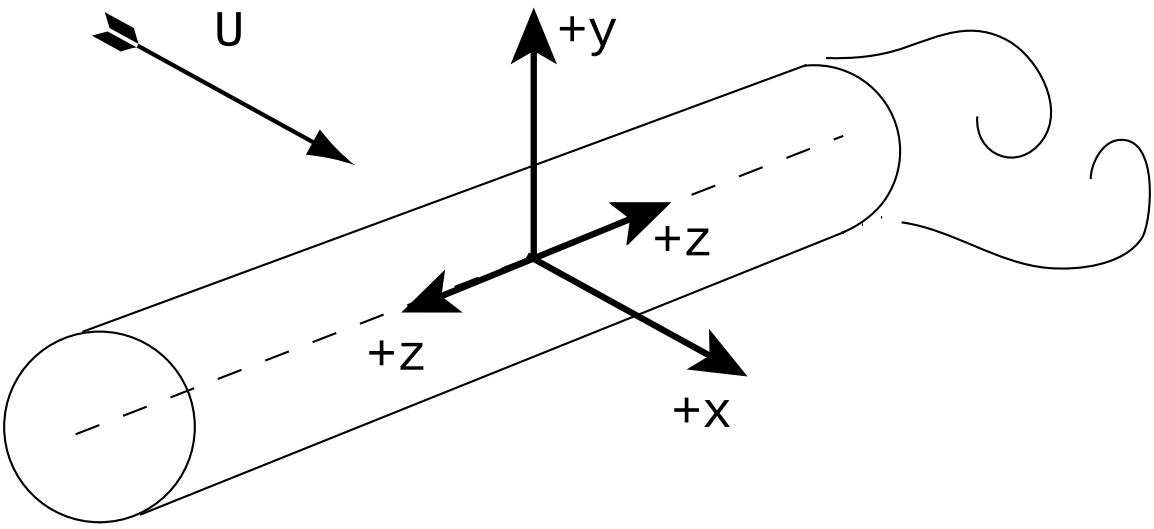

Figure 1-1: The cylinder coordinate system

Fluid-Structure Interaction

Reynolds Number The Reynolds number is an important number in describing the turbulence of the fluid boundary layer near the structure's surface. Roughly speaking, the Reynolds number is the ratio of inertial force to viscous force.

$$Re = \frac{UD}{\nu} \tag{1.8}$$

where U is the incident flow velocity and ν is the kinematic viscosity of the fluid. In the case of a cylinder, the flow is seen to separate at Reynolds numbers greater than 5. Within the subcritical regime ($5 < Re < 3 \times 10^5$), the flow in the boundary layer is considered to be laminar. At Reynolds numbers greater than the critical value of 3×10^5 (postcritical regime), the boundary layer flow is turbulent.

Reduced Velocity To nondimensionalize velocity, we normalize by the ratio of diameter to oscillation period to obtain the reduced velocity.

$$V_r = \frac{UT}{D} = \frac{2\pi U}{\omega_o D} \tag{1.9}$$

where T is the period of one oscillation of a vibrating structure and ω_o is the circular frequency of this oscillation. Furthermore, the reduced nominal velocity, a function of natural frequency rather than oscillation frequency, is another useful parameter.

$$V_{rn} = \frac{2\pi U}{\omega_n D} \tag{1.10}$$

where ω_n is the circular undamped natural frequency of the structure. For the purposes of this thesis, the natural frequency is defined in air.

Keulegan-Carpenter Number In oscillatory flows, such as wave action, the Keulegan-Carpenter number is an appropriate analogue to reduced velocity.

$$KC = \frac{2\pi U_m}{\omega_f D} \tag{1.11}$$

where ω_f is the circular frequency of flow oscillation and U_m is the maximum velocity incident on the cylinder during oscillation.

Strouhal Number The Strouhal number serves as a constant of proportionality relating the cylinder geometry, the incident velocity, and the vortex shedding frequency.

$$S = \frac{\omega_s D}{2\pi U} \tag{1.12}$$

where ω_s is the circular vortex shedding frequency. Strouhal number is primarily a function of Reynolds number. This relationship is further described in Section 1.1.2.

Forces

Drag Coefficient The drag force is defined as the force experienced by the structure in the same direction of the flow. The drag coefficient normalizes this force by the dynamic pressure.

$$C_D = \frac{F_D}{\frac{1}{2}\rho D U^2 L} \tag{1.13}$$

where F_D is the drag force imparted to the structure.

Lift Coefficient As with the drag coefficient, the lift coefficient results from normalization of the lift force by the dynamic pressure.

$$C_L = \frac{F_L}{\frac{1}{2}\rho D U^2 L} \tag{1.14}$$

where F_L is the lift force, or fluid-induced force acting transversely to the flow. However, as a structure begins to vibrate in this transverse direction, the lift force is split into a term in phase with the structure's velocity and a term in phase with the structure's acceleration. Thus, the development of two other lift coefficients is necessary. C_{LA} is the lift coefficient in phase with acceleration and C_{LV} is the lift coefficient in phase with velocity. Both of these parameters are functions of ϕ, the phase angle

between the lift force and the structure's motion.

$$C_{LA} = \frac{F_L \cos(\phi)}{\frac{1}{2}\rho D U^2 L} \tag{1.15}$$

$$C_{LV} = \frac{F_L \sin(\phi)}{\frac{1}{2}\rho D U^2 L} \tag{1.16}$$

Furthermore, these parameters are useful in describing the dynamics of the fluid-structure interaction. If C_{LV} is positive, energy is transferred from the fluid to the structure; resulting in excitation. However, if C_{LV} is negative, energy is transferred from the structure to the fluid; resulting in damping. Because the lift force in phase with acceleration is akin to the added mass, negative values of C_{LA} indicate a positive added mass. Gopalkrishnan [4] provides a detailed derivation of these parameters.

Damping Factor Both the structural and hydrodynamic damping of an element plays an important part in determining its VIV response. The damping factor (ζ), or fraction of the critical damping, provides a measure of the total damping.

$$\zeta = \frac{b}{2m\omega_n} \tag{1.17}$$

where b is the viscous damping coefficient of the system. If we assume the structural damping to be negligible as compared to the fluid damping, an estimated damping factor can be derived in terms of VIV parameters by equating the system dynamics with the hydrodynamic forces.

$$\zeta = \frac{C_{LV} U^2}{\pi D m^* A \omega_n \omega_o} \tag{1.18}$$

using (1.10) and assuming the condition when $\omega_o = \omega_n$,

$$\zeta = \frac{C_{LV} V_{rn}^2}{4\pi^3 m^* \frac{A}{D}} \tag{1.19}$$

Added Mass For the purposes of this analysis, the added mass represents the fluid displaced by a moving body. This entrained fluid is included in the effective dynamic

mass of the cylinder. The added mass coefficient, C_M, normalizes this mass by the volume of water displaced by the body.

$$C_M = \frac{m_a}{\frac{\pi}{4}\rho D^2 L} \tag{1.20}$$

where m_a is the mass of entrained fluid. The equations of added mass coefficient and coefficient of lift in phase with acceleration can be equated through Newton's second law

$$F = ma \tag{1.21}$$

and computing the maximum acceleration, a, through the equation

$$a = A\omega_o^2 \tag{1.22}$$

to yield the following equation for the coefficient of added mass

$$C_M = \frac{-2C_{LA}U^2}{\pi\omega_o^2 D^2 \frac{A}{D}} \tag{1.23}$$

Correlation

Correlation Coefficient The correlation coefficient, R, is used to describe the similarity of two signals. A coefficient magnitude of unity means the signals are identical, and a magnitude of zero means the signals are entirely dissimilar [11].

$$R_{ij} = \frac{C_{ij}}{\sqrt{C_{ii}C_{jj}}} \tag{1.24}$$

where i and j represent the two signals being considered and C is the covariance. For example, the definition of the covariance of signals i and j is

$$C_{ij} = E[(i - \mu_i)(j - \mu_j)] \tag{1.25}$$

where E is the mathematical expectation and $\mu_i = E[i]$. Unless otherwise stated, "correlation" refers to the degree of correlation between two *velocity* sensors. F_C refers to the correlation coefficient taken between the lift forces on either end of the cylinder.

1.1.2 Theoretical Background

Origins of vortex shedding

Potential (inviscid, irrotational) flow theory predicts that a cylinder placed in a steady current will experience maximum pressure at the leading and trailing edges. These two points, where the nearby fluid velocity is zero, are defined as the *stagnation points*. [14]. The maximum fluid velocity and minimum pressure on the cylinder's surface occur at the *shoulder*, or points $\pm 90^\circ$ from the stagnation points. Thus, potential flow predicts a symmetric, unseparated flow around the cylinder.

However, in the physical world, the influence of viscosity is significant. Viscous flow imposes a "no-slip" boundary condition; where the fluid velocity is zero on the surface of the cylinder. This condition results in a boundary layer where the fluid velocity increases from zero to that of the free stream as distance from the cylinder surface is increased. Furthermore, an external pressure gradient, when present, drives and shapes the boundary layer [23]. Two pressure gradients exist for a cylinder in uniform flow: a favorable or decreasing gradient between the leading stagnation point and the shoulder and an adverse or increasing gradient between the shoulder and the trailing stagnation point.

Figure 1-2 illustrates how the boundary layer is sequentially affected by the pressure gradient around a cylinder. Figure 1-2(a) shows the boundary layer profile for the favorable pressure gradient on the leading face of the cylinder. As the flow approaches the shoulder, the pressure gradient is equalized (Figure 1-2(b)). The adverse pressure gradient begins to affect the boundary layer on the trailing face of the cylinder. At some critical point, the fluid shear at the surface of the cylinder reaches zero (Figure 1-2(d)). This event marks the onset of separation, and its location is defined as the

separation point. As the flow further approaches the trailing stagnation point, the adverse pressure gradient can cause backflow in the lower boundary layer; causing the main flow to separate from the surface (Figure 1-2(e)). From the separation points on each side of the cylinder, two shear layers form and bound a turbulent region termed the wake [1]. The fluid velocity within the wake is significantly less that that of the external free stream. This inconsistency causes rotation in the fluid and eventually leads to the development of discrete vortices. It is the pressure disturbances created by these vortices that lead to vortex-induced vibration (VIV).

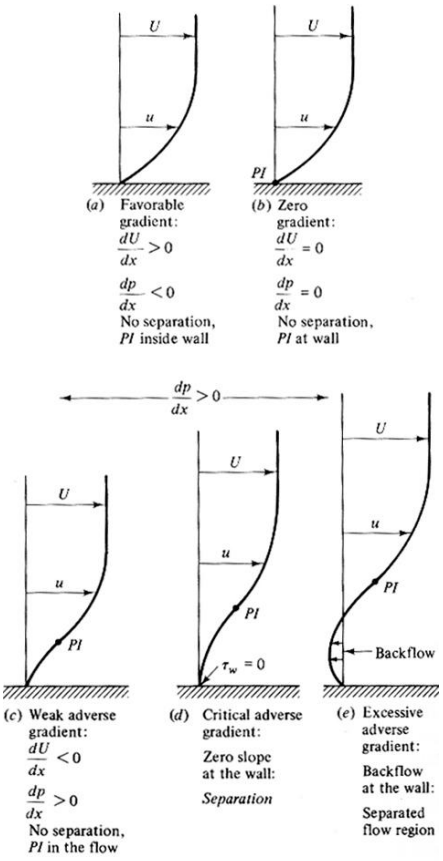

Figure 1-2: Velocity boundary layer evolution leading to flow separation on a cylinder. *From White.*

Wake characteristics

The characteristics of a stationary cylinder's wake are primarily functions of Reynolds number. At low Reynolds number ($Re < 5$), the flow is unseparated and fortuitously

resembles potential flow. As Reynolds number is increased ($5 < Re < 300$), a laminar vortex wake develops and eventually transitions to a turbulent wake. For the remainder of sub-critical flow ($300 < Re < 3 \times 10^5$), the wake remains fully turbulent, yet discrete discrete vortices are present. In this region, the wake is composed of a street of alternating vortices. This staggered arrangement is named the Karman street; after one of the first investigators of the phenomenon. Figure 1-3 shows the Karman street behind a circular cylinder. Here, the shedding frequency is defined as the rate at which a pair of vortices is shed from the cylinder. The vortex geometry of the Karman street causes oscillatory forcing of the cylinder; so that the cylinder is forced transversely to the flow at the shedding frequency, and is forced in-line with the flow at twice the shedding frequency. Further downstream of the cylinder, the vortices dissipate into unorganized turbulence. As the incident flow becomes turbulent ($Re > 3 \times 10^5$), the wake becomes disorganized but eventually discrete vortices reappear at higher values of Reynolds number.

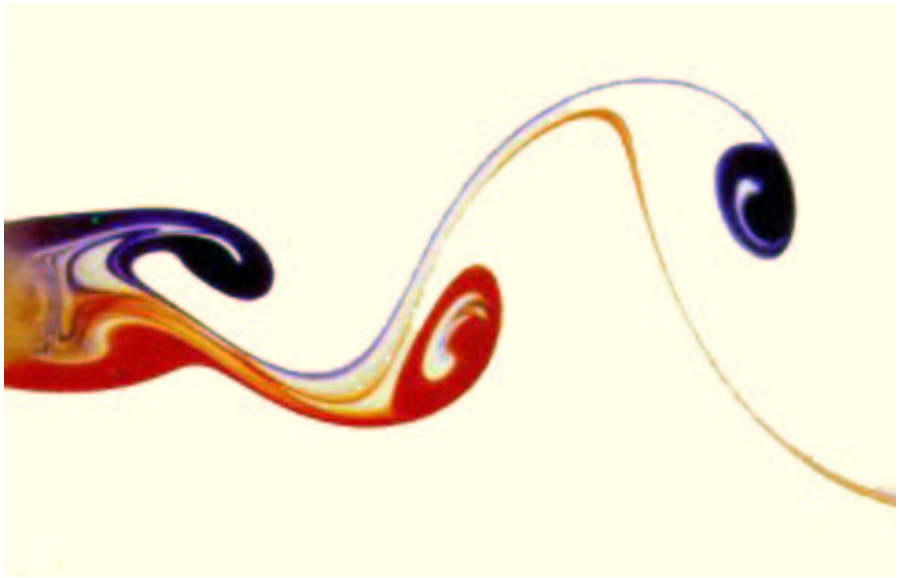

Figure 1-3: Karman vortex street downstream from a circular cylinder at low Reynolds number. *From Perry et al.*

Furthermore, Strouhal number, the parameter that relates vortex shedding frequency to the incident fluid velocity, is also a function of Reynolds number [3]. Figure 1-4 provides the experimentally determined relation between Strouhal number

and Reynolds number for a stationary, circular cylinder. As indicated by this figure, Strouhal number for sub-critical flows about a cylinder is consistently near 0.2. Thus, the Strouhal number used for all calculations herein is assumed to be 0.194. Previous experimental research at the MIT Testing Tank determined this value [7].

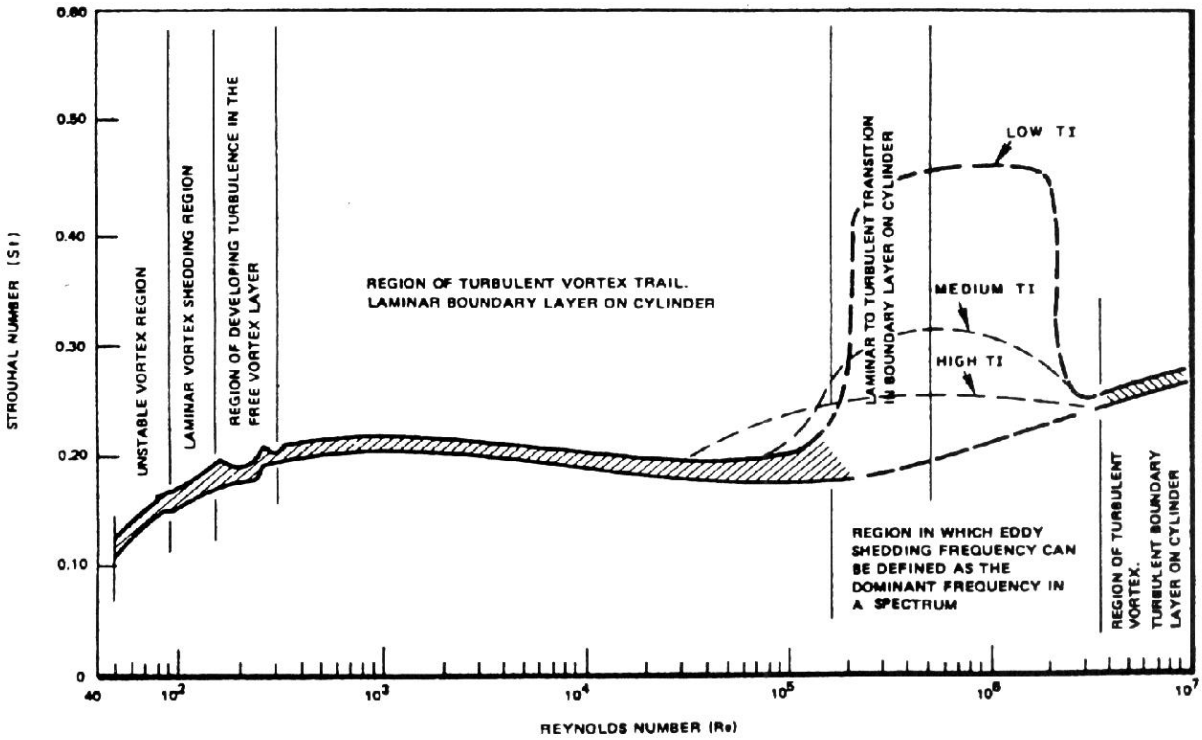

Figure 1-4: Strouhal number as a function of Reynolds number for various turbulence intensities. *From Chen.*

The near wake of a stationary cylinder subject to uniform cross-flow is characterized by distinct cells of vorticity. The correlation length is typically defined as the spanwise length of one vortex cell. The correlation coefficient, taken between two spanwise points downstream of a cylinder, provides a measure of the three-dimensionality of the flow. Correlation coefficient can be obtained from pressure, velocity, vorticity, or other measurements. A correlation coefficient of 1.0 indicates fully two-dimensional flow between the two points. Thus, reduction in correlation coefficient magnitude indicates an increase in three-dimensional flow, or flow in the spanwise direction. Correlation length is primarily a function of Reynolds number, surface roughness, and cylinder motion [21].

Cylinder motion and lock-in

In the case of a compliant structure, the forces resulting from vortex shedding can lead to oscillatory motion of the body. This vibration occurs primarily in the direction parallel to that of the incident flow. The amplitude of the vibratory response is governed primarily by the reduced velocity and the structure's mass and damping ratios [1]. Furthermore, such motions significantly influence the character of the wake.

As the oscillation amplitude of a cylinder increases, so does the strength of the shed vortices. The motion further organizes the vortex wake; enhancing correlation along the span. Significant growth in correlation length occurs as vibration amplitude ratio exceeds 0.1 [3]. Numerical studies predict that correlation length, $\frac{\Delta z}{D}$, for a cylinder with $Re = 1.9 \times 10^4$ increases from 3.5 to 40 over the amplitude ratio range 0.05 to 0.10 [18]. The intensified vortex wake imparts greater forces on the cylinder; increasing the mean and fluctuating drag.

Under most conditions, the vortex shedding frequency of a vibrating cylinder is predicted by the Strouhal number relation. However, over a range of reduced nominal velocity, this relation is violated as the shedding frequency synchronizes to the natural oscillation frequency of the cylinder. This phenomenon, known as *lock-in*, can shift the shedding frequency by up to $\pm 40\%$ from that predicted for a stationary cylinder. The reduced nominal velocity range over which lock-in occurs grows with increasing vibration amplitude. Lock-in initiates when the oscillation frequency nears the cylinder's natural frequency, i.e. $\frac{\omega_s}{\omega_n} \simeq 1.0$, and persists up to $\frac{\omega_s}{\omega_n} \simeq 1.4$ [1]; beyond which shedding frequency again follows the Strouhal relation. Assuming a Strouhal number of 0.2, Equations 1.10 and 1.12 predict that that lock-in will commence around $V_{rn} \approx 5$ and continue until V_{rn} exceeds 7. Within the lock-in region, resonant effects can further exaggerate vibration amplitude.

However, the phenomenon of vortex-induced vibration is self-limiting. Under most circumstances, amplitude ratio rarely exceeds unity because of changes in the pattern

[1] Here, ω_s is the shedding frequency predicted by the Strouhal relation for a stationary cylinder. During lock-in, this frequency is actually governed by the motion of the cylinder.

and phase of the wake that result from cylinder motion. At reduced nominal velocities below lock-in, each vortex is shed near the point of maximum displacement to create the Karman street. Yet, as lock-in initiates, the phase angle between the cylinder displacement and vortex shedding shifts by 180° as vortices begin to shed from the cylinder side opposite the maximum displacement. Additionally, the Karman vortex street can, at high values of amplitude ratio, transform into wake composed of staggered pairs of counter-rotating vortices. Through flow visualization techniques, Williamson and Roshko detail the dependence of these patterns on reduced velocity and amplitude ratio; terming the Karman street the "2S" pattern and the vortex pairs the "2P" pattern [25][24]. The forcing associated with a 2P shedding event is less than that of the organized 2S wake. Consequently, vibration amplitude is self-limiting because it becomes inversely proportional to the imparted forces. Figure 1-5 illustrates the two vortex patterns and their relation to phase angle between cylinder motion and transverse force.

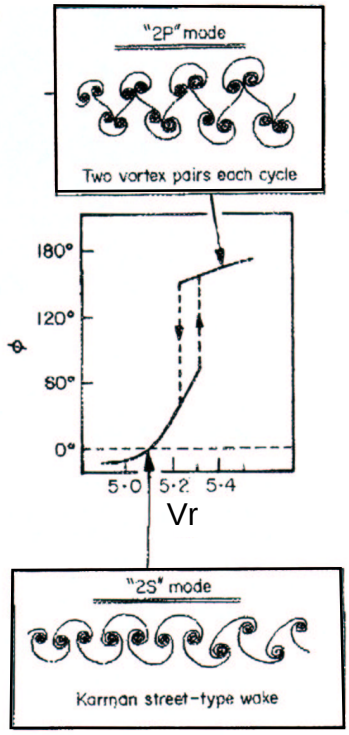

Figure 1-5: Vortex wake patterns and relation to phase angle, ϕ, between cylinder motion and lift force. *From Williamson and Roshko.*

Applications

Since inception, the offshore oil and other seafaring industries has been plagued by vortex-induced vibration fatiguing cylindrical structures placed in ocean currents. Engineers have developed a multitude of devices to prevent such vibrations, including: helical strakes, splitter plates, fairings, and turbulence tripping wires among others. Figure 1-6 provides examples of some of these methods. The purpose of all these devices is to restrict vortex correlation length, thus preventing the formation of powerful vortices. However, most of these tools are expensive and difficult to install, add drag to the structure, and are debilitated by biofouling. A primary motivation of the present research is the development of non-intrusive methods for suppressing vortex-induced vibration.

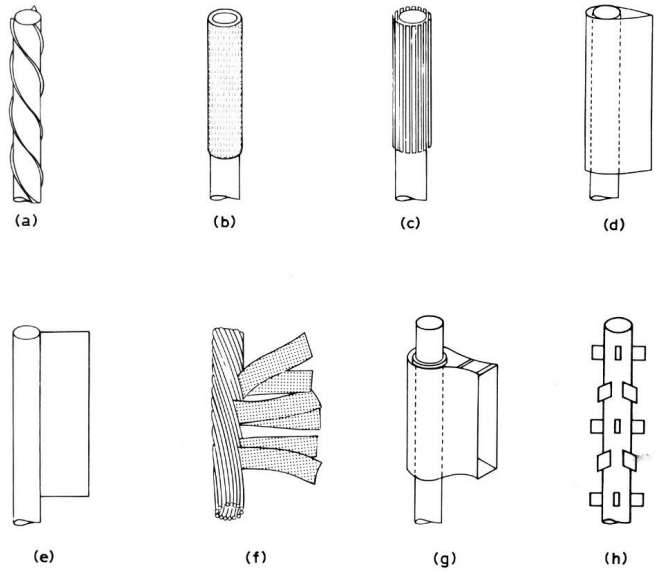

Figure 1-6: Vortex suppression mechanisms for cylindrical strucutres. a)helical strake, b)shroud, c)axial slats, d)streamlined fairing, e)splitter plate, f)ribboned cable, g)pivoted guiding vane, h)spoiler plates. *From Blevins.*

1.2 Previous Wake Correlation Research

The spanwise velocity correlation is a key parameter described in this thesis. Several research articles were influential to the design and analysis of the current correlation study. This section provides a brief synopsis of the most notable papers.

Grant In one of the first studies of its kind [5], Grant uses pairs of homemade anemometers to study the wake far downstream of a stationary cylinder in a wind tunnel. The tests are performed at $Re = 1300$, with wake sampling positions $\frac{x}{D} = 533$, $\frac{y}{D} = 0, 4, 7.6$. Seeking to determine the size of large-scale eddies, the author computes the velocity correlation coefficient between two points, as a function of separation, in the x,y, and z directions. Thus, the author presents nine correlations in the cylinder wake; three correlation directions as functions of three separation directions. Drawing from these results, the paper concludes that the far wake of a stationary cylinder is composed of three-dimensional pairs of counter-rotating vortices. Furthermore, these eddies are found to have axes of rotation inclined 45° to the central axis of the cylinder. Thus, Grant provides an early example of the use of velocity correlation in revealing the complex three-dimensionality of the wake.

Toebes Using an array of hot-wire anemometers and a Prandtl tube, Toebes produces signal traces of the unsteady flow immediately downstream of a vibrating cylinder [21]. These wind tunnel tests are performed in the high sub-critical Reynold number regime, $Re = 0.2 \times 10^5$ - 1.2×10^5. Toebes shows that vortex strength and frequency, although nearly harmonic, vary randomly. Most notably, Toebes provides the first surface plots of correlation coefficient magnitude as a function of amplitude ratio, $\frac{A}{D}$ and spanwise separation, $\frac{\Delta z}{D}$. Measured at $\frac{x}{D} = 0$, $\frac{y}{D} = 1$, correlation is seen to grow with amplitude ratio up to the maximum value of $\frac{A}{D} = 0.25$ and to decrease rapidly with $\frac{\Delta z}{D}$. The author uses these findings as evidence for his contention that the flow around a cylinder is a fluidelastic phenomenon; i.e. fluid motion contributes to structuring the vortex wake.

Ramberg and Grifffin While oscillating a flexible rubber cylinder in its third mode of vibration, Ramberg and Griffen use a pair of anemometers to measure the spanwise and streamwise correlation [17]. It is important to note that these tests are conducted in a wind tunnel, at a relatively low Reynolds number range, Re = 400-1300. The authors provide evidence that correlation is greatest during lock-in; when the shedding, vibration, and cylinder natural frequency are coincident. In the lock-in region, the maximum correlation coefficient, or "degree of correlation", is largely independent of vibration frequency and amplitude and Reynolds number. Furthermore, it is seen that the x and y probe coordinates have little effect on the spanwise correlation measurement. That is, the researchers find the trend of correlation coefficient versus $\frac{\Delta z}{D}$ to be independent of wake position.

Novak and Tanaka Using pressure sensors placed both radially and longitudinally on a cylinder in a wind tunnel, Novak and Tanaka compare the development of correlation length for both laminar and turbulent inflows [15]. The laminar flow has a maximum Reynolds number $Re = 1 \times 10^5$ and turbulence is uniformly generated by a coarse grid.

Plotting chordwise pressure correlation reveals that the pressure correlation measured between the two shoulders of a stationary cylinder is high; while correlation between the shoulders and the stagnation point approaches zero. However, as the cylinder is forced to vibrate, the shoulder-to-shoulder correlation decreases and shoulder-to-stagnation point correlation grows. This change is accompanied by a narrowing of the pressure spectrum bandwidth.

Overall, spanwise pressure correlation is greater for laminar incident flow than that for turbulent flow. The authors demonstrate a dramatic increase in correlation coefficient as amplitude ratio is increased from $\frac{A}{D} = 0$ to $\frac{A}{D} = 0.1$. To further describe this phenomenon with a numerical value of correlation length, the authors develop the following equation.

$$\frac{L}{D} = \int_0^\infty R(\frac{\Delta z}{D}) d\frac{\Delta z}{D} \tag{1.26}$$

where $\frac{L}{D}$ is nondimensional correlation length, R is correlation coefficient, and $\frac{\Delta z}{D}$ is spanwise separation. Using the coefficients c and n, the subsequent equation curve-fits the correlation coefficient data as a function of spanwise separation.

$$R(\frac{\Delta z}{D}) = e^{-(c\frac{\Delta z}{D})^n} \tag{1.27}$$

Combining Equation 1.26 and Equation 1.27 and solving for c and n allows computation of the experimentally obtained correlation length via the following equation.

$$\frac{L}{D} = \frac{1}{nc}\Gamma(\frac{1}{n}) \tag{1.28}$$

where Γ is the gamma function defined as

$$\Gamma(\frac{1}{n}) = \int_0^\infty e^{-t}t^{(\frac{1}{n}-1)}dt \tag{1.29}$$

Using this formulation, the authors state that the correlation length of a cylinder in laminar flow increases from $\frac{L}{D} = 3.5$, when the cylinder is stationary, to $\frac{L}{D} = 43.4$, when the cylinder is forced to oscillate at $\frac{A}{D} = 0.1$. In turbulent flow, the correlation length increased from $\frac{L}{D} = 2.4$ to $\frac{L}{D} = 10.4$. It is important to note that these measurements are taken on the cylinder's surface.

Sumer *et al.* In two papers, Sumer *et al.* investigate the spanwise pressure correlation on the surface a cylinder subject to oscillatory flows while stationary, experiencing forced vibrations, or experiencing self-induced vibrations. The oscillatory flow is simulated by driving a testing carriage back and forth in a still water flume. Furthermore, these studies investigate the affect of a nearby wall on the wake correlation. Tests are performed over a range of Reynolds number (defined by the maximum fluid velocity), $Re = 3.4 \times 10^4 - 6.8 \times 10^4$. The flow is oscillated to achieve the Keulegan-Carpenter numbers $KC = 6$, 20, and 65.

For a stationary cylinder in oscillatory flow, time domain records of pressure correlation illustrate that the correlation achieves a maximum value at the instant the flow around the cylinder becomes stationary before reversing direction.

In the case of forced vibrations [9], a hydraulic system oscillates the cylinder over the range of amplitude ratio $\frac{A}{D} = 0 - 0.35$. Results indicate that correlation increases with vibration amplitude up to $\frac{A}{D} = 0.1$ for $KC = 6$ and $\frac{A}{D} = 0.15$ for $KC = 20$ and 65. As amplitude ratio increases further, the correlation coefficient decreases. Correlation coefficient is greatest, at all values of separation $\frac{\Delta z}{D}$, for $KC = 6$.

However, a different correlation trend is seen for a spring-mounted cylinder that is free to vibrate [19]. As with the cylinder experiencing forced vibration, correlation along the span of the freely vibrating cylinder increases with vibration amplitude. Though, instead of decreasing at greater amplitudes, the wake correlation of the freely vibrating cylinder remains consistently high. The maximum values of correlation coefficient are seen within the lock-in region, where motion amplitude is greatest.

Szepessy Through the use of pressure sensors located midspan on a flexible tube in a wind tunnel, Szepessy is able to produce time traces of spanwise correlation and phase difference [20]. Analysis of the instantaneous pressure signals reveals disturbances or "shedding irregularities". It is these irregularities, the author contends, that lead to a phase drift in the vortex shedding along the span. That is, rms phase difference between two interrogation locations is seen to increase rapidly with increasing separation distance. Subsequently, this phase lag causes the reduction in correlation coefficient at greater spanwise separations. Lock-in is believed to retard the phase drift growth and reduce the rate of correlation decay with separation. The maximum correlation length is estimated to be $\frac{L}{D} = 2.7$. Also, the article reports a periodic oscillation in spanwise correlation with a period around 10-20 times the Strouhal vortex shedding period.

Wu *et al.* Using hydrogen bubble flow visualization, pressure sensors, and hotwire anemometers, Wu *et al.* analyze the three dimensional structures of the wake between and downstream of two stationary cylinders in tandem [26]. Flow visualization is performed in a water channel ($Re = 1000$) and correlation studies are performed in a wind tunnel ($Re = 4.2 \times 10^4$ and $Re = 1.7 \times 10^4$). The authors conclude that

the separation distance of two cylinders has a profound effect on the spanwise wake correlation. For small cylinder separations, $\frac{\Delta S}{D} \leq 3.0$ [2], the correlation coefficient, measured both between and downstream of the cylinders, remains relatively high over the range of spanwise separation, $\frac{\Delta z}{D} = 0 - 4.5$. This enhanced correlation results from the suppression of the leading cylinder's vortex wake and the shedding of a single wake from both cylinders. However, as the distance between the cylinders is further increased, the wake of the leading cylinder becomes stable and buffets the trailing cylinder with a turbulent vortices. Consequently, spanwise correlation magnitude diminishes rapidly with greater separations.

The authors attribute the deterioration of spanwise correlation to the presence of three-dimensional structures in the wake. Using flow visualization, the authors are able to discern spanwise and streamwise vortical structures in addition to the principle vortices shed at the Strouhal frequency. The presence of these three-dimensional structures, in a supposed two-dimensional flow, stimulates turbulence witch in turn erodes correlation.

Hayakawa and Hussain Hayakawa and Hussain use various arrays of cross-wire anemometers, orientated to measure velocity in the x and y directions simultaneously, to map the spanwise vorticity field in the wake of a stationary cylinder [6]. Experiments are performed in a wind tunnel at $Re = 1.3 \times 10^4$. This technique also allows for the computation of spanwise vorticity correlation. The authors develop a "somewhat arbitrary" definition of correlation length, or the scale of the spanwise structures. Specifically, the correlation length is the separation over which the spanwise vorticity correlation coefficient drops by e^{-1}. Estimated values of correlation length in the current study are based on this definition. Using this formula, the article presents the resulting correlation lengths far downstream from the cylinder: $\frac{\Delta z}{D} = 1.8$ at $\frac{x}{D} = 20$ and $\frac{\Delta z}{D} = 0.9$ at $\frac{x}{D} = 40$. Thus, correlation is seen to diminish further downstream as the vortices dissipate into turbulence.

[2] equivalent to $\frac{\Delta x}{D}$

Chapter 2

Experimental Methods

2.1 Thermal Anemometry

All experiments described in this thesis involve the use of thermal anemometry sensors to characterize the velocity downstream of an oscillating cylinder. This section provides a summary of the theory behind such techniques and how they are employed in the current experiments.

2.1.1 Theory

Constant temperature anemometry is a tool used for investigating the characteristics of and structures within fluid flow. The working principle is based on the cooling effect of a flow on a heated body. A typical anemometry probe includes a thin wire or film element connected to one arm of a Wheatstone bridge. The electrical current heats the wire in a process termed Joule heating. In a fluid, this heat is constantly being lost to the environment through convection. The rate of heat transfer from the wire to the fluid of measurement is a function of fluid velocity, temperature, density, and viscosity. A servo amplifier maintains constant resistance, and thus temperature, of the wire. Thus, as the wire is cooled by fluid flow, greater current is required to maintain the temperature of the wire. Ultimately, the amplifier outputs a voltage that is related to the flow velocity through a higher-order polynomial. The simplified

governing equation is

$$\frac{dE}{dt} = W - H \tag{2.1}$$

where E is the thermal energy stored in the wire, H is the heat transferred from the wire to the fluid, and W is the power generated by Joule heating

$$W = I^2 R_W \tag{2.2}$$

where I is the electrical current passed through the wire and R_W is the resistance of the wire, a function of wire temperature. For equilibrium conditions, the heat storage in the wire is zero and heat flux is equal to Joule heating.

$$\frac{dE}{dt} = 0 \qquad W = H \tag{2.3}$$

Constant temperature anemometry probes are capable of resolving small-scale fluid velocities with very fast response to fluctuations in the flow. However, the fragile sensors are susceptible to chemical contamination and mechanical failure. At relatively low velocities, including those of the current study, such problem sources become important. Bubbles of dissolved gas, particulate matter, and oxidation can change the heat transfer properties of the sensor element. Also, heat radiation from the wire to the supports and temperature changes in the fluid of measurement become significant when the fluid velocity is small. Because of these effects, frequent calibration of the probe in a known fluid velocity is necessary [13].

2.1.2 Experimental Application

The six anemometer probes used in the experiment are TSI hot film cylindrical, single sensor, end flow probes (model number 1210-20W). Each probe features a thin film of platinum deposited on a cylindrical quartz substrate as the sensitive element. An insulated support post holds each end of the filament. Flow is intended to approach the film orthogonally, parallel to the probe body. Figure 2-1 provides an image of the sensor provided by the manufacturer.

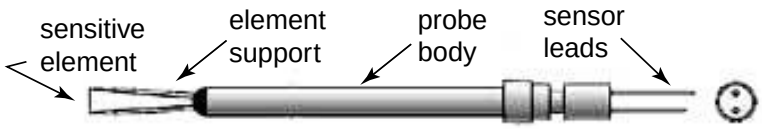

Figure 2-1: TSI Model 1210-20W thermal anemometry probe.

A stainless steel support connected to a BNC cable (TSI model number 1159-15) holds each probe in place and transmits the current between the sensor and the amplifier. Brackets on the Anemometer Positioning System hold these supports to accurately and precisely locate each probe. Each of the six anemometer amplifiers (TSI model number CTA1750-Plus) forms a Wheatstone bridge using a probe element, a control resistor matched to the probe at the factory, and a variable gain resistor. The variable gain is set such that each amplifier outputs a voltage between 0V and 10V over the range of applicable velocities. An electrically grounded steel case (shown in Figure 2-2) houses the six amplifiers.

To ensure accurate operation of the sensors, calibration is performed daily, or about every 100 runs, on all anemometers. The computer-controlled velocity of the carriage provides a baseline to reference the anemometer voltages. The experimental cylinder and struts are rotated out of the water to provide an unobstructed horizontal flow to the probes. Because the towing velocity for all experiments is $40\frac{cm}{s}$, the following calibration speeds, V_T, are used to characterize the sensor's response in the wake of a bluff body; V_T = 15, 19, 23, 27, 31, 35, 39, 43, 47, $51\frac{cm}{s}$. A fourth-order polynomial curve fit to the resulting voltage allows for the determination of any instantaneous fluid velocity. Figure 2-3 provides an example of the daily calibration results of all six anemometers.

Figure 2-2: Photograph of the six anemometer amplifiers and housing.

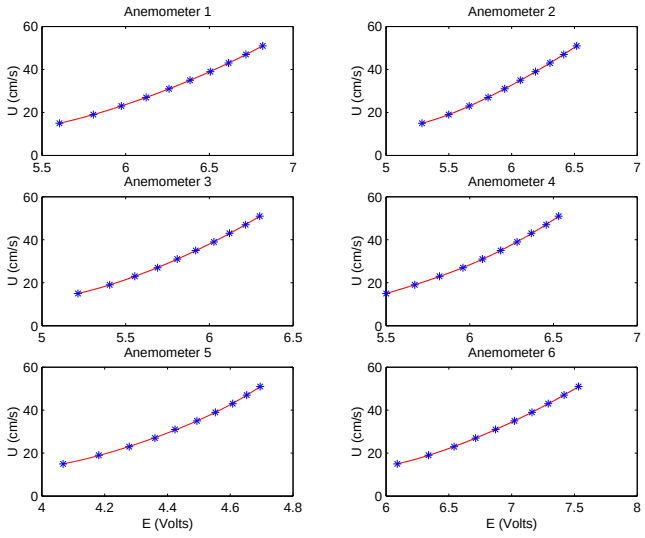

Figure 2-3: Example of anemometry calibration data points and fourth-order curve fit (solid line).

2.2 Experimental Setup

2.2.1 Virtual Cable Testing Apparatus

All experiments described in this thesis are performed in the Ship Model Testing Tank at the Massachusetts Institute of Technology. The laboratory is centered around a 30m $\times$ 2.5m $\times$ 1.2m towing basin. A torque-controlled drive system enables a utility carriage to traverse the length of the basin at speeds between $0.12\frac{m}{s}$ and $1.50\frac{m}{s}$. An independent computer controls the traverse velocity of the carriage. The Virtual Cable Testing Apparatus (VCTA) rides upon this utility carriage. Figure 2-4 illustrates the arrangement of VCTA and the Anemometer Positioning System.

Experimental cylinders are mounted between two foil-shaped struts that extend above the surface of the water. These struts, as well as nearly all the experimental hardware, are formed from alloy 6061 or 6063 aluminum. Thin, circular end plates ($45cm$ diameter, $0.3cm$ thickness) bound both ends of the test cylinder with a gap less than $0.3cm$. The end plates promote two-dimensional flow over the cylinder and prevent end effects. A brushless servo motor (Parker model number ML3450A-10) connected to a linear slide (ALM model number SPA-10912-01) actuates the struts and test cylinder. That is, the cylinder is capable of motion only in the direction perpendicular to that of the incident flow. A Motion Engineering Inc. PID motion control card in a computer on board the carriage controls the servo motor and thus the motion of the cylinder. Also, the motion control card monitors an optical encoder on the motor shaft and provides a voltage corresponding to the position of the cylinder.

Although the apparatus is capable of actuating two cylinders independently, the experiments described in this thesis employ only one cylinder. The test cylinder is a hollow aluminum tube $2m$ in length with a $7.62cm$ outer diameter. Thus, the cylinder's aspect ratio is slightly greater than 26. Each end is sealed with a delrin plug and RTV silicone. The cylinder is polished daily, or about every 100 runs, to ensure a smooth, uniform surface.

To measure the flow-induced forces on each side of the cylinder, a Kistler piezo-electric force transducer (model number 9601A3111000) is mounted on a stainless

steel post that connects the cylinder's end plug to the foil strut. The sensor is capable of recording the force imparted to the cylinder in both the lift and drag directions. A digital amplifier (Kistler model number 5010B) transforms the piezoelectric charge into a corresponding voltage. Daily calibrations ensure the accuracy and precision of the device. Specifically, a known weight is applied to each end of the cylinder, *in situ*, and the resulting voltage is recorded. A custom 90° jig allows for calibration of the drag force.

The summation of these devices forms the Virtual Cable Testing Apparatus. The apparatus permits three types of experiments with the following configurations: a stationary cylinder, a cylinder under forced motion, and a freely-vibrating cylinder. The former two configurations are achieved by programming the appropriate motion parameters into the motion control card. However, free vibrations are achieved through a sophisticated force feedback control system described in the following section.

All experiments described in this thesis are conducted at a towing speed of $40\frac{cm}{s}$. Thus, the resulting Reynolds number is in the high sub-critical region, $Re = 30,480$.

Free vibration through force feedback

Free vibration of the rigid aluminum cylinder is achieved through a hybrid experiment-simulation using force feedback. The first step in implementing this system is the development of a mass-spring-dashpot simulation model in the form

$$F(t) = m\ddot{y}(t) + b\dot{y}(t)b + ky(t) \tag{2.4}$$

where $F(t)$ is the instantaneous force imparted on the cylinder, $y(t)$ is the instantaneous vertical displacement of the cylinder, and m, b, and k are the mass, damping, and stiffness of the virtual cylinder, respectively. These virtual parameters can be specified by the user; allowing for variation of reduced nominal velocity.

A computer on board the carriage performs the simulation; reading force and displacement information from a data acquisition card, calculating the modelled velocity, and issuing that velocity to the servomotor through the motion control card.

The rate of the control loop is limited by the computation time step at 250Hz. $F(t)$ is input to the simulation via the force transducers and includes both the fluid and inertial forces. The simulation removes the physical inertial force so that only the hydrodynamic force enters into the model. Furthermore, the physical cylinder mass is replaced with the virtual cylinder mass. For all free vibration experiments herein, the virtual mass ratio is $m^* = 3.0$. Although the virtual damping is set to zero for these experiments, the feedback loop is not ideal and the physical damping ratio is non-zero. Multiple experiments performed at $V_{rn} = 6.0$ reveal that the actual damping ratio is near $\zeta = 0.032$.

Please refer to [8] for a detailed description of the design of this system.

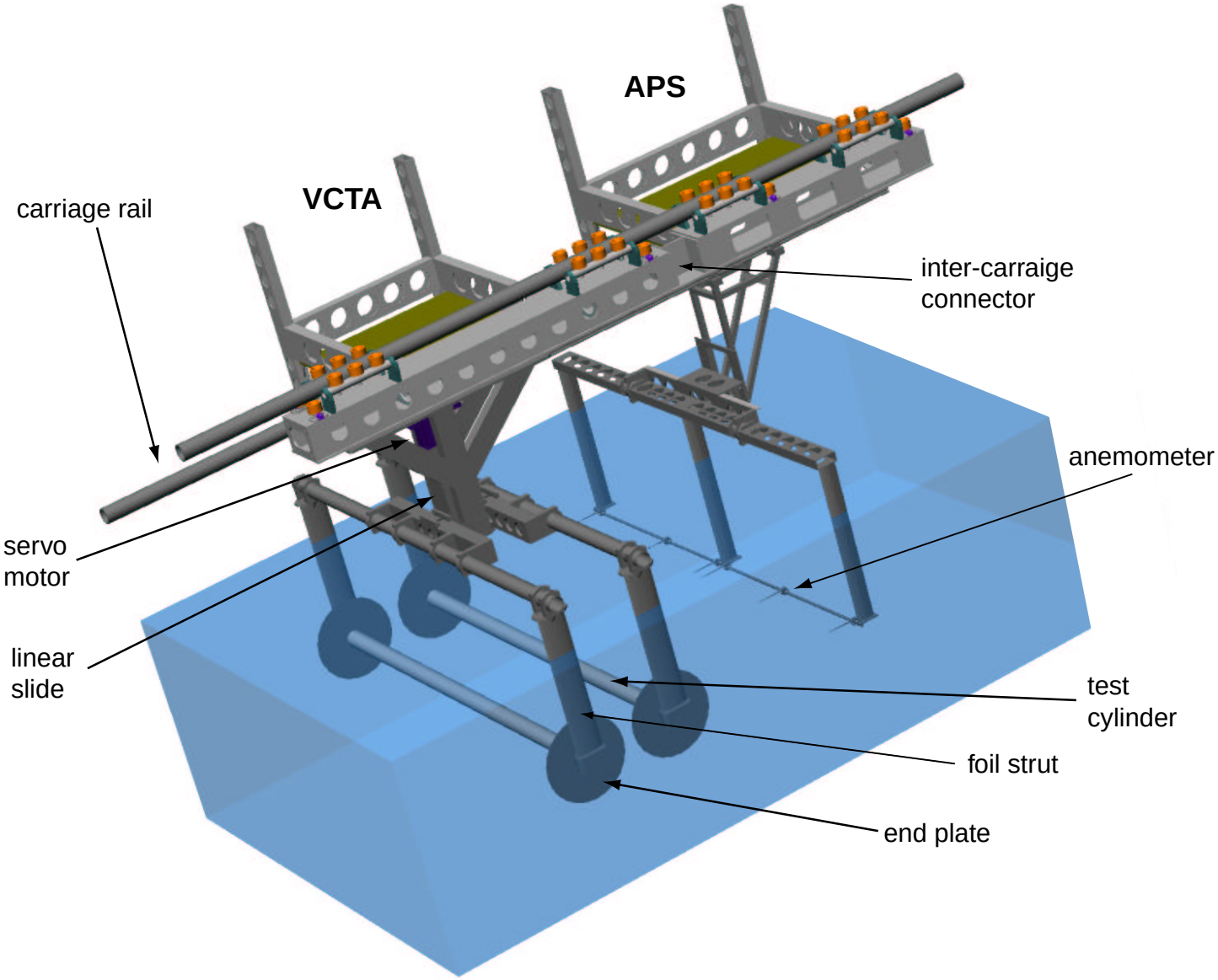

Figure 2-4: A computer-rendered image of the Virtual Cable Testing Apparatus and Anemometer Positioning System.

2.2.2 Anemometer Positioning System

The Anemometer Positioning System (APS) is an apparatus that allows for precise positioning of thermal anemometers in the downstream region of an experimental cylinder. A second carriage is mounted, by way of a coupling, to the rear of the VCTA carriage to house the APS. Rails allow the apparatus to traverse anywhere within the downstream region from $\frac{x}{D} = 0$ to $\frac{x}{D} = 15$ [1]. Slides equipped with handbrakes hold a truss and bracket in place to provide a stable sensor platform.

The apparatus's two configurations allow for a rake of anemometers to be oriented either parallel to or perpendicular to the cylinder axis. In the horizontal configuration (shown in Figures 2-4 and 2-6), three foil struts hold a cylindrical stainless steel rod parallel to the cylinder. This horizontal arrangement is used for spanwise correlation studies. Through coarse adjustment of the elevation of the horizontal rake and fine adjustment of the cylinder position, the APS permits correlation studies over a range of vertical positions from $\frac{y}{D} = 0$ to $\frac{y}{D} = 4$. However, the current experiments utilize only three such positions, $\frac{y}{D} = 0.5$, 2.0, and 3.0, at one downstream location, $\frac{x}{D} = 2.0$.

Precision-drilled holes in the rod allow brackets to hold anemometers at known positions along the span of the cylinder. Specifically, anemometers can be placed at 55 locations along the span of the cylinder with a maximum separation of $\frac{\Delta z}{D} = 27.5$ and a resolution of $\frac{\Delta z}{D} = 0.5$. Two anemometer arrangements enable a limited number of probes, six in this case, to characterize the correlation over the entire span of the cylinder. The *alpha* arrangement has closely spaced probes to determine correlation at small separations. Conversely, the *beta* arrangement has widely spaced probes to determine correlation over large separations. All relevant experiments employ both arrangements. Table 2.1 details the separations used in each arrangement. The combination of these two arrangements results in 24 unique separations between $\frac{\Delta z}{D} = 0.5$ and $\frac{\Delta z}{D} = 24.5$.

A similar cylindrical rod is mounted in parallel to a single foil strut to form the vertical configuration of the APS (shown in Figure 2-7). This configuration is used for

[1] These values and others presented in this section are referenced to the $7.62cm$ test cylinder used for all experiments .

	Arrangement *alpha*	Arrangement *beta*
distance from midpoint $\frac{z}{D}$	-4.0, -1.0, 0.0, 0.5, 2.5, 5.0,	-12.5, -7.0, -5.5 0.0, 10.0, 12.0
separations $\frac{\Delta z}{D}$	0.5, 1.0, *1.5*, *2.0*, **2.5**, 3.0, 3.5, 4.0, **4.5**, 5.0, 6.0, 6.5, 9.0	*1.5*, *2.0*, **5.5**, 7.0, 10.0, 12.0, 12.5, 15.5, 17.0, 17.5, 19.0, 22.5, 24.5

Table 2.1: Location of the six anemometer probes and resulting separations. Separations in **bold** are repeated within that arrangement and separations in *italic* are repeated between the two arrangements.

mapping the mean velocity profile downstream of the cylinder. Coarse adjustment of the placement of the probe brackets and fine adjustment of the test cylinder position allow the vertical location of the anemometers to vary from $\frac{y}{D} = 0$ to $\frac{y}{D} > 7$ with unlimited resolution. For all experiments herein, the rake is located directly downstream of the cylinder's midpoint, i.e. $\frac{z}{D} = 0$. Also, the two downstream locations investigated in these experiments are $\frac{x}{D} = 2.0$ and $\frac{x}{D} = 5.0$. In these experiments, two arrangements of the six anemometer probes discretize the downstream velocity profile between $\frac{y}{D} = 0$ and $\frac{y}{D} = 5.5$ with a resolution of $\frac{y}{D} = 0.5$. Figure 2-5 illustrates the anemometer locations for both rake configurations.

Because the wake is assumed to be symmetric about the cylinder axis, measurements are taken only in the upper hemisphere of the wake. Furthermore, the probe element, or "hot film", orientation is different for the two APS configurations. During spanwise wake correlation studies, employing the horizontal arrangement, the anemometer sensor elements are configured so that they are parallel to the central axis of the test cylinder. Thus, the probes detect primarily the horizontal and vertical components, i.e. u and v, of the wake velocity. In this configuration, the voltage output of the anemometers is proportional to the vector sum of these two velocity components. This approach is intended to capture the velocities generated by the principle vortices shedding from the cylinder. However, in the case of the vertical

APS configuration, the probe elements are oriented perpendicular to the central axis of the test cylinder. So, during profile mapping experiments, the probes are exposed chiefly to the horizontal and spanwise components, i.e. u and z, of the wake velocity. This approach is intended to capture the mean in-line velocity. Figure 2-5 also illustrates the probe orientation for each configuration.

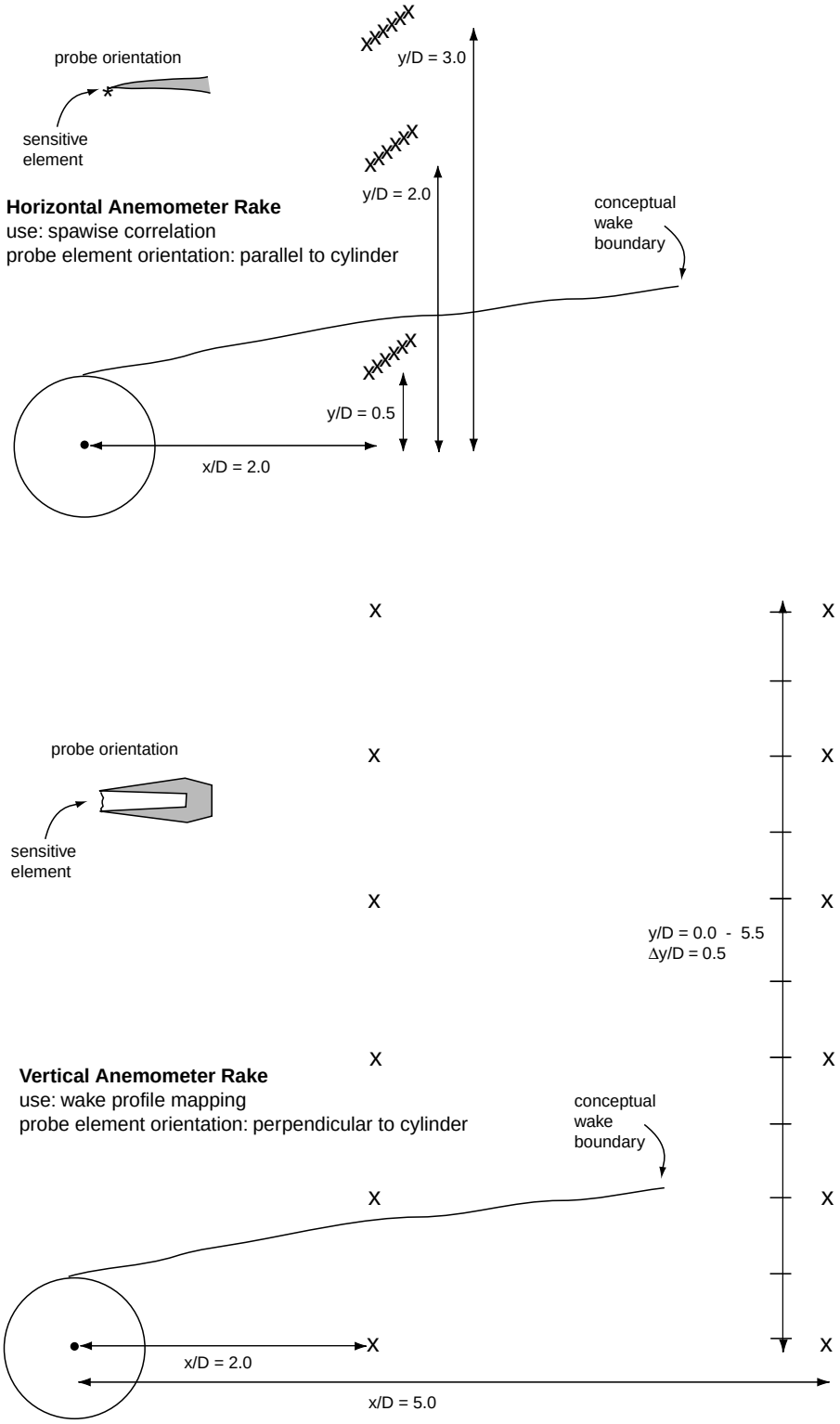

Figure 2-5: Location and orientation of anemometer rakes for horizontal and vertical configurations. **X** represents, roughly, anemometer position.

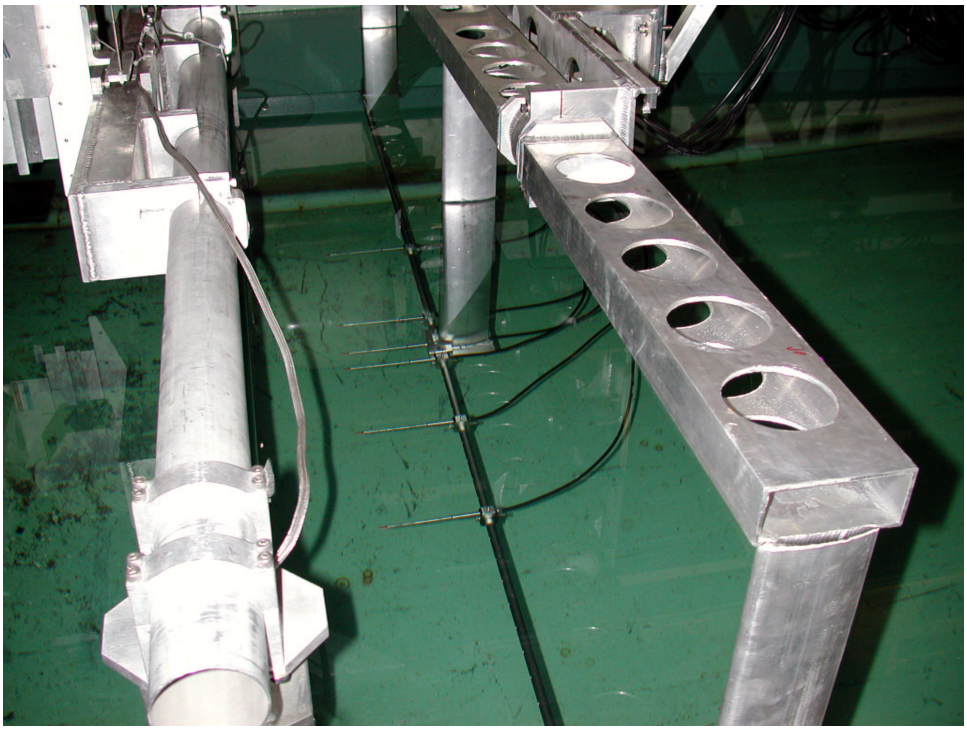

Figure 2-6: Photograph of the Anemometer Positioning System in the horizontal configuration used for spanwise correlation studies.

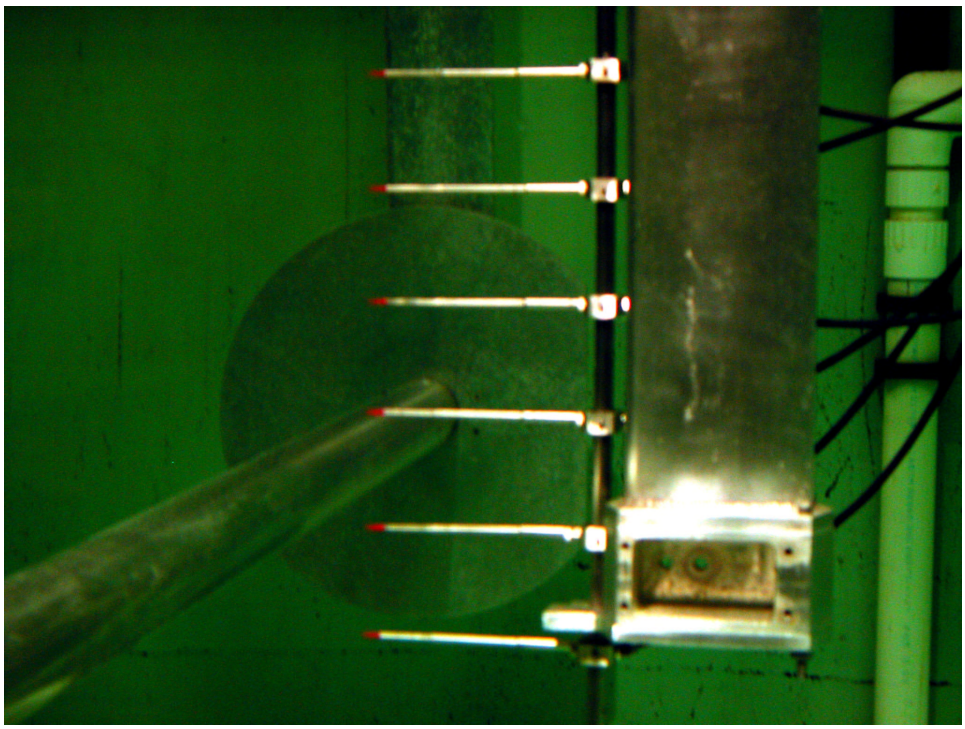

Figure 2-7: Photograph of the Anemometer Positioning System in the vertical configuration used for mapping of the wake velocity profile.

2.2.3 Data Acquisition and Processing

After completion of anemometer and force transducer calibrations, the appropriate calibration coefficients are input to the VCTA control software. The apparatus is then ready to execute forced or free vibration experimental runs. During a typical run at a tow velocity of $40\frac{cm}{s}$, the carriage traverses the entire basin in about 40 seconds. Immediately after each experiment, the carriage is returned to its start position and the parameters for the next run are input to the control software. Several minutes elapse between each run to allow the ambient turbulence and vorticity in the basin to settle.

A Computer Boards Inc. data acquisition card (model number CIO-DAS6402/16) in a separate computer records the voltages of all sensors, including: servo motor encoder, force transducers, and anemometers. The board samples a total of 11 data channels at a rate of 100Hz. DasyLab software stores the data from each experimental run to disk in the IEEE 32-bit file format. Figure 2-8 provides a example of the data obtained from one experimental run. The data processing software utilizes only the steady part of the run, after any transients have died out and before motion stops.

Matlab technical computing software parses the data file and performs all analysis. Windowing allows the determination of each parameter for a subset of data, approximately one oscillation. Thus, the values presented herein are averages over 20-40 oscillation cycles. The processing algorithm computes the following parameters for each experimental run.

- Amplitude ratio, $\frac{A}{D}$, is computed from the average of the 0.5% highest motion amplitudes.

- Peak frequency, such as that of the lift force, the cylinder oscillation, and the wake, is obtained from a fast-Fourier transform and resulting power spectral density.

- The two in-line force signals are summed and averaged to determine the mean drag coefficient, $C_D(mean)$.

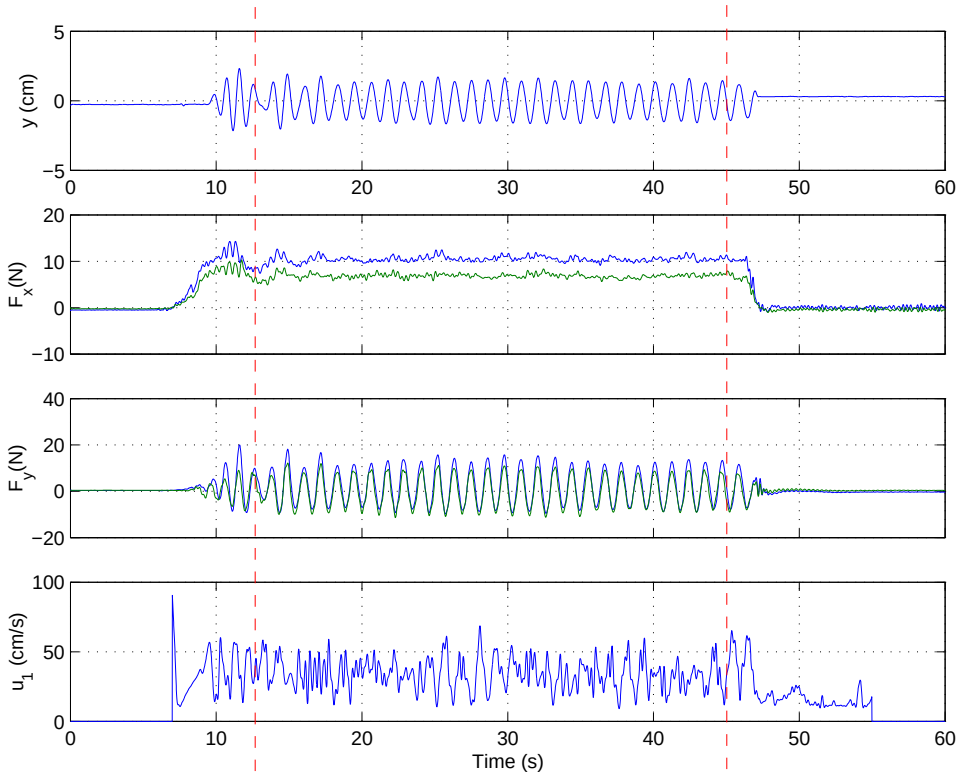

Figure 2-8: Example data from free vibration experimental run at $V_{rn} = 3.9$. Data channels from top to bottom: cylinder displacement, drag forces, lift forces, and single anemometer. Dashed lines bound region of investigation.

- Fluctuating drag coefficient, $C_D(std)$, is computed from the standard deviation of the in-line force.

- Lift coefficient in phase with velocity, C_{LV}, lift coefficient in phase with acceleration, C_{LA}, and phase angle between lift force and displacement, ϕ are computed via an inner product calculation as described in [22].

- The lift force correlation coefficient, F_C, is calculated with respect to the forces on either end of the cylinder.

- For wake mapping experiments, the mean velocity, $\bar{u}$, recorded by each anemometer is computed.

- For spanwise correlation experiments, the correlation coefficient, R_{ij} is taken between each of the six anemometers.

- To determine the mean phase difference, ψ_{ij}, between anemometers, a Hilbert transform calculates the discrete-time analytic signal for each sensor. The angle of this imaginary transform is equivalent to the instantaneous phase of the original signal. This approach requires preliminary tight bandpass filtering of the signals to obtain a monotonic input.

It is important to note that all signals are low-pass filtered at 30 $\frac{rad}{s}$ to eliminate noise. Specifically, the filter acts both forward and backward to eliminate any filter-induced phase lag. This filter acts prior to the application of force calibration coefficients and the polynomial anemometer calibration.

Chapter 3

Free Vibration Results

Free vibration experiments are performed over the range of reduced nominal velocity $V_{rn} = 3.0 - 12.0$ with a resolution of $V_{rn} = 0.1$. The current study sweeps through the parameter space a total of six times to accommodate the three anemometer positions and the two anemometer configurations. This chapter describes the coupled vibration response of both the cylinder and the fluid.

3.1 Vibration Dynamics

Amplitude

Figure 3-1 illustrates the dependence of amplitude ratio on reduced nominal velocity for all experiments. Initially, vibration amplitude increases rapidly with reduced nominal velocity. Amplitude ratio reaches a maximum, narrowly exceeding unity, at $V_{rn} \approx 5.7$. Yet, at greater values of V_{rn}, the vibration amplitude ratio decreases steadily with increasing velocity. A distinct plateau is evident as amplitude ratio remains nearly constant near $\frac{A}{D} \approx 0.55$ for $V_{rn} \approx 7.0 - 8.5$. The cylinder oscillation continues to diminish at higher velocities; approaching zero for the largest values of V_{rn} investigated.

Similarly, Figure 3-2 shows the trend of vibration amplitude as a function of reduced velocity. That is, this figure includes additional information on the observed

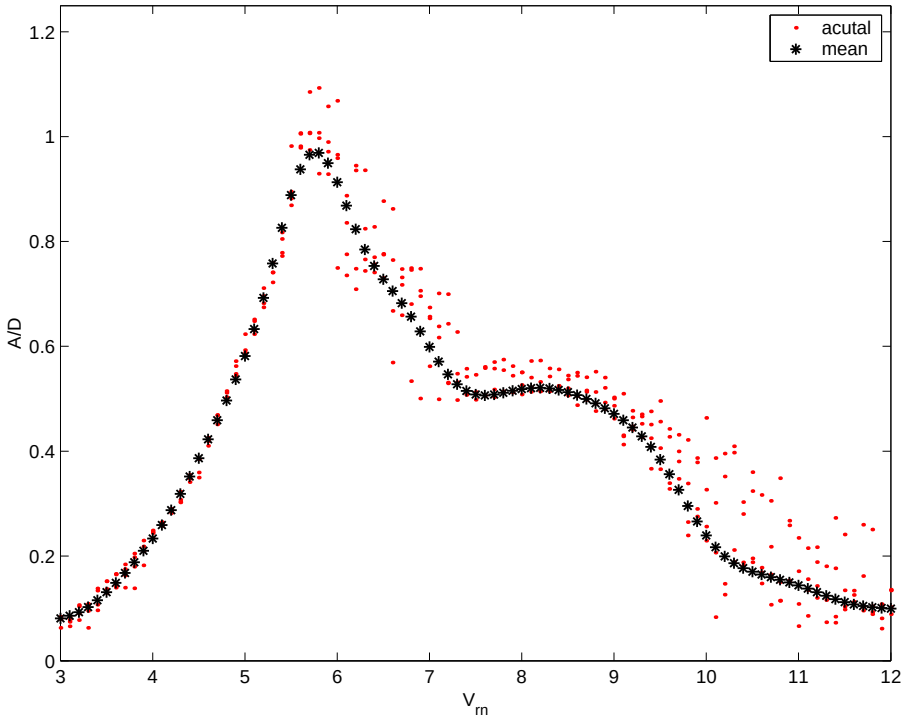

Figure 3-1: Amplitude ratio as a function of reduced nominal velocity.

vibration frequency. The "mean" plot in this figure is generated from the amplitude and frequency observed at each reduced nominal velocity, averaged over six iterations. Amplitude ratio increases abruptly with reduced velocity from $V_r = 5.5$ up to $V_r = 6.3$. A clear peak in amplitude ratio is centered around $V_r \approx 6.3$. Thus, the maximum vibration amplitudes observed occur within a small frequency band. Several data points, at different values of $\frac{A}{D}$, fall along a line of reduced velocity $V_r = 6.7$. In contrast, no vibration is observed at the corresponding frequencies of the nearby reduced velocities. These results suggest that frequency synchronization of the vortex shedding and the cylinder oscillation occurs at $V_r = 6.7$. Based on this assumption, the corresponding Strouhal number is near $S = 0.15$. Furthermore, the highest values of amplitude ratio occur just outside of this fundamental lock-in reduced velocity. This behavior indicates that the resonant effects accompanying lock-in extend over a considerable frequency band. Amplitude ratio remains nearly constant at $\frac{A}{D} \approx 0.5$ between reduced velocity $V_r = 7$ and $V_r = 8$. As reduced velocity increases further, the vibration amplitude tends to decrease; mean $\frac{A}{D}$ is near 0.1 at $V_r > 9$. However,

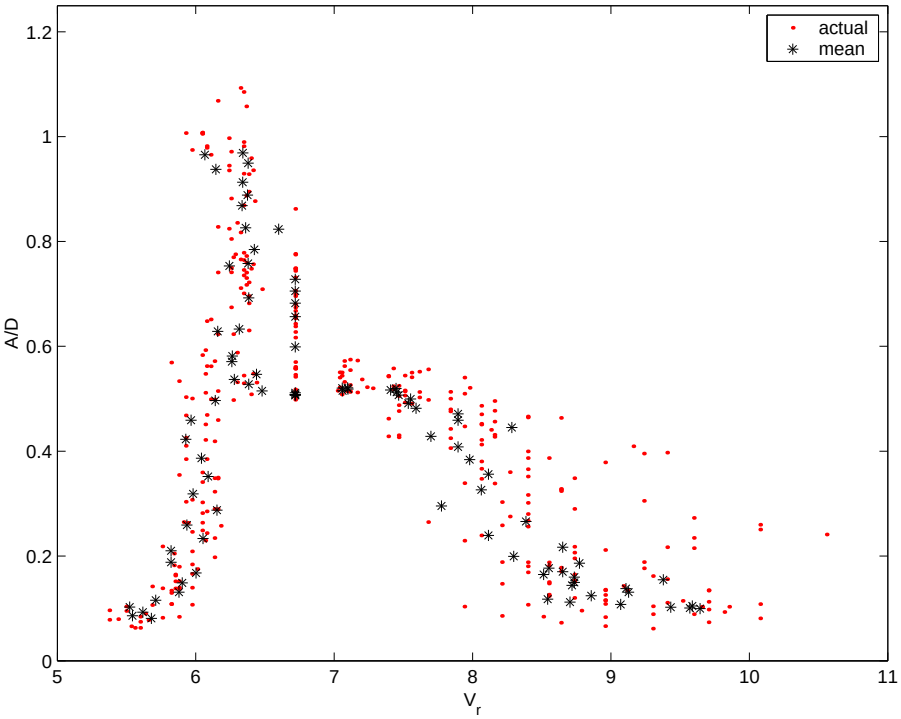

Figure 3-2: Amplitude ratio as a function of reduced velocity.

significant scatter is evident in this region and amplitude ratios vary greatly for a given reduced velocity.

Frequency

Figure 3-3 provides the frequency ratio plots of cylinder oscillation, lift force, and downstream velocity. The points for these three frequencies are coincident for a large range of reduced nominal velocity, $V_{rn} = 3 - 9$. Frequency ratio increases monotonically from $\frac{\omega_*}{\omega_n} \approx 0.5$ to unity over $V_{rn} = 3$ to $V_{rn} \approx 6.2$. A discontinuity is evident around $V_{rn} \approx 6.3$; where frequency ratio jumps from $\frac{\omega_*}{\omega_n} = 1.1$ down to $\frac{\omega_*}{\omega_n} = 0.9$. This behavior is likely indicative of the synchronization of vortex shedding frequency and oscillation frequency. Because the frequency ratio remains near unity throughout, the region within $6 < V_{rn} < 7$ is roughly defined as the lock-in region. Beyond this region (i.e. $7 < V_{rn} < 8$), the frequency ratio continues to increase steadily before plateauing around $\frac{\omega_*}{\omega_n} = 1.2$. The coincidence of the three frequencies ends abruptly around $V_{rn} \approx 9$; as the lift force and downstream velocity frequencies

jump up to nearly twice that of the cylinder motion. This transition provides evidence of the wake transformation from the 2S to 2P vortex wake. That is, the doubling of the number of vortices per cycle is evident in the lift force and downstream velocity spectra but not in that of the cylinder motion. As reduced nominal velocity increases from $V_{rn} = 9$ to $V_{rn} = 12$ the wake frequency ratio rises steadily from $\frac{\omega_w}{\omega_n} \approx 1.8$ to $\frac{\omega_w}{\omega_n} \approx 2.4$ while the oscillation frequency ratio continues to fluctuate around $\frac{\omega_o}{\omega_n} \approx 1.3$. Thus, the shedding rate does not actually reach twice the oscillation rate until $V_{rn} > 11.5$. This may indicate the presence of a hybrid P+S wake leading to the development of a stable 2P wake. However, the corresponding amplitude and reduced velocities do not agree with Roshko and Williamson's map of vortex synchronization regions [25]. It is also possible that the 2P vortex pair has coalesced into a single disturbance once it reaches the anemometer, thus reducing the measured frequency.

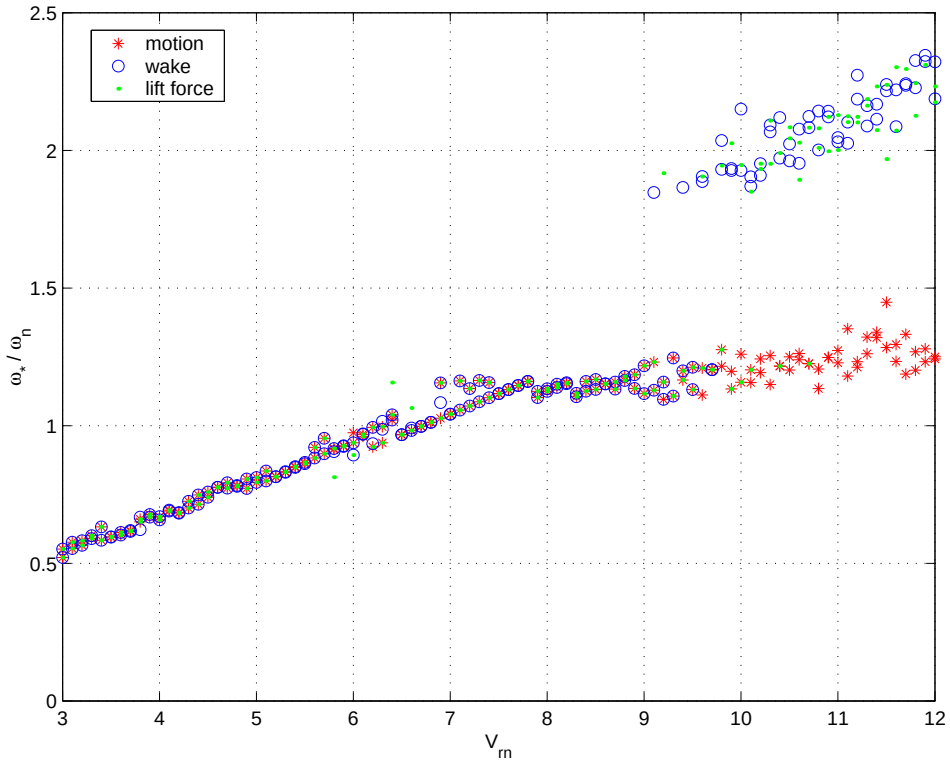

Figure 3-3: Frequency ratio of cylinder motion, lift force, and downstream velocity as functions of reduced velocity. Downstream velocity frequency is measured at $\frac{x}{D} = 2$, $\frac{y}{D} = 2$.

Again, each of the frequencies discussed in this section represent the frequency

with the greatest power spectral density obtained from a fast Fourier transform of the experimental data. Thus, Appendix B provides power spectra of several runs to illustrate the relative intensities of these frequencies and the transition of the lift force and wake velocity frequencies.

Drag

Figure 3-4 presents both mean and fluctuating drag coefficients as functions of reduced nominal velocity. Both plots have a coincident peak centered around $V_{rn} \approx 5.7$. These peaks are also coincident with the amplitude ratio peak of Figure 3-1. Mean drag coefficient exceeds 3.0 and fluctuating drag coefficient approaches 0.7. Thus, during maximum vibration, the cylinder experiences an instantaneous drag force nearly four times that of a stationary cylinder. For reduced velocities characterized by small vibration amplitude, the drag coefficients resemble those of a stationary cylinder experiencing sub-critical flow (i.e. $C_D(mean) \approx 1.3$ and $C_D(std) \approx 0$). So, drag force is seen to be directly proportional to cylinder vibration amplitude. This dependency reveals the fluidelastic behavior that leads to significant vortex-induced vibration. As the amplitude of cylinder vibration grows, so does the strength of shed vortices; which in turn leads to even greater oscillation. The following section illustrates how the strength of the shed vortices is related to the spanwise correlation of the wake.

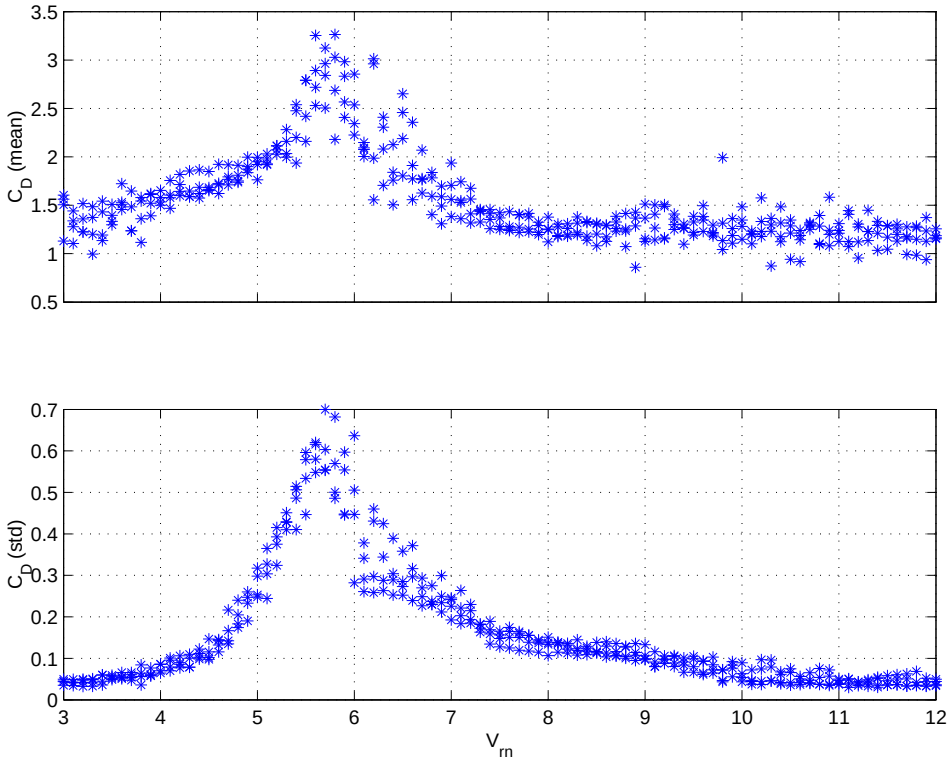

Figure 3-4: Mean and fluctuating drag coefficient as functions of reduced nominal velocity.

Lift

Figure 3-5 shows several lift characteristics of the freely-vibrating cylinder as functions of reduced nominal velocity. The plot of lift coefficient in phase with velocity (Figure 3-5.a) reveals the relation between energy flow and reduced nominal velocity. Initially, C_{LV} increases steadily; reaching a peak near $C_{LV} \approx 0.8$ around $V_{rn} \approx 5.3$. That is, the amount of energy transferred from the fluid to the cylinder increases with motion amplitude. As reduced nominal velocity increases beyond $V_{rn} \approx 5.3$, C_{LV} decreases until plateauing at $C_{LV} \approx -0.1$ for $Vrn > 7$. Here, the direction of energy transfer is reversed and the structure inputs a nominal amount of energy into the fluid. The fluid is responsible for damping the cylinder vibration considerably; preventing self-excitation at these higher reduced nominal velocities.

Mirroring the plot of C_{LV}, Figure 3-5.b shows the trend of lift coefficient in phase with acceleration. After increasing from an initial value of $C_{LA} \approx -1.0$ (corresponding

to an added mass coefficient, $C_M \approx 10.5$) at $V_{rn} = 3$, the plot reaches a peak, coincident with that of C_{LV}, where C_{LA} approaches -3.0 ($C_M \approx 5.7$) around $V_{rn} \approx 5.3 - 5.5$. Thus, the effect of added mass is actually seen to diminish with increasing cylinder vibration amplitude. C_{LA} decreases quickly as reduced nominal velocity is increased further; eventually becoming positive around $V_{rn} \approx 6.5$. Beyond this point, C_{LA} reaches a maximum positive value of $C_{LA} \approx 0.5$ ($C_M \approx -1.4$) near $V_{rn} \approx 7$ before steadily decreasing towards zero. Thus, the vibration at reduced nominal velocities greater than those of the lock-in region (i.e. $V_{rn} > 7$) is characterized by a negative added mass and energy transfer from the cylinder to the fluid. In contrast, the positive added mass and the fluid to structure energy flow are both significant for the sub-lock-in values of V_{rn}.

The phase angle, ϕ, between lift force and cylinder displacement (Figure 3-5.c) exhibits an almost binary behavior. Specifically, phase angle at reduced nominal velocities prior to lock-in ($V_{rn} < 6$) is near to $\phi \approx 0°$. Yet, the phase angle makes a dramatic and sustained shift to $\phi \approx 180°$ within the region $6 < V_{rn} < 7$. This transition provides further evidence of the vortex geometry transition from the 2S to 2P pattern. The trend of end lift force correlation, F_C, (Figure 3-5.d) also reveals the transition between these two regimes. That is, the forcing on the cylinder is well correlated (i.e. $F_C \approx 1$) for both the 2S wake ($3 < V_{rn} < 6$) and the 2P wake ($7 < V_{rn} < 8.5$). However, the vortex-induced forces are uncorrelated as F_C dips toward -1 within the transition region ($6 < V_{rn} < 7$). Also, end force correlation diminishes at higher reduced nominal velocities ($V_{rn} > 8.5$); suggesting the 2P wake becomes less organized.

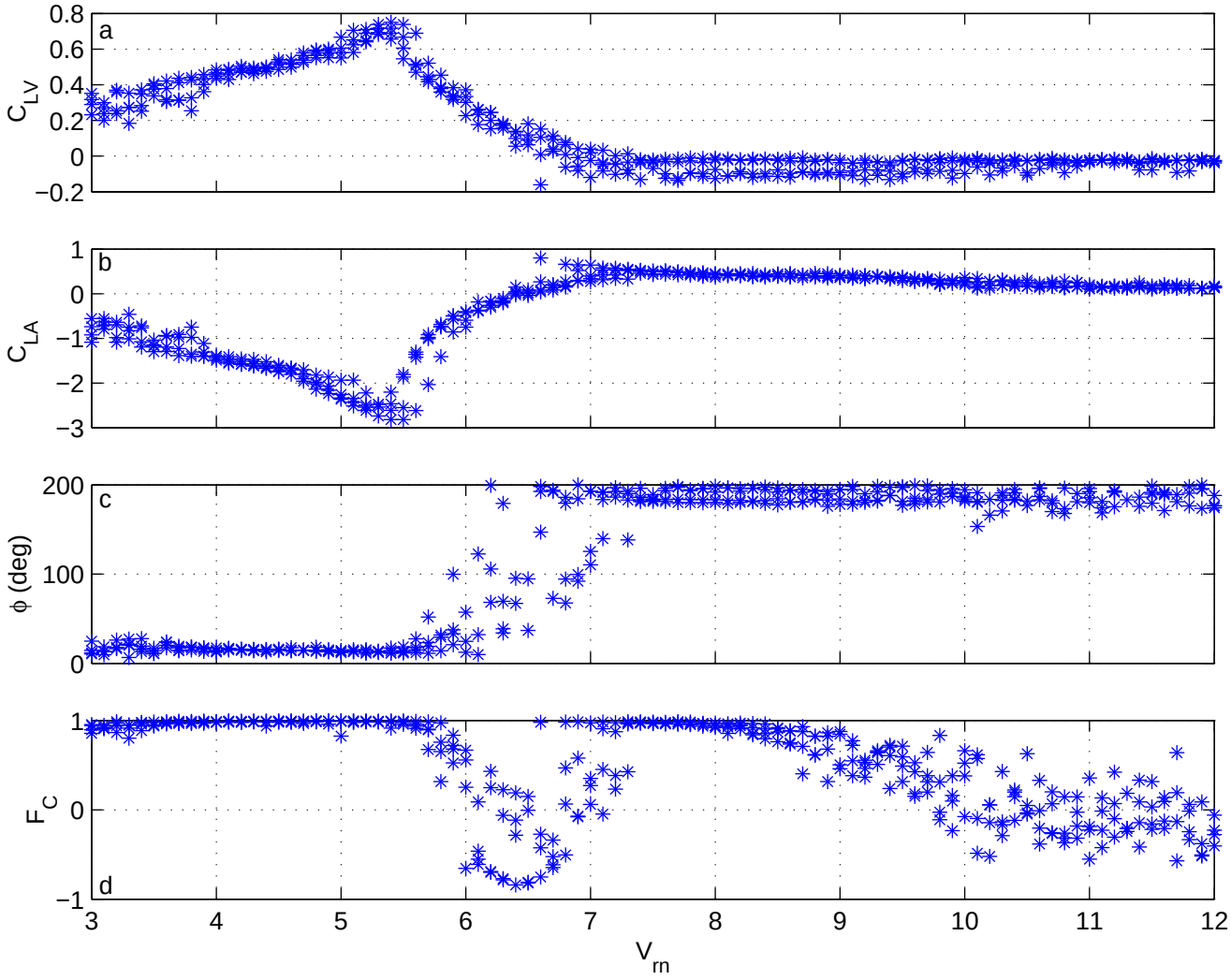

Figure 3-5: Lift characteristics as functions of reduced nominal velocity, including: (a)lift coefficient in phase with velocity, (b)lift coefficient in phase with acceleration, (c)phase angle between lift force and cylinder displacement, and (d)correlation coefficient between end lift forces.

3.2 Wake Characteristics

3.2.1 Spanwise Velocity Correlation

As discussed in Chapter 2, six anemometers in two horizontal arrangements are used to characterize the spanwise correlation of the downstream velocities of an oscillating cylinder. To provide a baseline for these studies, Figure 3-6 presents the velocity correlation coefficient, R_{ij}, as a function of spanwise anemometer separation, $\frac{\delta z}{D}$, for a stationary cylinder. Correlation trends at the three relevant measurement locations are displayed.

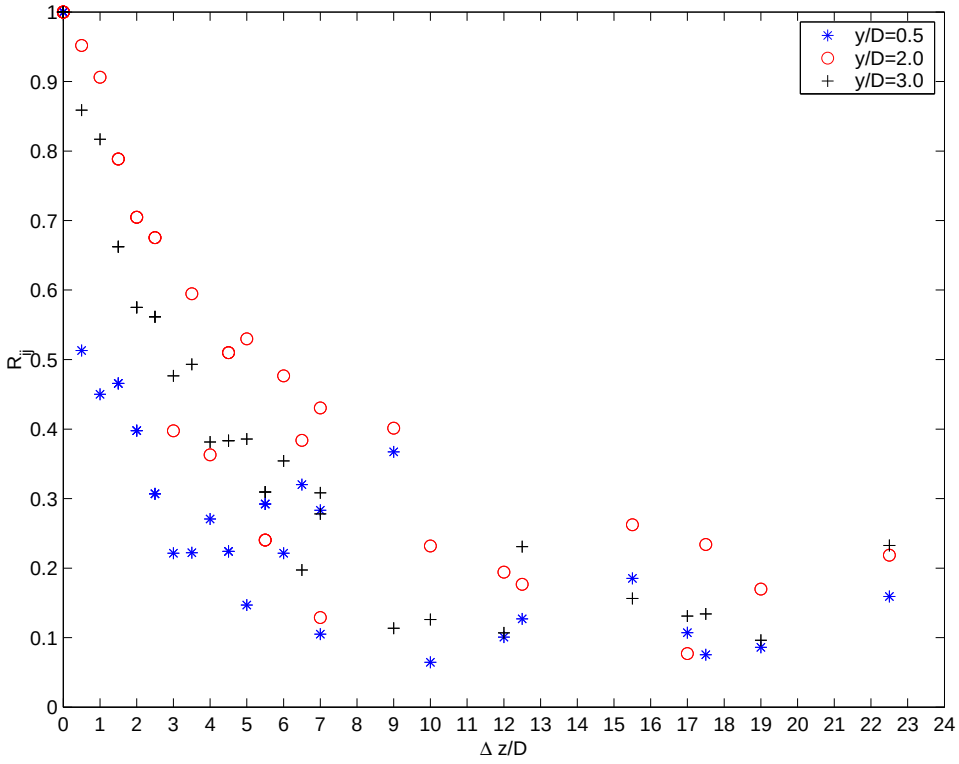

Figure 3-6: Velocity correlation coefficient at various locations downstream of a stationary cylinder as a function of spanwise separation. $\frac{x}{D} = 2.0$ for all cases.

Figure 3-6 illustrates the dependance of velocity correlation on spanwise separation. The plot for each downstream location follows a similar rapidly decreasing exponential curve with increasing separation distance. However, the correlation magnitude is consistently greatest at $\frac{y}{D} = 2.0$ and least at $\frac{y}{D} = 0.5$. This finding supports

elevation - $\frac{y}{D}$	correlation length - $\frac{L}{D}$
0.5	0.25
2	3.0
3	2.0

Table 3.1: Estimated vortex correlation length at various locations downstream of a stationary cylinder. $x/D = 2$ for all cases.

theoretical assertion that the separation layer at the cylinder shoulder is more turbulent than the region outside the immediate wake. Furthermore, the correlation magnitude is greater at $\frac{y}{D} = 2.0$ than at $\frac{y}{D} = 3.0$; suggesting that vortices become disorganized as they dissipate and move away from the cylinder. Here, we employ Hayakawa and Hussain's [6] definition of estimated correlation length, $\frac{L}{D}$. That is, $\frac{L}{D}$ is the separation distance over which correlation coefficient drops by $e^{-}1$, or when $R_{ij} > 0.63$. The resulting estimated correlation lengths are presented in Table 3.2.1. These values closely agree with those provided by Sarpkaya [18]. Herein, the position $\frac{x}{D} = 2, \frac{y}{D} = 2$ will serve as a benchmark for measuring the ultimate correlation of the vortex wake.

Lastly, the correlation magnitude at the greatest measured separation distance, $\frac{\Delta z}{D} = 22.5$ is relatively large for all three wake positions. Because this separation nearly spans the length of the entire cylinder ($AR = 26.2$), the increase in correlation is likely an artifact resulting from the foil struts. Specifically, anemometers located at the cylinder ends may record similar energy from the wake of the heaving foils; artificially amplifying the correlation magnitude. This unavoidable effect is present in all spanwise correlation experiments in this thesis.

The two anemometer arrangements result in 24 spanwise separations for each of the 91 virtual reduced nominal velocities to produce 2184 unique experimental data points for each wake location. Figure 3-7 provides a graphical representation of this test matrix. Two-dimensional interpolation of these experimental points create the correlation and phase difference surfaces of Figure 3-8 through Figure 3-10. These figures provide the spanwise velocity correlation results behind a freely vibrating

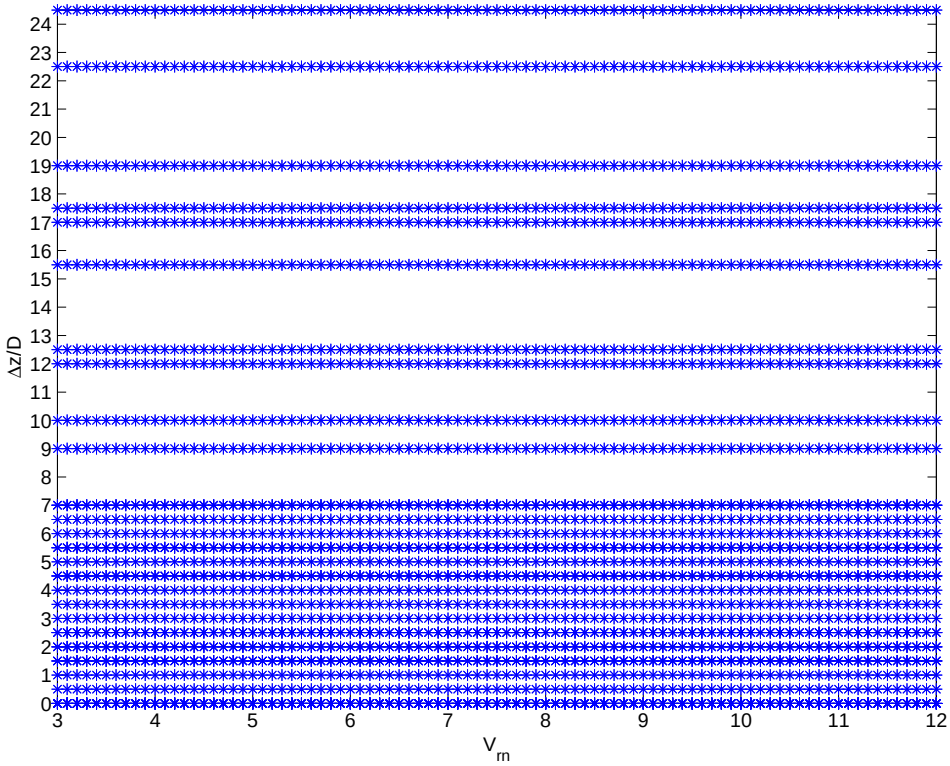

Figure 3-7: Experimental test matrix illustrating spanwise anemometer separations over the range of reduced nominal velocities.

cylinder as contours of R_{ij}. Corresponding results for phase difference, ψ, between anemometers are also provided in each figure. It is important to note that the surfaces in these figures result from both interpolation and two-dimensional, high-order curve fitting in the least squares sense.

Figure 3-8 reveals that the fluid velocities measured downstream from the cylinder shoulder ($\frac{x}{D} = 2.0$, $\frac{y}{D} = 0.5$) are largely uncorrelated. This measurement location is considered to be within the turbulent cylinder wake. Correlation coefficient never exceeds $R_{ij} = 0.6$ for any significant values of spanwise separation. In fact, estimated correlation length does not exceed $\frac{L}{D} \approx 0.5$ for any reduced nominal velocity. Dependance of correlation on spanwise separation is subtly evident as correlation coefficient plummets at small values of $\frac{\Delta z}{D}$. Although, two regions of slightly increased correlation exist as R_{ij} exceeds 0.4 at all separations for $3.5 < V_{rn} < 4.5$ and $R_{ij} > 0.3$ within $7 < V_{rn} < 8$. These regions correspond to relatively moderate cylinder vibration amplitude, $0.2 < \frac{A}{D} < 0.5$ (see Figure 3-1). Overall, the vortices in this

location are turbulent and disorganized, especially when the cylinder is nearly still or vibrating significantly. A notable feature is the isolated $R_{ij} > 0.5$ contour occurring at large separations for $3.8 < V_{rn} < 4.2$. This is likely an effect of the widely spaced anemometers detecting the wake of the foil struts. This region and the few others with increased correlation have corresponding small values of phase difference (Figure 3-8.b). Whereas, the regions of low correlation coefficient are characterized by phase difference values $\psi > 90°$.

In contrast to the fluid velocities downstream of the cylinder shoulder, those measured 2 diameters above the cylinder axis are significantly correlated. As theoretically predicted, the flow structure is more organized outside of the turbulent cylinder wake. Figure 3-9 shows that the flow at $\frac{x}{D} = 2.0$, $\frac{y}{D} = 2.0$ is fully correlated along the entire span for certain reduced nominal velocities. Specifically, the velocity correlation coefficient exceeds $R_{ij} = 0.6$ for all separation distances within $3.6 < V_{rn} < 5.6$ and $7.0 < V_{rn} < 8.8$ Here, the estimated correlation length actually exceeds the length of the cylinder (i.e. $\frac{L}{D} > 26$). These correlation peaks are coincident with the smaller ones seen at the cylinder shoulder in Figure 3-8. Thus, maximum vortex correlation is seen to develop under moderate vibration amplitudes, $0.2 < \frac{A}{D} < 0.5$. The first correlated region, $3.6 < V_{rn} < 5.6$, has values of R_{ij} exceeding 0.9 at separations greater than $\frac{\Delta z}{D} \approx 22$; suggesting that the 2S wake is highly stable. Whereas, the second correlation region, $7.0 < V_{rn} < 8.8$, has a large contour of $R_{ij} > 0.8$ at large separation distances; indicating that the 2P wake pattern is also well organized along the span. The transition zone between these two highly correlated regions is characterized by relatively low values of velocity correlation coefficient; $R_{ij} > 0.5$ for $\frac{\Delta z}{D} > 5$. This region is interesting because it contains the frequency lock-in, the greatest motion amplitudes, as well as the phase angle transition and the end force correlation drop indicative of the vortex pattern transformation. Our results conflict with Ramberg and Griffin [17], who observed the greatest correlation within the lock-in region. We hypothesize that the fluid is unable to remain organized as turbulence develops under the vigorous cylinder oscillations. The fluid does not become reorganized until vibration amplitude decreases and the 2P pattern fully develops. Also,

within the transition region, a clear dependence of velocity correlation on spanwise separation is evident and correlation length is estimated to be $\frac{L}{D} \approx 3.5$. At low reduced nominal velocities ($V_{rn} < 3.6$) characterized by small amplitude vibrations, the velocities are moderately correlated with an estimated correlation length of $\frac{L}{D} \approx 10$. Although similar amplitude vibrations exist for $V_{rn} > 8.8$, the velocities in this region are uncorrelated with an estimated correlation length of only $\frac{L}{D} \approx 2$. This dichotomy suggests a direct relationship between motion frequency, vortex wake pattern, and spanwise velocity correlation. Overall, these results closely agree with those of Novak and Tanaka[15] and Hayakawa and Hussain[6].

Furthermore, comparison of the correlation coefficient and phase difference results at this location (Figure 3-9.b) reveals that the areas of lowest phase difference are coincident with the areas of greatest correlation. This association provides evidence for Szepessy's assertion[20] that increased correlation results from coherent phasing of spanwise vortex structures. Limited motion of the cylinder organizes turbulent, out-of-phase structures at the cylinder's shoulder into in-phase vortex sheets correlated along the cylinder's span outside of the immediate wake.

Figure 3-10 illustrates that the velocity correlation at $\frac{x}{D} = 2.0, \frac{y}{D} = 3.0$ is similar to that at $\frac{x}{D} = 2.0, \frac{y}{D} = 2.0$. Although correlation coefficient magnitudes are somewhat reduced, two similar regions exist where correlation length extends over the entire cylinder span. The key similarity is the reduction in correlation within the lock-in region where vibration amplitude is greatest ($5.6 < V_{rn} < 7.0$). The presence of this degradation at a location sufficiently far from the cylinder wake proves that it is not an artifact of anemometer probes entering the turbulent zone at high motion amplitudes. Thus, the breakdown of spanwise correlation for large vibration is maintained throughout the downstream region. Correlation coefficient magnitude is less at a location further from the wake likely because of vortex diffusion.

The final set of figures in this subsection (Figure 3-11.a-c) provides the unwrapped phase angle, θ, between the cylinder displacement and anemometers located 0, 2.5, and 5 diameters, spanwise, from the midpoint. The differences between the individual anemometers are small compared to the large scale trends of each figure. For example,

Figure 3-11.a shows that the each of the phase angles at $\frac{x}{D} = 2.0, \frac{y}{D} = 0.5$ is near $\theta \approx 100°$ for $3.0 < V_{rn} < 6.5$. However, the plot makes an abrupt jump as values of θ approach $9000°$ within $6.5 < V_{rn} < 8.0$. This phenomenon is probably an artifact of the anemometers at this location being exposed to the vortices shed from both sides of the cylinder during large vibrations. At greater reduced nominal velocities, the phase angles return to $\theta \approx 100°$ before increasing to $\theta \approx 2000°$ around $V_{rn} \approx 10.0$. Figures 3-11.b and 3-11.c show a similar trend outside of the wake; where phase angles increase significantly at $V_{rn} > 9$. This increase corresponds to the doubling of measured wake frequency (Figure 3-3) and likely results from the vortex pattern transition.

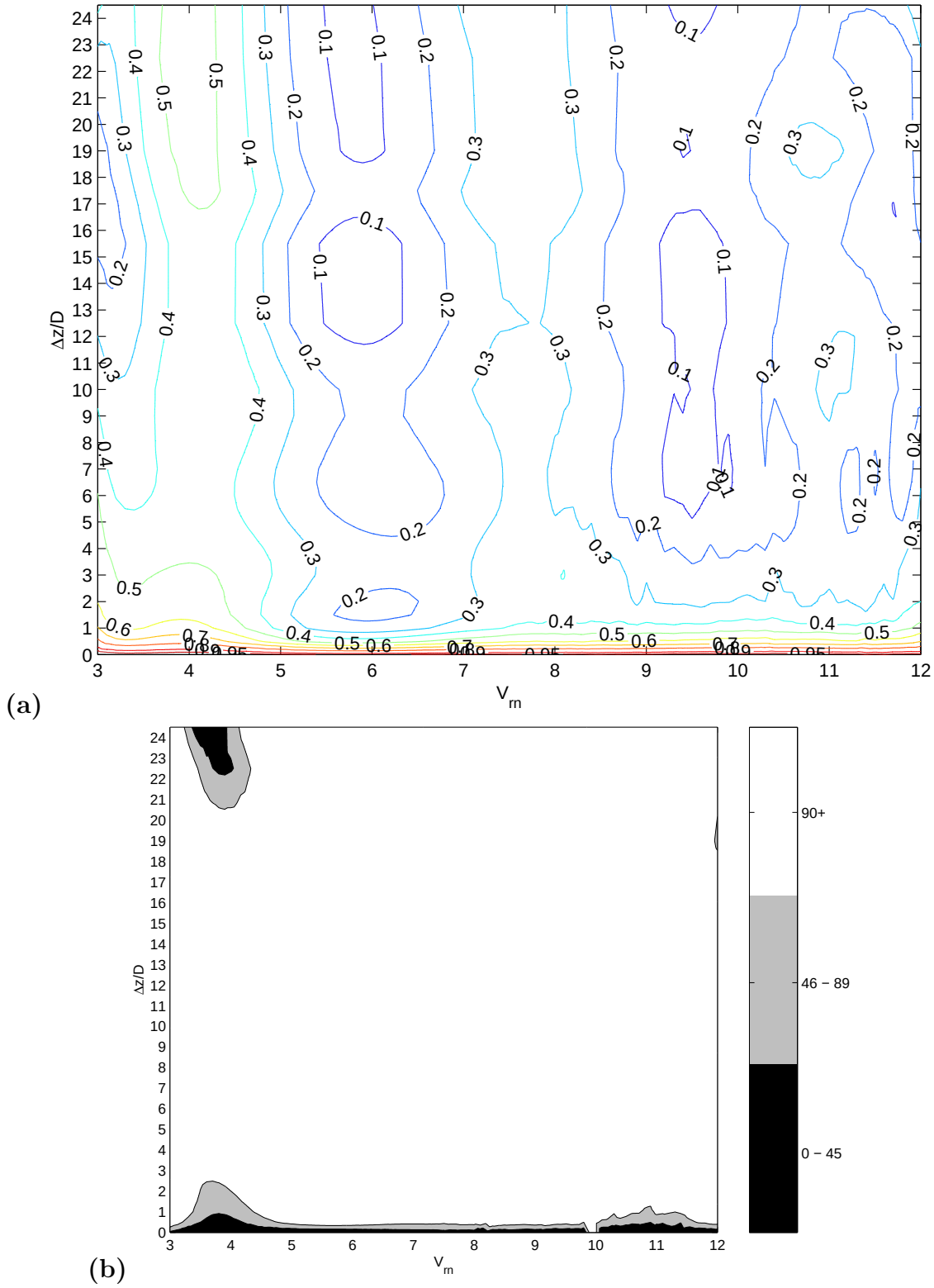

Figure 3-8: (a) Velocity correlation coefficient, R_{ij}, and (b) phase difference, ψ, surfaces as functions of spanwise separation and reduced nominal velocity at $\frac{x}{D} = 2.0$, $\frac{y}{D} = 0.5$.

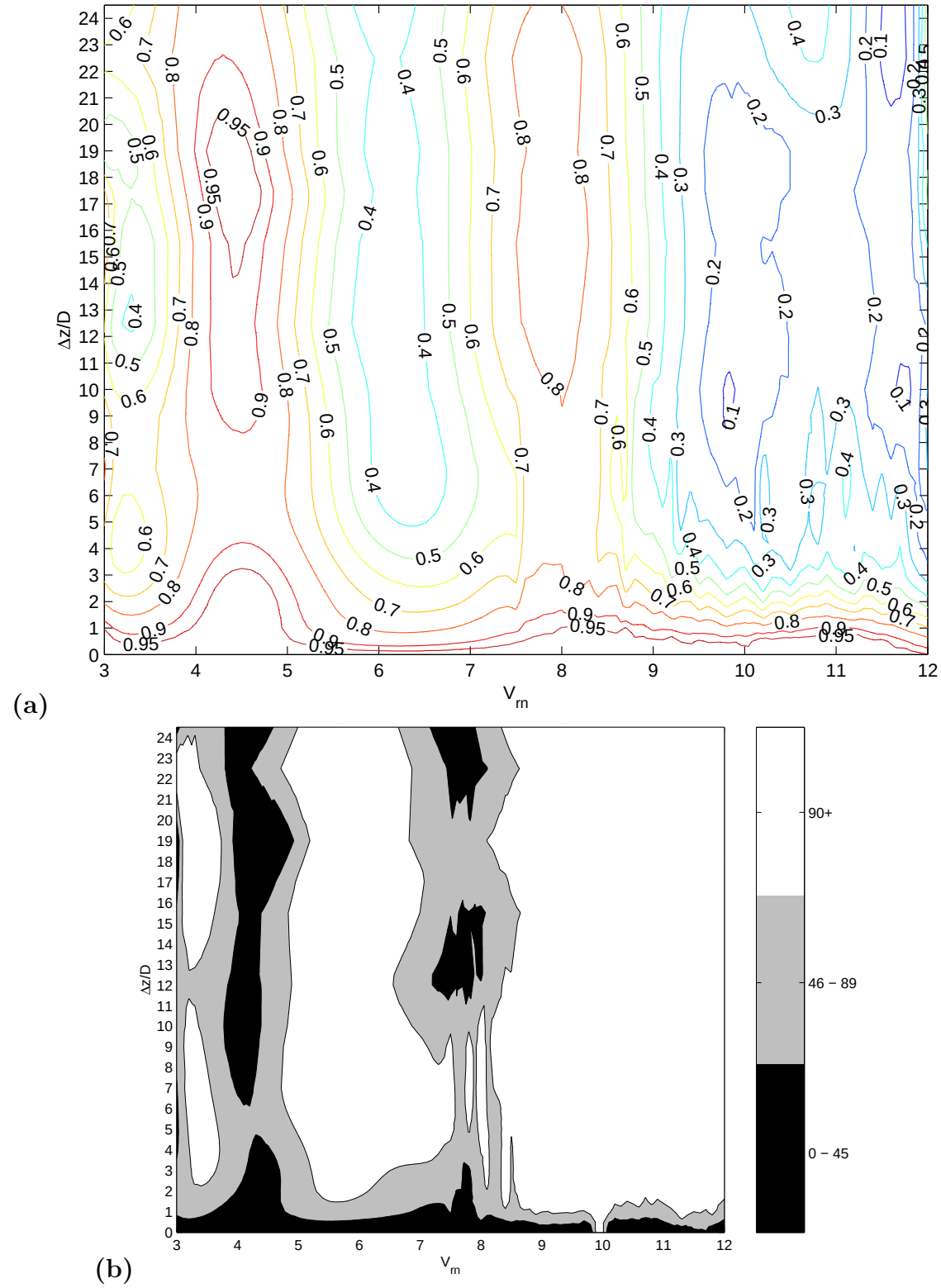

Figure 3-9: (a) Velocity correlation coefficient, R_{ij}, and (b) phase difference, ψ, surfaces as functions of spanwise separation and reduced nominal velocity at $\frac{x}{D} = 2.0$, $\frac{y}{D} = 2.0$.

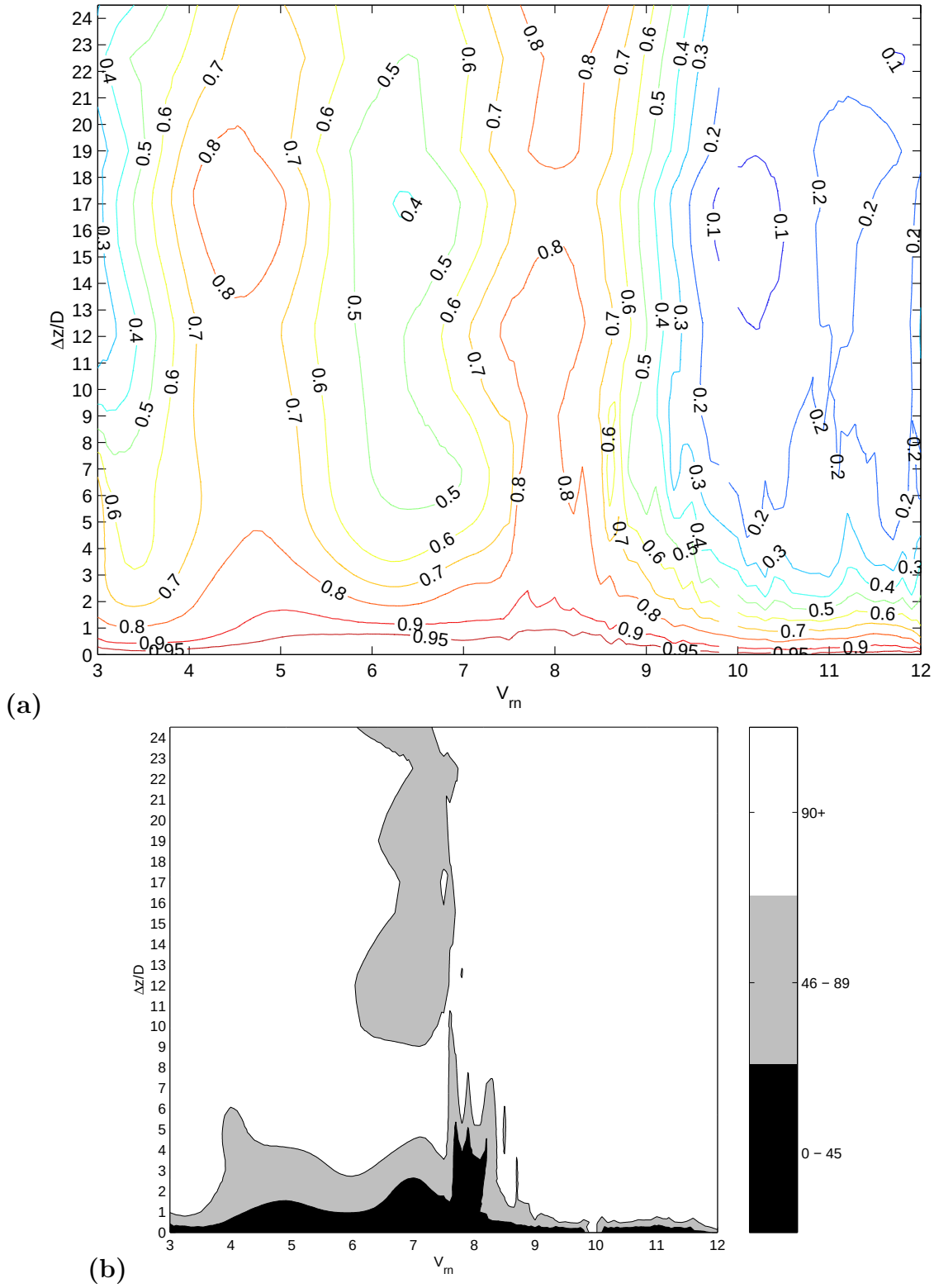

Figure 3-10: (a) Velocity correlation coefficient, R_{ij}, and (b) phase difference, ψ, surfaces as functions of spanwise separation and reduced nominal velocity at $\frac{x}{D} = 2.0$, $\frac{y}{D} = 3.0$.

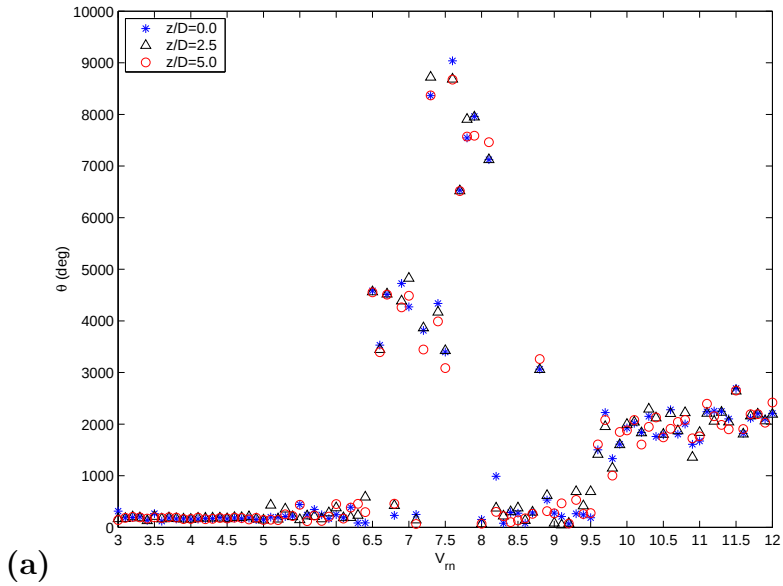

(a)

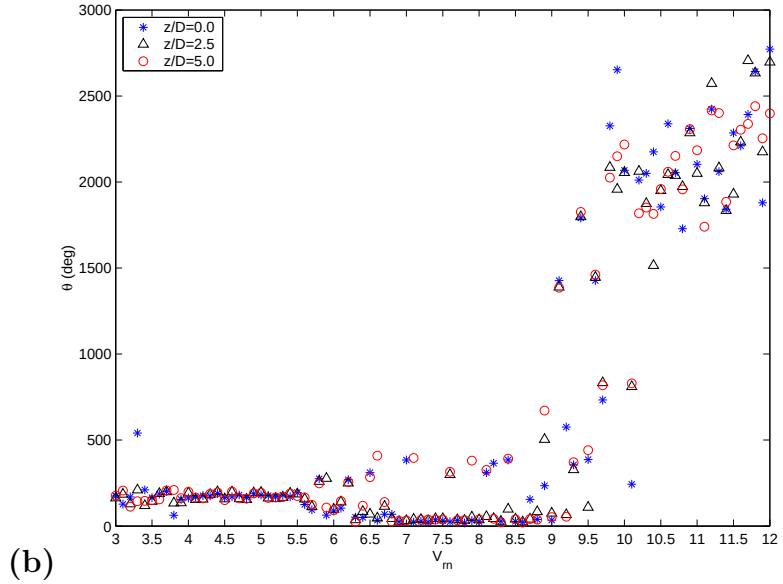

(b)

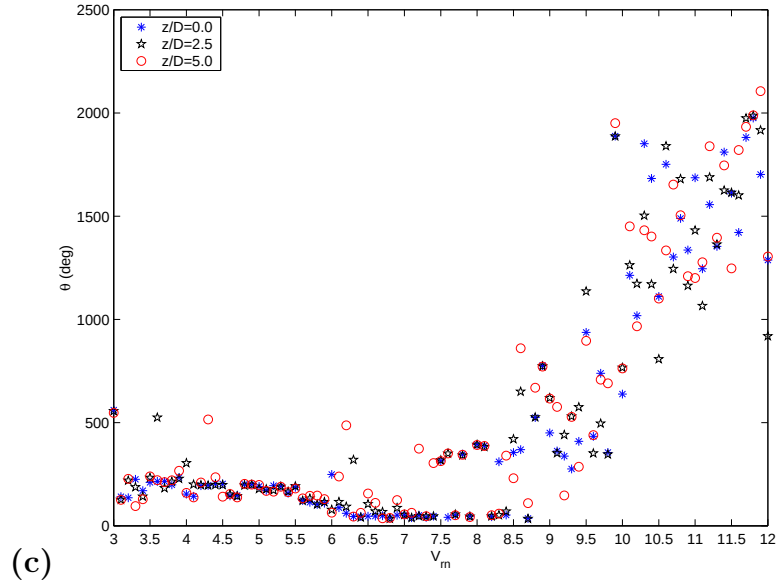

(c)

Figure 3-11: Phase difference, θ, between cylinder displacement and anemometer signals at $x/D = 2.0$ and (a)$y/D = 0.5$, (b)$y/D = 2.0$, (c)$y/D = 3.0$ as a function of reduced nominal velocity.

3.2.2 Downstream Velocity Profile

Figures 3-12.a and b show the mean velocity profile of a freely vibrating cylinder measured downstream at 2 diameters and at 5 diameters, respectively. Each of the figures also provides the profile for a stationary cylinder at that location; labeled "STILL". Eighteen reduced nominal velocities ($V_{rn} = 3.3 : 0.5 : 11.8$) are employed in the simulation for the free vibration study. The amplitudes and frequencies observed are also used in the forced vibration study and are presented in Table 4.2. Each profile is normalized by the free stream velocity; creating the repetitive top axis tickmarks, $\frac{U_{mean}}{U_o} = [0, .5, 1]$. Because measurements are only taken above the cylinder, the profiles are artificially mirrored about the plane of symmetry for clarity. Also, the soiled line is a high-order polynomial fitting the actual data points (+).

At 2 diameters downstream, the downstream velocity defect for all cases is situated within $-2 < \frac{y}{D} < 2$. Thus, the mean velocity outside of this region results primarily from the free stream. As the cylinder begins to oscillate at low reduced nominal velocities, the shape of the profile resembles that of the stationary cylinder. However, the depth of the velocity defect grows up to $V_{rn} = 4.8$, where $\frac{U_{mean}}{U_o} \approx 0.5$ at $\frac{y}{D} = 0$. At $V_{rn} = 5.3$, the profile changes shape as the mean velocity at $\frac{y}{D} = 0$ exceeds that at $\frac{y}{D} = 0.5$. This inverted geometry, resulting from the powerful vortices accompanying large vibration, continues up to $V_{rn} = 8.8$. These vortices even cause $\frac{U_{mean}}{U_o}$ to exceed unity around $\frac{y}{D} \approx 2$ for the greatest motion amplitudes. At higher values of V_{rn}, the inversion disappears and the profile again resembles that of the stationary cylinder. This figure also confirms that the positions $\frac{x}{D} = 2.0, \frac{y}{D} = 2.0$ and $\frac{x}{D} = 2.0, \frac{y}{D} = 3.0$, used in the spanwise correlation study, are outside the immediate cylinder wake.

Figure 3-12 shows little change in the velocity profile geometry further downstream at $\frac{x}{D} = 5$. The profiles are more uniform; indicating a reduction in strength of the velocity defect. Furthermore, the inversion, where the mean velocity at $\frac{y}{D} = 0$ exceeds that at $\frac{y}{D} = 0.5$, exists at only a few reduced nominal velocities ($5.3 < V_{rn} < 6.8$). Thus, the vortices loose strength as they diffuse further downstream of the cylinder. Also, the wake width is not noticeably greater at this location than at $\frac{x}{D} = 2$.

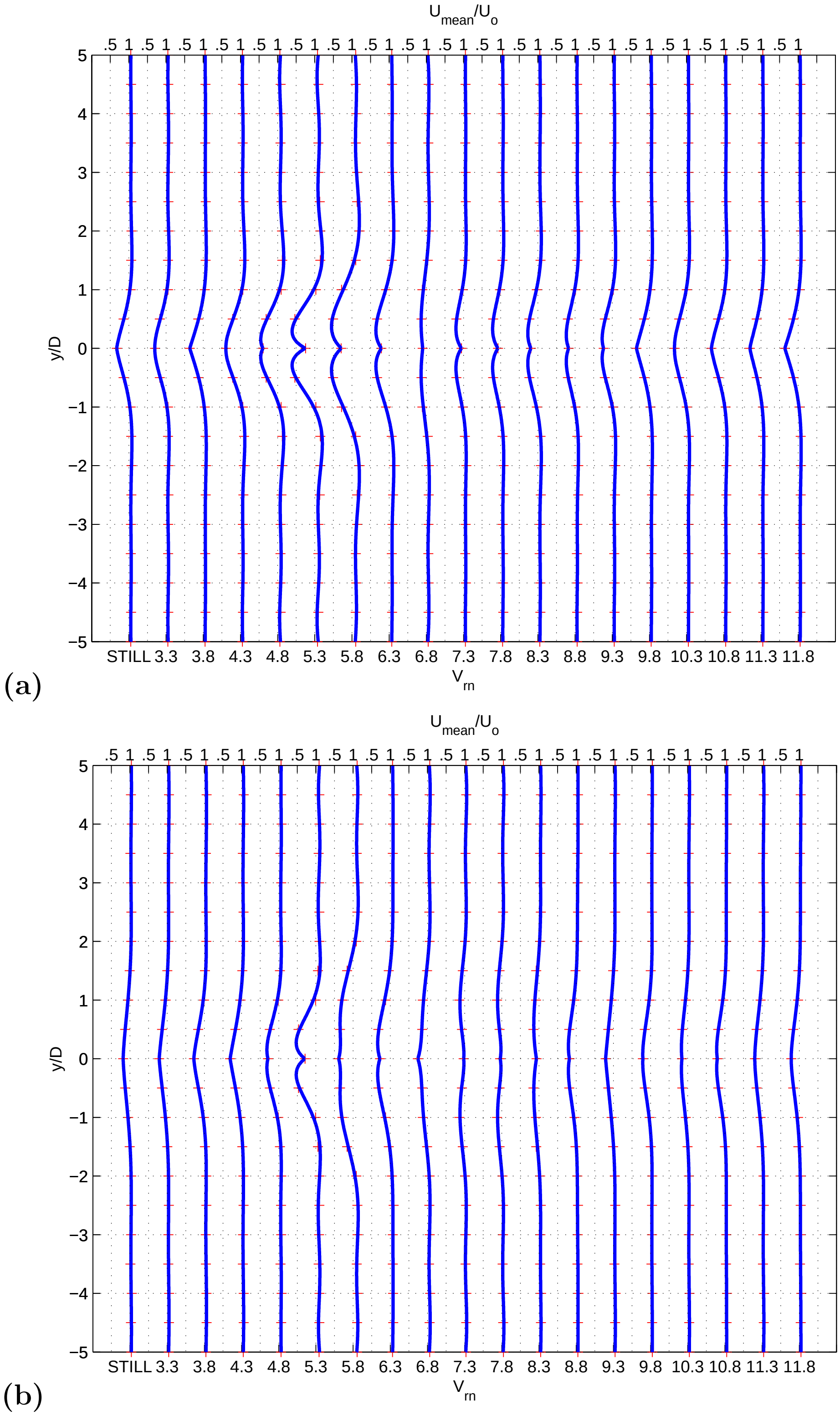

Figure 3-12: Mean velocity profile downstream of a freely vibrating cylinder measured at (a)$\frac{x}{D} = 2$ and (b)$\frac{x}{D} = 5$.

Chapter 4

Forced Vibration Results

4.1 Vibration Dynamics

4.1.1 Spanwise Velocity Correlation

In order to compare the spanwise velocity correlation of a freely-vibrating cylinder and that of a cylinder experiencing forced vibrations, sinusoidal oscillations were imparted to the cylinder at amplitudes and frequencies near to those seen in the free vibration experiments. Specifically, VCTA forced the cylinder at four amplitude levels within three frequency, or reduced velocity regimes. Table 4.1 details the oscillation amplitude ratios used at the different amplitude levels and frequency regimes. Also, Figure 4-1 compares the forced vibration parameters with the previously discussed free vibration results.

	Frequency Regime		
	A	**B**	**C**
Amplitude Level	$V_r = 5.2 - 7.1$	$V_r = 6.7 - 8.3$	$V_r = 8.1 - 10.0$
1	0.2	0.35	0.1
2	0.5	0.45	0.2
3	0.8	0.55	0.3
4	1.1	0.65	0.4

Table 4.1: Amplitude Ratio, $\frac{A}{D}$, at different amplitude levels and frequency regimes for forced vibration spanwise correlation study.

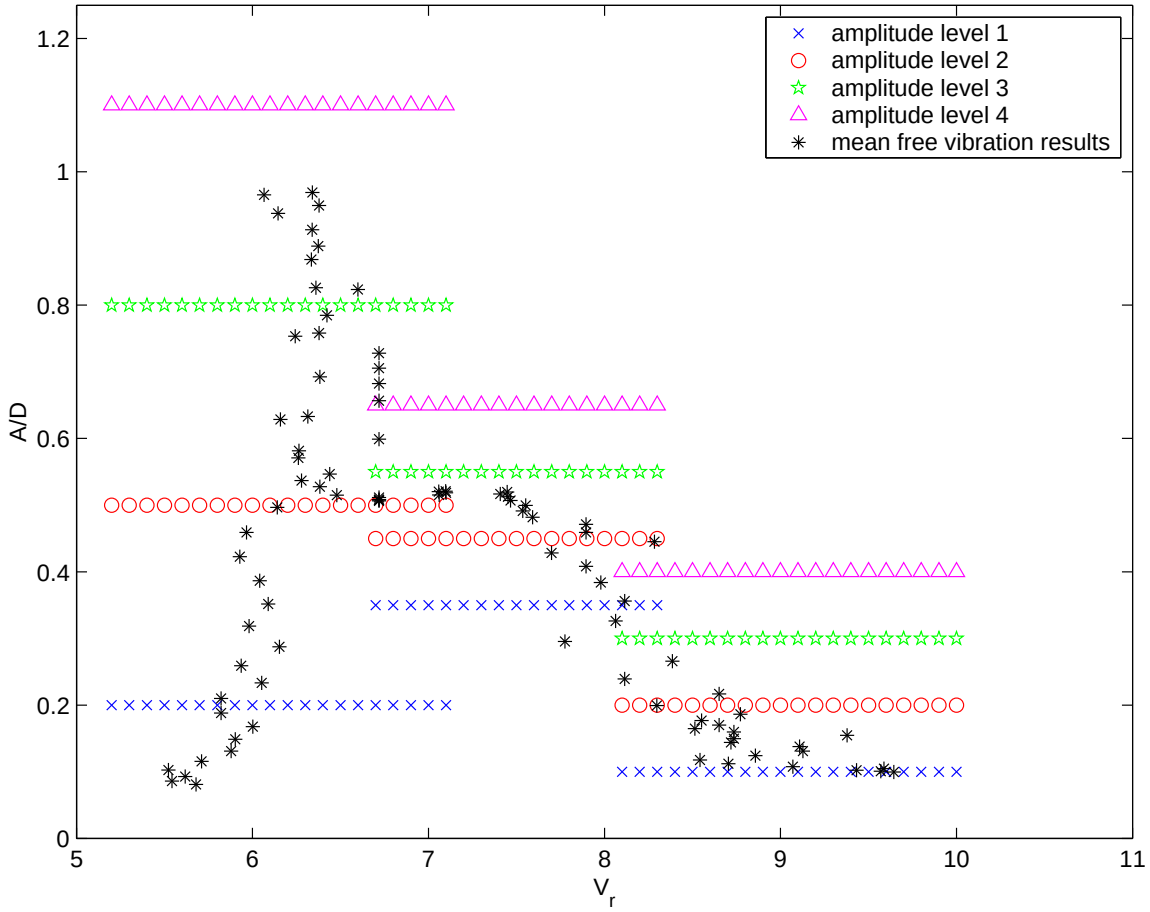

Figure 4-1: Amplitude ratio as a function of reduced velocity for both free and forced vibration spanwise correlation studies.

4.1.2 Downstream Velocity Profile

For the velocity profile experiments, the amplitudes and frequencies of a freely vibrating cylinder were recorded and played back sinusoidally. Table 4.2 provides the amplitudes and frequencies observed at each reduced nominal velocity and then applied for forced vibration. Although reduced nominal velocity is not directly relevant to forced motion, values of V_{rn} are provided for comparison with free vibration results.

Vrn	A/D	ω (rad/s)
3.3	0.10	5.97
3.8	0.19	5.67
4.3	0.32	5.52
4.8	0.50	5.37
5.3	0.76	5.17
5.8	0.97	5.20
6.3	0.78	5.14
6.8	0.66	4.91
7.3	0.53	5.17
7.8	0.51	4.91
8.3	0.52	4.43
8.8	0.49	4.38
9.3	0.43	4.30
9.8	0.30	4.24
10.3	0.19	3.77
10.8	0.15	3.52
11.3	0.12	3.73
11.8	0.10	3.50

Table 4.2: Velocity profile study motion parameters observed in free vibration and later used for forced motion.

4.2 Wake Characteristics

4.2.1 Spanwise Velocity Correlation

This section includes summary figures providing the forced motion results as functions of reduced velocity, V_r. Each figure includes three subplots; the first shows contours of spanwise velocity correlation coefficient (R_{ij}) as functions of spanwise separation ($\frac{\Delta z}{D}$), the second shows mean drag coefficient ($C_D(mean)$) and fluctuating drag coefficient ($C_D(std)$), and the third shows lift coefficient in phase with velocity (C_{LV}) and acceleration (C_{LA}), and phase angle (ϕ) between cylinder displacement and lift force. Figure 4-2 through Figure 4-13 refer to the velocity measurements taken outside the wake at $\frac{x}{D} = 2.0$, $\frac{y}{D} = 2.0$. Likewise, Figure 4-14 through Figure 4-25 refer to the velocity measurements taken within the wake at $\frac{x}{D} = 2.0$, $\frac{y}{D} = 0.5$. Each figure's

caption provides the corresponding amplitude level and frequency regime.

Velocity measurements outside the wake ($\frac{x}{D} = 2.0$, $\frac{y}{D} = 2.0$)

Frequency regime *A* - Figures 4-2 through 4-5 Focusing on the velocity measurements taken outside of the wake, several trends are evident. Within frequency regime A, spanwise correlation, R_{ij}, exhibits little dependence on spanwise septation, $\frac{\Delta z}{D}$. That is, the downstream velocities are either correlated along the entire span or almost completely uncorrelated. The range of reduced velocities for which the downstream velocity is well correlated clearly depends on the forcing amplitude. Specifically, the estimated correlation length extends over the entire span for reduced velocities: $5.3 < V_r < 6.0$ at amplitude level *1*, $5.3 < V_r < 6.3$ and $6.7 < V_r < 7.1$ at amplitude level *2*, and over the entire frequency regime A ($5.3 < V_r < 7.1$) at amplitude level *3*. Thus, the range of vibration frequencies characterized by well correlated downstream velocities extends with greater motion amplitude. However, as amplitude ratio exceeds unity (amplitude level *4*), the correlation coefficient drops ubiquitously and estimated correlation length reaches a maximum of $\frac{L}{D} \approx 10$. As also observed in the free vibration results, the flow remains organized along the entire span only under some threshold vibration amplitude. Furthermore, this frequency regime contains the largest ranges of reduced velocities with full-span correlation lengths. These vibration frequencies, slightly above that of the lock-in reduced velocity $V_r \approx 6.7$, are especially conducive to coherent vortex sheet formation.

As expected, both mean and fluctuating drag increase with vibration amplitude. Both coefficients remain fairly constant at all reduced velocities except at amplitude level *4*, where $C_D(mean)$ drops from values greater than 3.0 to less than 2.0 over $V_r \approx 6.1 - 6.4$. This region also includes a shift in phase angle, observed at all amplitude levels, from $\phi \approx 0$ to $\phi \approx 180$; signaling the 2S to 2P vortex geometry transition. Also, C_{LV} exhibits a similar trend at all amplitude levels; characterized by slightly negative or near zero values for $V_r < 5.8$ and $V_r > 6.4$. The coincidence of these regions of slightly negative C_{LV} with the regions of greatest spanwise velocity correlation suggests a connection between power flux and spanwise correlation. The

plot of C_{LA} is also similar for each amplitude level as the coefficient is negative at low values of V_r before growing to positive values at $V_r > 6.2$. The ultimate magnitudes of this coefficient increase with vibration amplitude (i.e. minimum $C_{LA} \approx -4.0$ at amplitude levels *3* and *4*). Because the maximum instantaneous acceleration increases at each amplitude level, so does the added mass.

Frequency regime *B* - Figures 4-6 through 4-9 The evolution of spanwise velocity within frequency regime B is unique. At amplitude level *1*, the spanwise velocities are largely uncorrelated and estimated correlation length reaches a maximum of only $\frac{L}{D} \approx 3$. Such disorganization is interesting because the amplitude ratio, $\frac{A}{D} = 0.35$, is comparable to those that produce high correlation in frequency regime A. However, regions of full-span correlation length develop at the three higher amplitude levels, spanning: $6.7 < V_r < 7.2$ at amplitude level *2*, $6.8 < V_r < 7.5$ at amplitude level *3*, and $6.7 < V_r < 7.7$ at amplitude level *4*. Again, greater motion amplitude encourages correlation, but a minimum frequency threshold is evident at $V_r \approx 7.7$ ($\omega_o = 4.28$).

Mean drag coefficient remains near $C_D(mean) \approx 1.3$ and fluctuating drag coefficient is almost zero at all amplitude levels. The two lift coefficients and the phase angle between cylinder displacement and lift force, ϕ, exhibit a similar uniformity; all remain near zero throughout.

Frequency regime *C* - Figures 4-10 through 4-13 The downstream velocities all four amplitude levels within frequency regime C are largely uncorrelated. Estimated correlation length does not exceed, $\frac{L}{D} \approx 3$. The oscillation frequencies in this regime are less than 65% of the Strouhal shedding frequency for a stationary cylinder. So, forcing at such an unnatural frequency prohibits the coherent phasing of spanwise vortex structures. The effect of the foil strut wake is seen at amplitude level *3*, where relatively high values of correlation coefficient ($R_{ij} > 0.5$) are isolated at large separation distances ($\frac{\Delta z}{D} > 20$). Hence, this effect demonstrates some dependence on vibration amplitude.

As with frequency regime B, mean and fluctuating drag coefficient stay near stationary cylinder values ($C_D(mean) \approx 1.3$ and $C_D(std) \approx 0.1$). Both C_{LA} and C_{LV} linger close to zero. Phase angle, ϕ, also remains near zero at amplitude levels *1* and *2*. However, instability in the vortex geometry is evident as phase angle fluctuates between $\phi \approx 0^\circ$ and $\phi \approx -100^\circ$ at amplitude level *3*. At amplitude level *4*, phase angle shifts from $\phi \approx 0^\circ$ to $\phi \approx 200^\circ$ around $V_r \approx 8.8$. Referencing Williamson and Roshko's map of vortex synchronization [25], we hypothesize that this phase shift likely represents a transformation from a non synchronized vortex pattern to the 2P pattern.

Velocity measurements within the wake ($\frac{x}{D} = 2.0$, $\frac{y}{D} = 0.5$)

Frequency regime *A* - Figures 4-14 through 4-17 As compared to the same measurements taken outside of the wake, correlation of the downstream velocities in this regime is significantly reduced. However, regions of full-span correlation length do exist at some reduced velocities. Specifically, the spanwise correlation coefficient exceeds $R_{ij} > 6$ over $5.2 < V_r < 5.7$ at amplitude level *1*, and over $5.2 < V_r < 5.9$ at amplitude level *2*. Such correlation is unique because no significant correlation is observable downstream of the shoulder of a freely vibrating cylinder. Thus, the consistent sinusoidal motion likely creates well organized vortices of uniform strength. However, this trend does not extend to higher amplitudes; as seen by the lack of correlation at amplitude levels *3* and *4*. Thus, spanwise correlation is greatest during forced vibration and further amplified by moderate amplitude oscillations near the Strouhal shedding frequency.

The lift and drag coefficient trends are obviously the same for this velocity measurement location. Though, it is interesting that the regions of full-span correlation length coincide with slightly negative values of C_{LV}.

Frequency regime *B* - Figures 4-18 through 4-21 Spanwise velocity correlation is all but non existent in this region. No consistent correlation length is discernable. The full-span correlation lengths seen outside of the wake are not existent

within. As seen in the free vibration study, organization of the flow along the span occurs primarily outside of the turbulent cylinder wake.

Frequency regime *C* - Figures 4-22 through 4-25 As with the measurements taken outside the wake for this frequency regime, the downstream velocities are completely uncorrelated at all amplitude levels.

4.2.2 Downstream Velocity Profile

The mean velocity profiles recorded during forced vibration (Figure 4-26) are nearly identical to those recorded during free vibration (Figure 3-12). The velocity defect geometry resembles that of the stationary cylinder at all reduced nominal velocities except those with the greatest motion amplitude. An inversion, where the mean velocity at $\frac{y}{D} = 0.0$ exceeds that at $\frac{y}{D} = 0.5$, is also existent during forced vibration. However, the magnitude of the inversion and the range of affected reduced nominal velocities ($4.8 < V_{rn} < 6.8$) are both less for forced vibrations than the corresponding free vibrations. This small effect may result from the absence of sporadic vortices of increased strength during forced motion. Again, the wake is confined to $-2.0 < \frac{y}{D} < 2.0$ at both downstream locations.

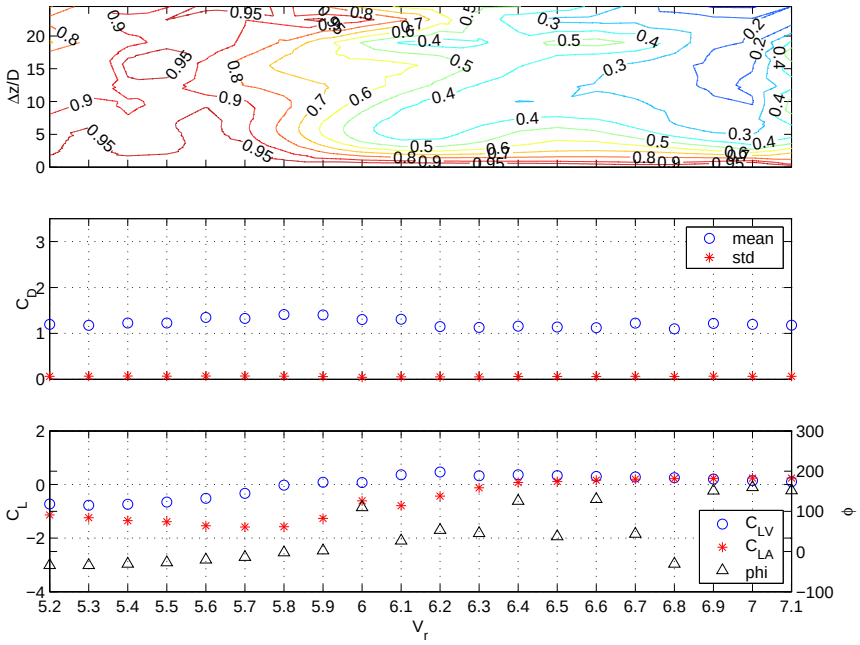

Figure 4-2: Summary of results outside the wake at $\frac{x}{D} = 2.0$, $\frac{y}{D} = 2.0$ for amplitude level *1* ($\frac{A}{D} = 0.2$) within frequency regime A.

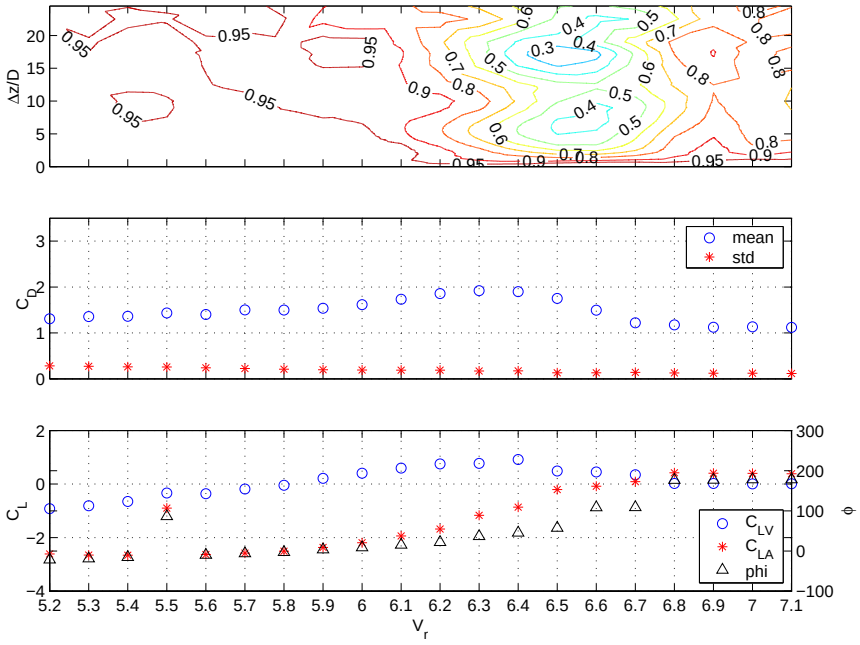

Figure 4-3: Summary of results outside the wake at $\frac{x}{D} = 2.0$, $\frac{y}{D} = 2.0$ for amplitude level *2* ($\frac{A}{D} = 0.5$) within frequency regime A.

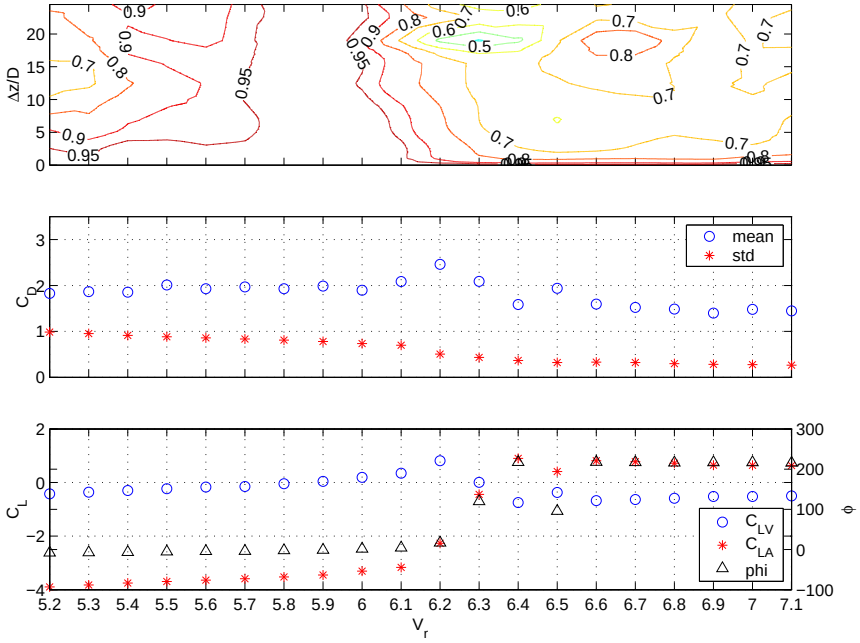

Figure 4-4: Summary of results outside the wake at $\frac{x}{D} = 2.0$, $\frac{y}{D} = 2.0$ for amplitude level *3* ($\frac{A}{D} = 0.8$) within frequency regime A.

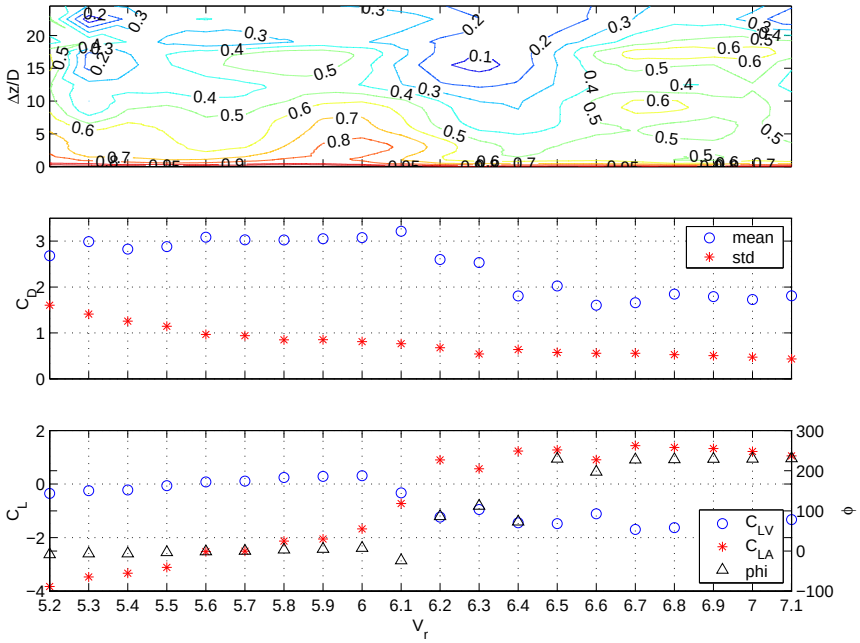

Figure 4-5: Summary of results outside the wake at $\frac{x}{D} = 2.0$, $\frac{y}{D} = 2.0$ for amplitude level *4* ($\frac{A}{D} = 1.1$) within frequency regime A.

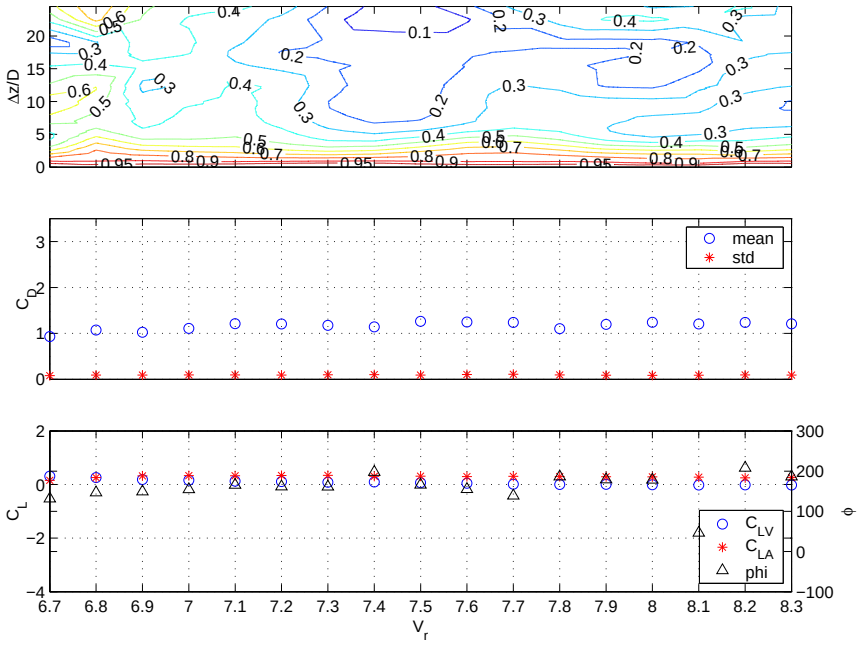

Figure 4-6: Summary of results outside the wake at $\frac{x}{D} = 2.0$, $\frac{y}{D} = 2.0$ for amplitude level *1* ($\frac{A}{D} = 0.35$) within frequency regime *B*.

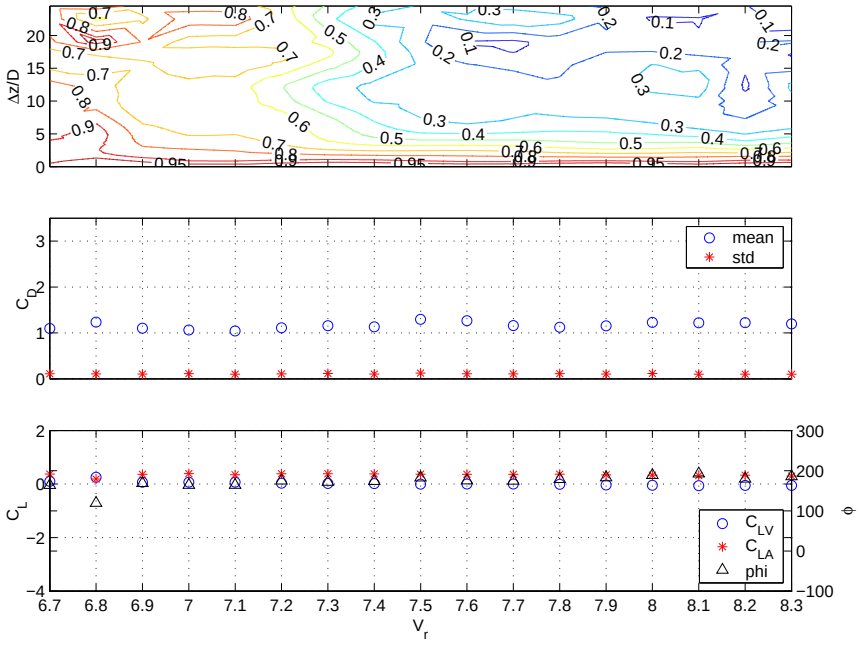

Figure 4-7: Summary of results outside the wake at $\frac{x}{D} = 2.0$, $\frac{y}{D} = 2.0$ for amplitude level *2* ($\frac{A}{D} = 0.45$) within frequency regime *B*.

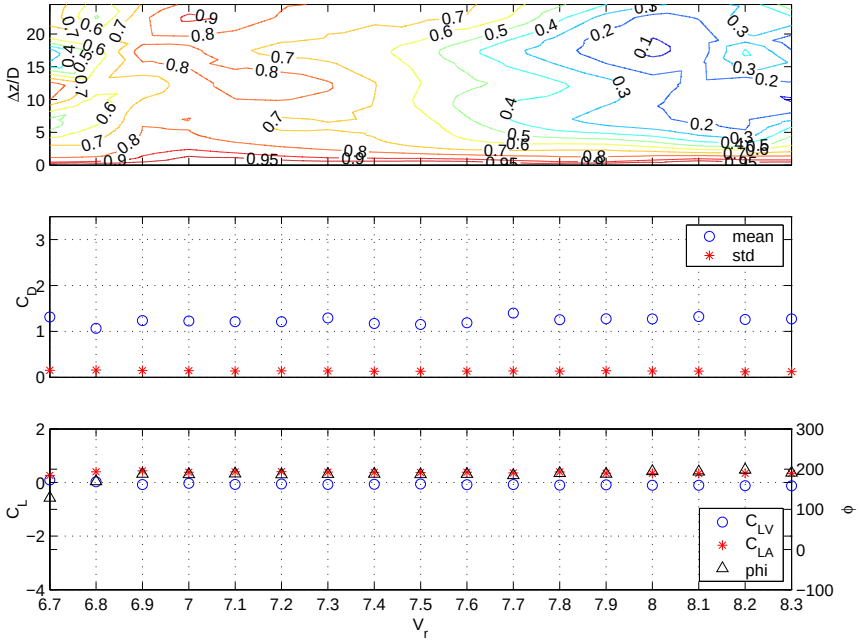

Figure 4-8: Summary of results outside the wake at $\frac{x}{D} = 2.0$, $\frac{y}{D} = 2.0$ for amplitude level *3* ($\frac{A}{D} = 0.55$) within frequency regime *B*.

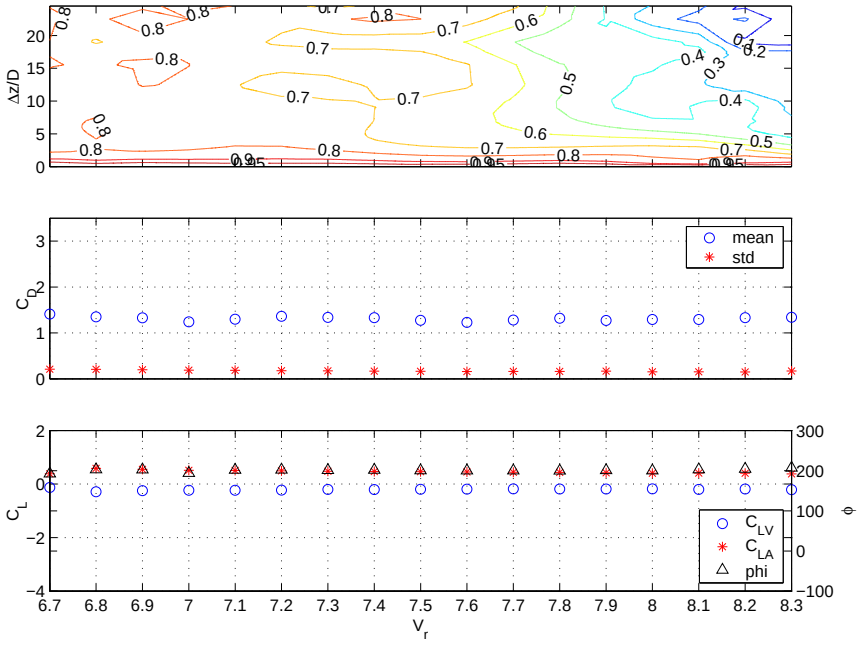

Figure 4-9: Summary of results outside the wake at $\frac{x}{D} = 2.0$, $\frac{y}{D} = 2.0$ for amplitude level *4* ($\frac{A}{D} = 0.65$) within frequency regime *B*.

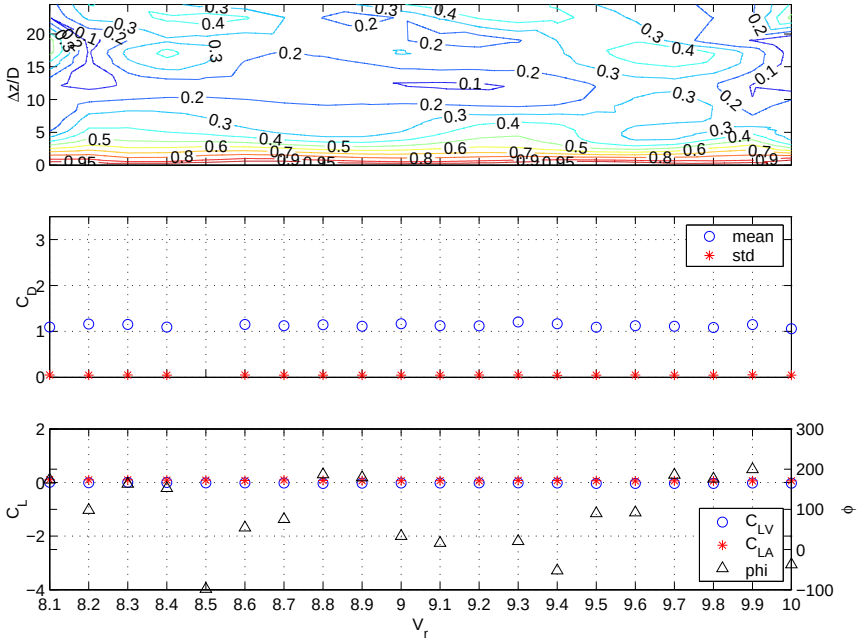

Figure 4-10: Summary of results outside the wake at $\frac{x}{D} = 2.0$, $\frac{y}{D} = 2.0$ for amplitude level *1* ($\frac{A}{D} = 0.1$) within frequency regime *C*.

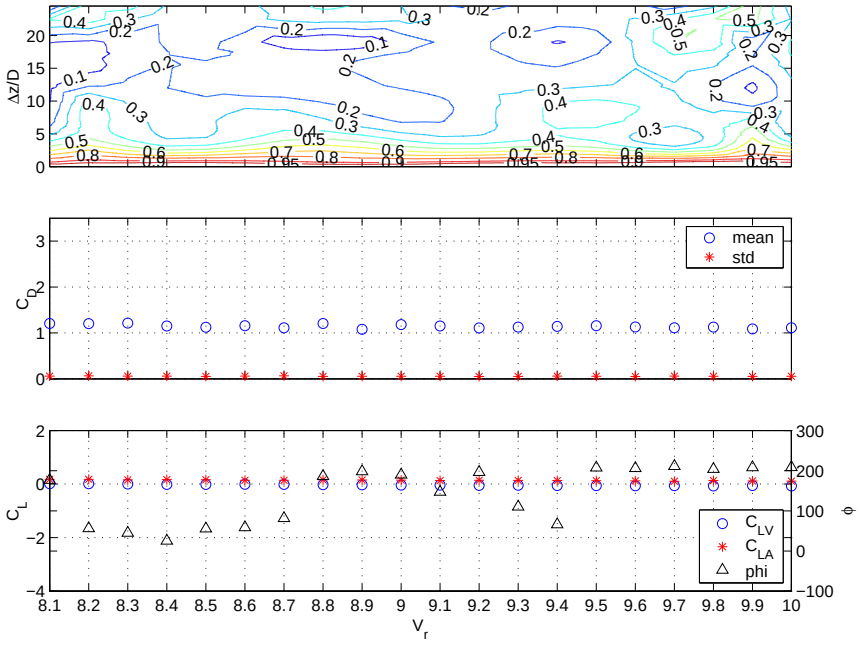

Figure 4-11: Summary of results outside the wake at $\frac{x}{D} = 2.0$, $\frac{y}{D} = 2.0$ for amplitude level *2* ($\frac{A}{D} = 0.2$) within frequency regime *C*.

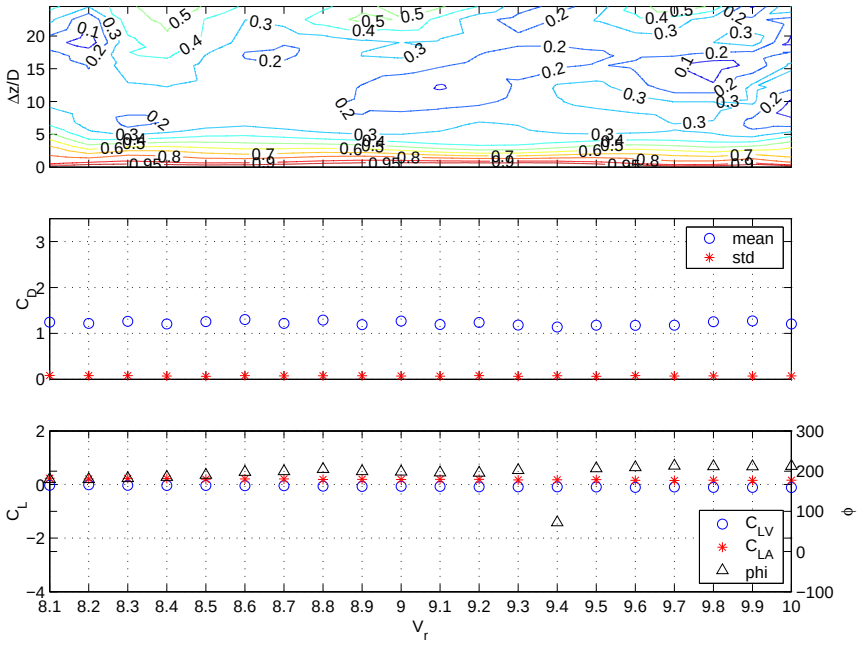

Figure 4-12: Summary of results outside the wake at $\frac{x}{D} = 2.0$, $\frac{y}{D} = 2.0$ for amplitude level *3* ($\frac{A}{D} = 0.3$) within frequency regime *C*.

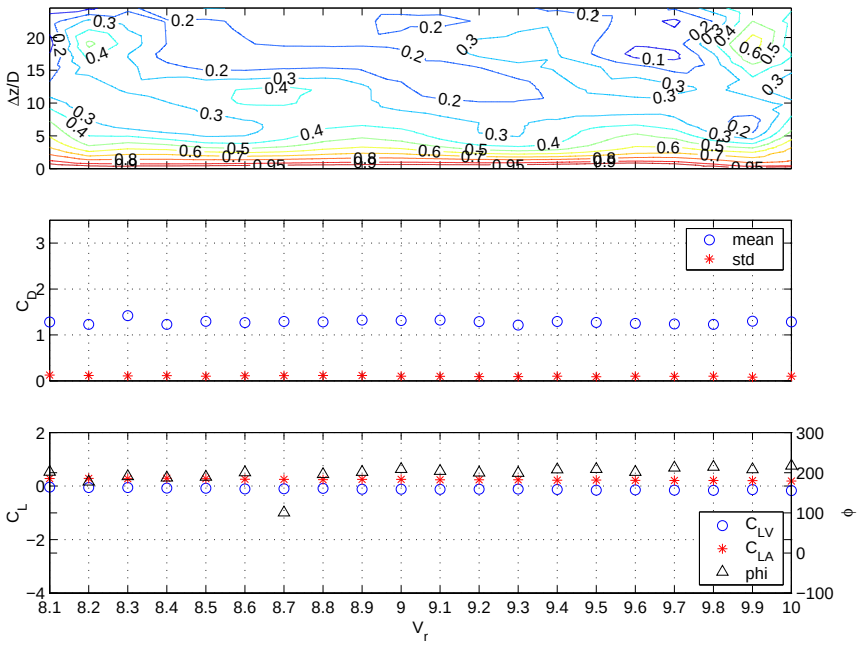

Figure 4-13: Summary of results outside the wake at $\frac{x}{D} = 2.0$, $\frac{y}{D} = 2.0$ for amplitude level *4* ($\frac{A}{D} = 0.4$) within frequency regime *C*.

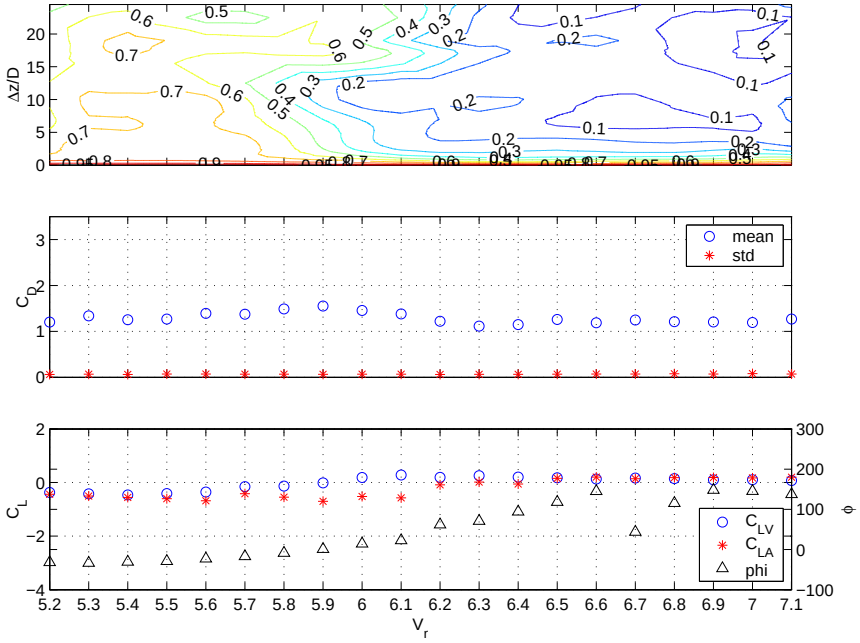

Figure 4-14: Summary of results within the wake at $\frac{x}{D} = 2.0$, $\frac{y}{D} = 0.5$ for amplitude level *1* ($\frac{A}{D} = 0.2$) within frequency regime A.

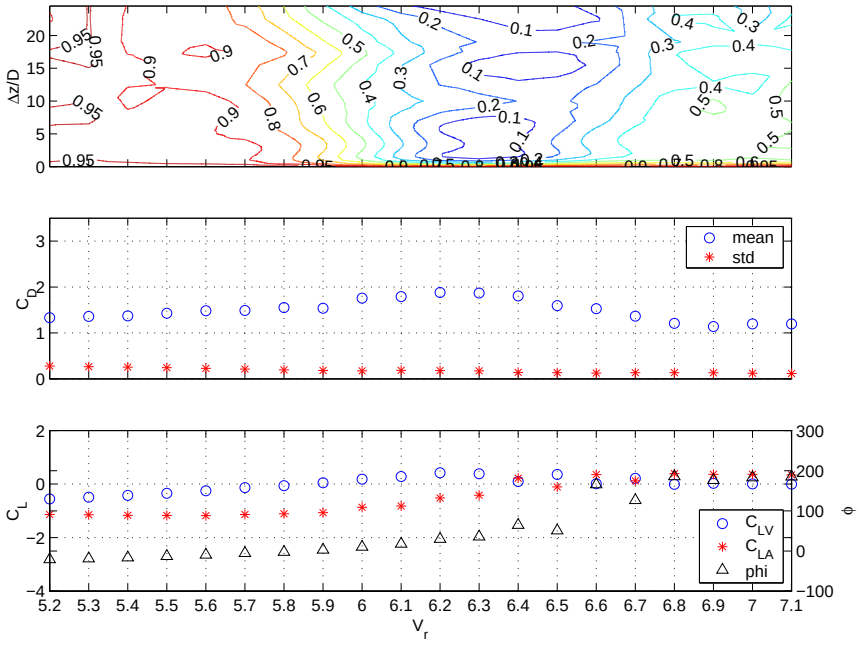

Figure 4-15: Summary of results within the wake at $\frac{x}{D} = 2.0$, $\frac{y}{D} = 0.5$ for amplitude level *2* ($\frac{A}{D} = 0.5$) within frequency regime A.

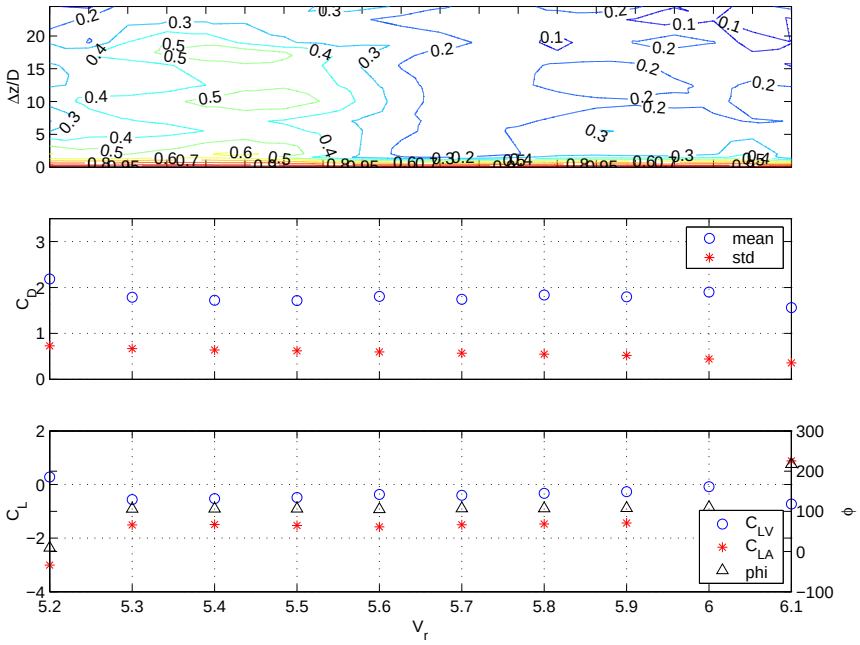

Figure 4-16: Summary of results within the wake at $\frac{x}{D} = 2.0$, $\frac{y}{D} = 0.5$ for amplitude level *3* ($\frac{A}{D} = 0.8$) within frequency regime A.

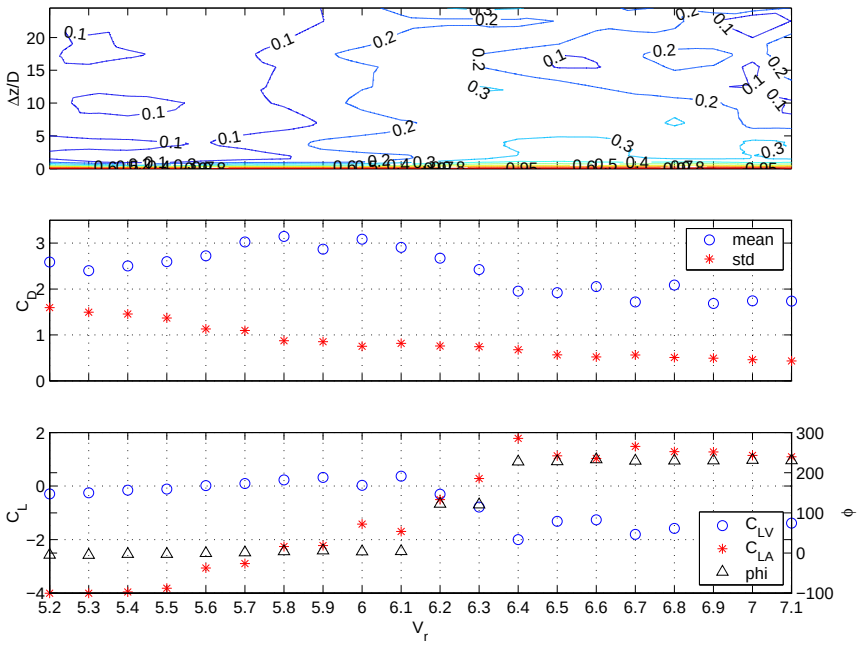

Figure 4-17: Summary of results within the wake at $\frac{x}{D} = 2.0$, $\frac{y}{D} = 0.5$ for amplitude level *4* ($\frac{A}{D} = 1.1$) within frequency regime A.

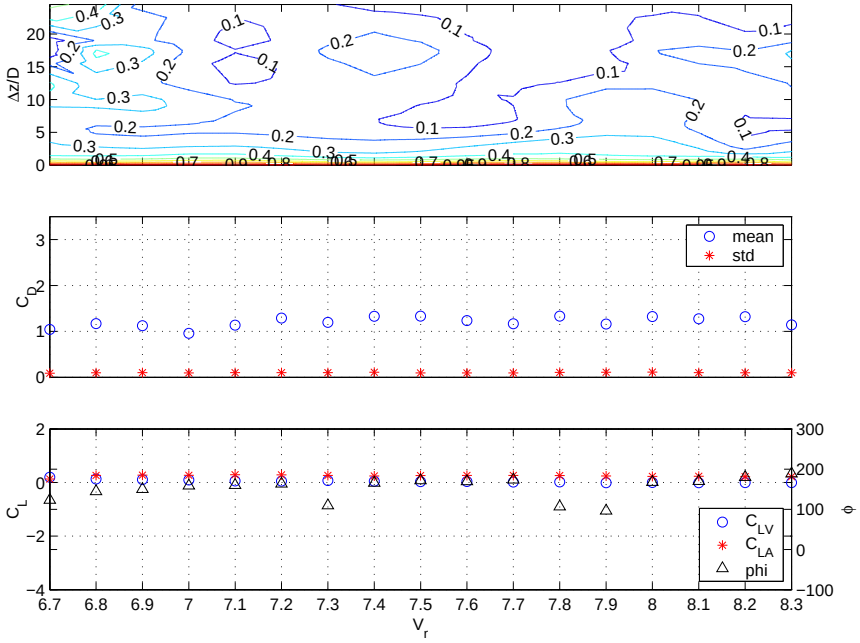

Figure 4-18: Summary of results within the wake at $\frac{x}{D} = 2.0$, $\frac{y}{D} = 0.5$ for amplitude level *1* ($\frac{A}{D} = 0.35$) within frequency regime *B*.

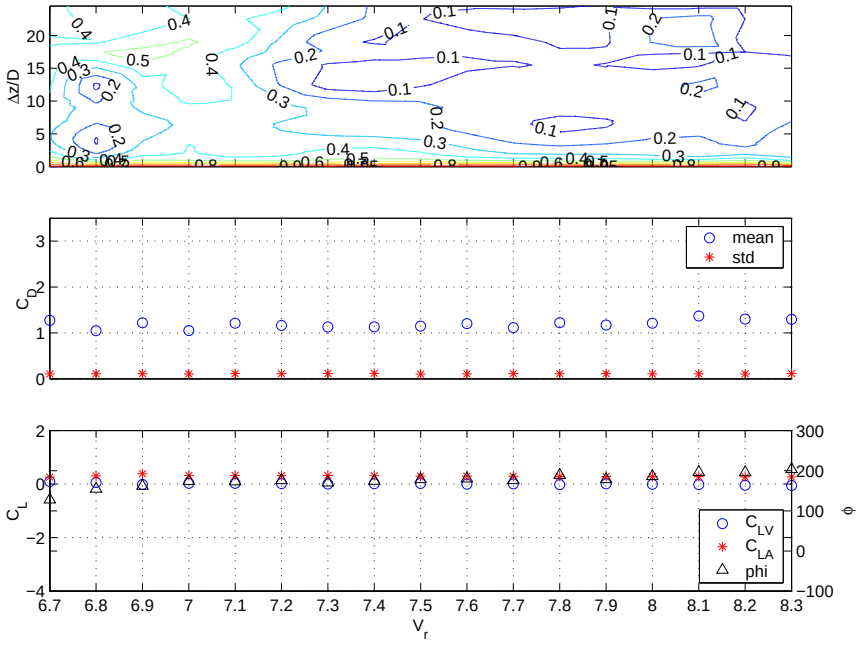

Figure 4-19: Summary of results within the wake at $\frac{x}{D} = 2.0$, $\frac{y}{D} = 0.5$ for amplitude level *2* ($\frac{A}{D} = 0.45$) within frequency regime *B*.

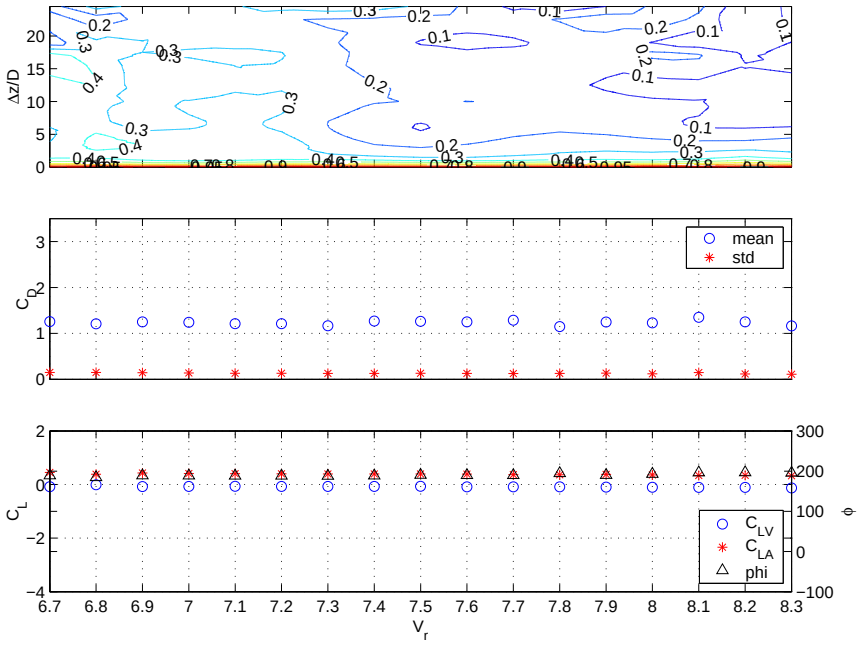

Figure 4-20: Summary of results within the wake at $\frac{x}{D} = 2.0$, $\frac{y}{D} = 0.5$ for amplitude level *3* ($\frac{A}{D} = 0.55$) within frequency regime *B*.

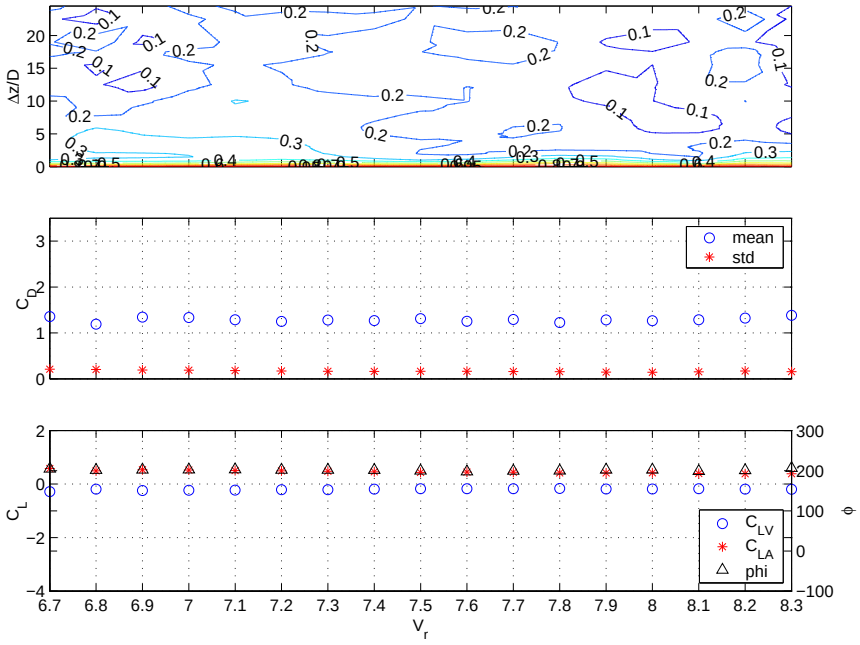

Figure 4-21: Summary of results within the wake at $\frac{x}{D} = 2.0$, $\frac{y}{D} = 0.5$ for amplitude level *4* ($\frac{A}{D} = 0.65$) within frequency regime *B*.

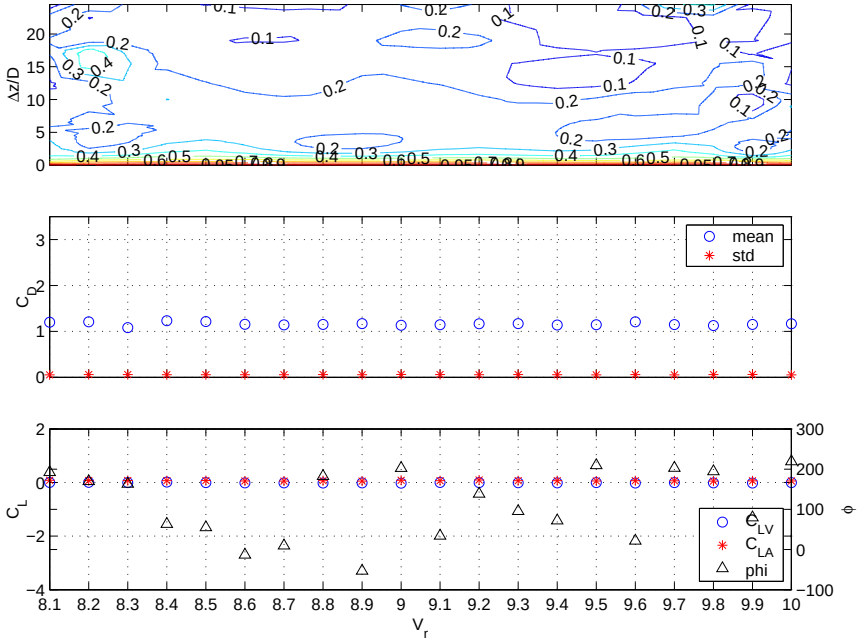

Figure 4-22: Summary of results within the wake at $\frac{x}{D} = 2.0$, $\frac{y}{D} = 0.5$ for amplitude level *1* ($\frac{A}{D} = 0.1$) within frequency regime *C*.

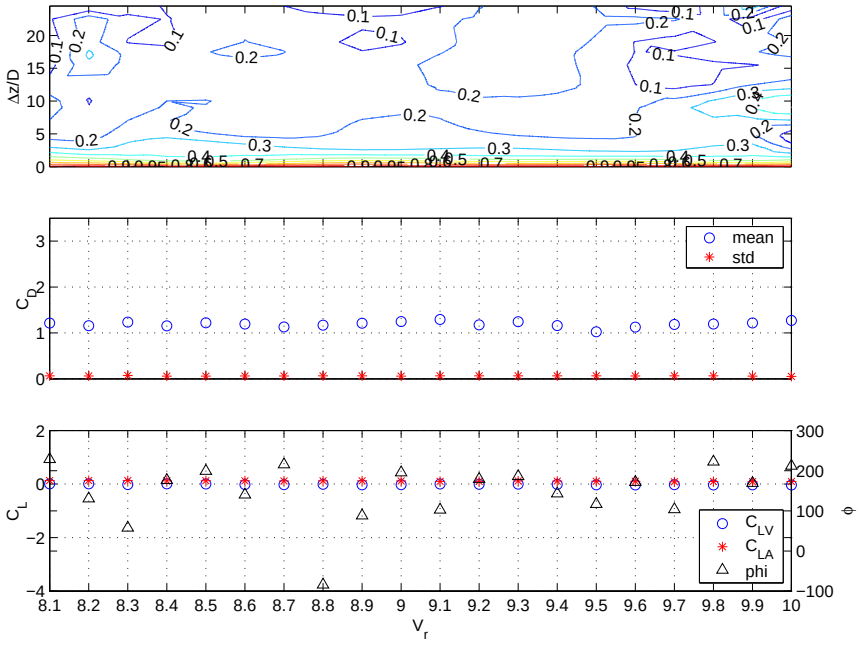

Figure 4-23: Summary of results within the wake at $\frac{x}{D} = 2.0$, $\frac{y}{D} = 0.5$ for amplitude level *2* ($\frac{A}{D} = 0.2$) within frequency regime *C*.

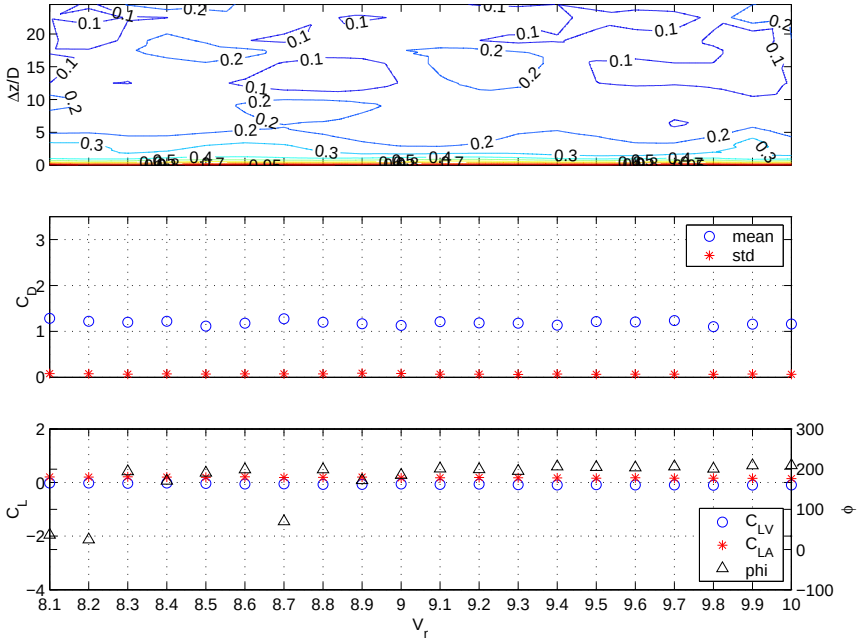

Figure 4-24: Summary of results within the wake at $\frac{x}{D} = 2.0$, $\frac{y}{D} = 0.5$ for amplitude level *3* ($\frac{A}{D} = 0.3$) within frequency regime *C*.

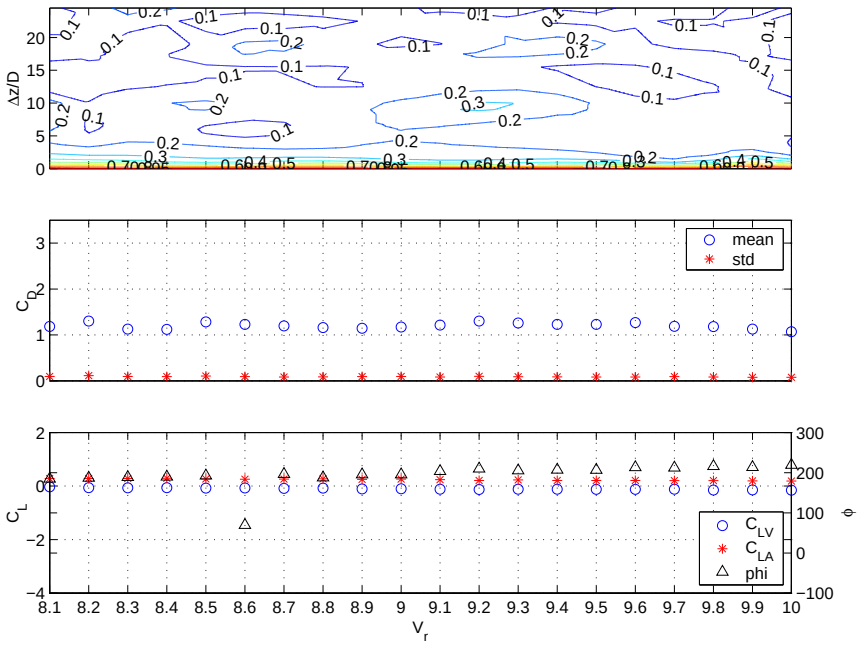

Figure 4-25: Summary of results within the wake at $\frac{x}{D} = 2.0$, $\frac{y}{D} = 0.5$ for amplitude level *4* ($\frac{A}{D} = 0.4$) within frequency regime *C*.

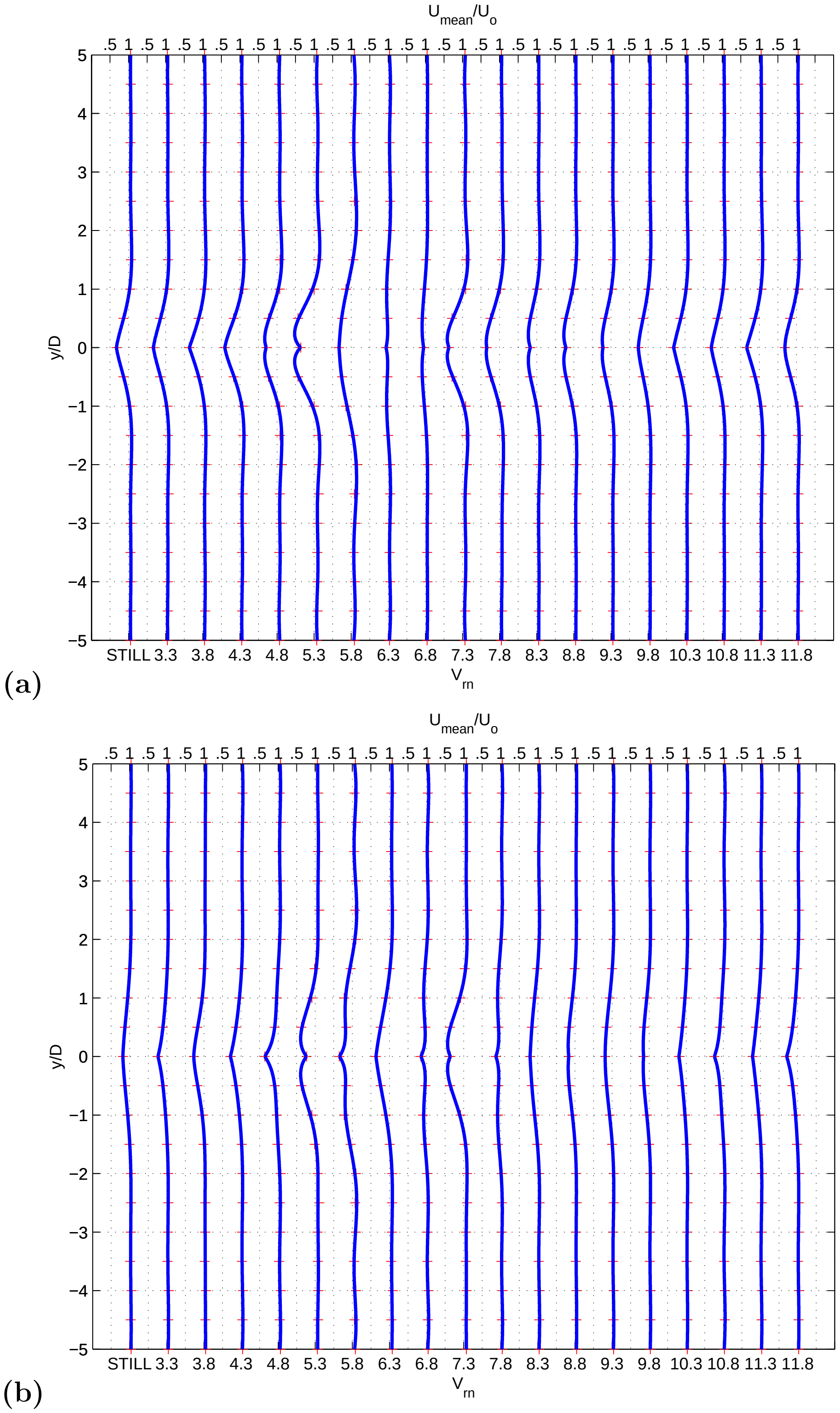

Figure 4-26: Mean velocity profile downstream of a cylinder experiencing forced vibration measured at (a)$\frac{x}{D} = 2$ and (b)$\frac{x}{D} = 5$.

Chapter 5

Conclusions

Experiments are performed in the MIT towing tank to investigate the spanwise velocity correlation and the velocity profile downstream of a vibrating cylinder. All experiments involve a Reynolds number of $Re = 30,480$. This study includes both free vibrations implemented through force feedback and forced vibrations. An array of constant temperature anemometers measures the instantaneous velocities downstream of the cylinder.

5.1 Error Analysis

Overall, the experimental results presented in this thesis are found to be repeatable and agree with theoretical predictions. Techniques, such as "wet" calibration of all sensors, are intended to reduce the level of systematic error. However, some potential sources of error exist in the experimental methods. None of these sources is believed to significantly affect the results. The conceivable causes and effects of experimental error are provided below.

- Misalignment or misplacement of the anemometer probes artificially decreasing or increasing velocity correlation coefficients.
- Possible inaccuracy in the carriage velocity control system resulting in faulty anemometer calibrations.

- Errors in the determination of force calibration coefficients affecting the accuracy of all force measurements.
- Oxidation formation on the surface of the test cylinder increasing roughness and thus the effective Reynolds number.
- Fouling of anemometer sensitive elements or temperature fluctuations in the fluid changing the measurement properties of one or more probes after calibration.
- Residual turbulence and vorticity from previous runs affecting the velocity correlation measurements.
- Accidental detection of the heaving foil strut/end plate wakes factitiously increasing correlation at large separation distances.

5.2 Primary Conclusions

In general, the findings of this thesis agree with previous research. Specifically, the trends of amplitude ratio, lift and drag coefficients, phase between displacement and force, and end force correlation follow those of Hover *et al.* [7] and others. Drawn from Chapters 3 and 4, this section provides a summary of the primary conclusions of the anemometer study that are unique to this study.

- In free vibration, the downstream velocity frequency doubles at a greater reduced nominal velocity than the 180° shift in phase angle between cylinder displacement and lift force. This inconsistency suggests that the 2P wake is not necessarily stable at the point of phase transition.
- As observed within the wake, forced motion produces more organized vortices with greater spanwise correlation than does free vibration.
- Full-span correlation lengths exist for both the 2S and the 2P vortex patterns at certain oscillation frequencies.

- The flow outside of the turbulent cylinder wake is more organized than that within.

- Large values of spanwise correlation coefficient coincide, roughly, with slightly negative values of C_{LV}, where energy flows from the structure to the fluid.

- Forced vibration results reveal the dependence of spanwise velocity correlation coefficient on motion amplitude and frequency. Flow correlated along the entire cylinder span occurs only within a certain amplitude and frequency threshold. Increased vibration amplitude can expand the range of oscillation frequencies characterized by highly correlated vortices. Specifically, amplitude ratios ranging $0.1 \leq \frac{A}{D} \leq 0.8$ and frequencies ranging from approximately 65% to 100% of the vortex shedding frequency of a stationary cylinder produce the greatest spanwise velocity correlation values. However, the upper limit of this frequency band is not explored in this study and may be larger.

- The deterioration of spanwise correlation at very high motion amplitudes contributes to the self-limiting nature of vortex-induced vibrations.

- In the case of a stationary cylinder, spanwise velocity correlation coefficient depends primarily on separation distance.

- Coherent phasing of vortex structures along the cylinder span is the mechanism that promotes largely two-dimensional flow to produce high values of velocity correlation coefficient.

- Because vortex shedding is periodic, cylinder oscillations change the geometry of the mean velocity profile only at large amplitudes.

5.3 Recommendations for Future Work

In addition to revealing the velocity characteristics downstream of an oscillating cylinder, this research raised several questions that are not presently addressed. This work shows the constant temperature anemometer to be a valuable tool in determining the fluid velocity at a specific point, but an instrument of limited utility in describing large scale phenomena. This section provides suggestions for future studies to further discover the subtleties of vortex-induced vibration.

- Employment of a cylinder with a greater aspect ratio would enable investigation of spanwise correlation at separation distances above the maximum theoretical correlation length of $\frac{L}{D} \approx 40$. Such an experiment would also reduce the effect of the foil strut wakes on correlation over large separations.

- Flow visualization techniques, such as dye injection and especially digital particle image velocimetry, can discern the three dimensional structure of shed vortices. These techniques could also implicitly determine the turbulent wake boundary and the vortex pattern.

- To fully define the oscillation frequency range resulting in well correlated downstream velocities, future studies should apply frequencies greater than the stationary shedding frequency (i.e. lower reduced velocities).

- Measurement at numerous downstream locations could reveal the evolution of spanwise correlation as vortices move away from the cylinder.

- Comparison of experimental results with numerical results from computation fluid dynamics would likely illustrate strengths and weaknesses of the experimental and theoretical approaches.

- A vertical anemometer rake with a finer resolution than that of the current study might show the velocity deficit with more detail.

Appendix A

Time Domain Examples

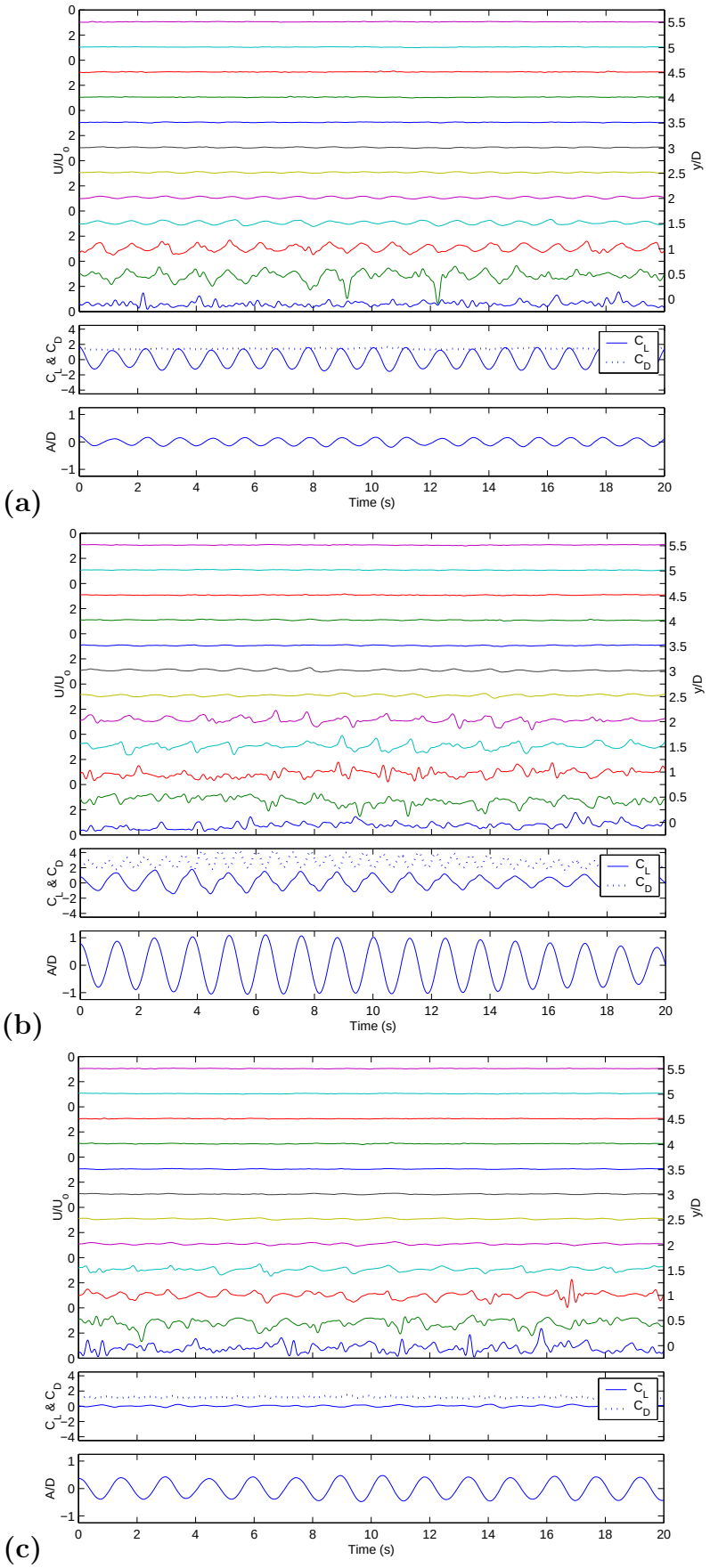

Figure A-1: Velocity profile at $\frac{x}{D} = 2$, lift and drag force, and cylinder displacement time histories for free vibration at (a)$V_{rn} = 3.8$, (b)$V_{rn} = 6.3$, and (c)$V_{rn} = 8.8$

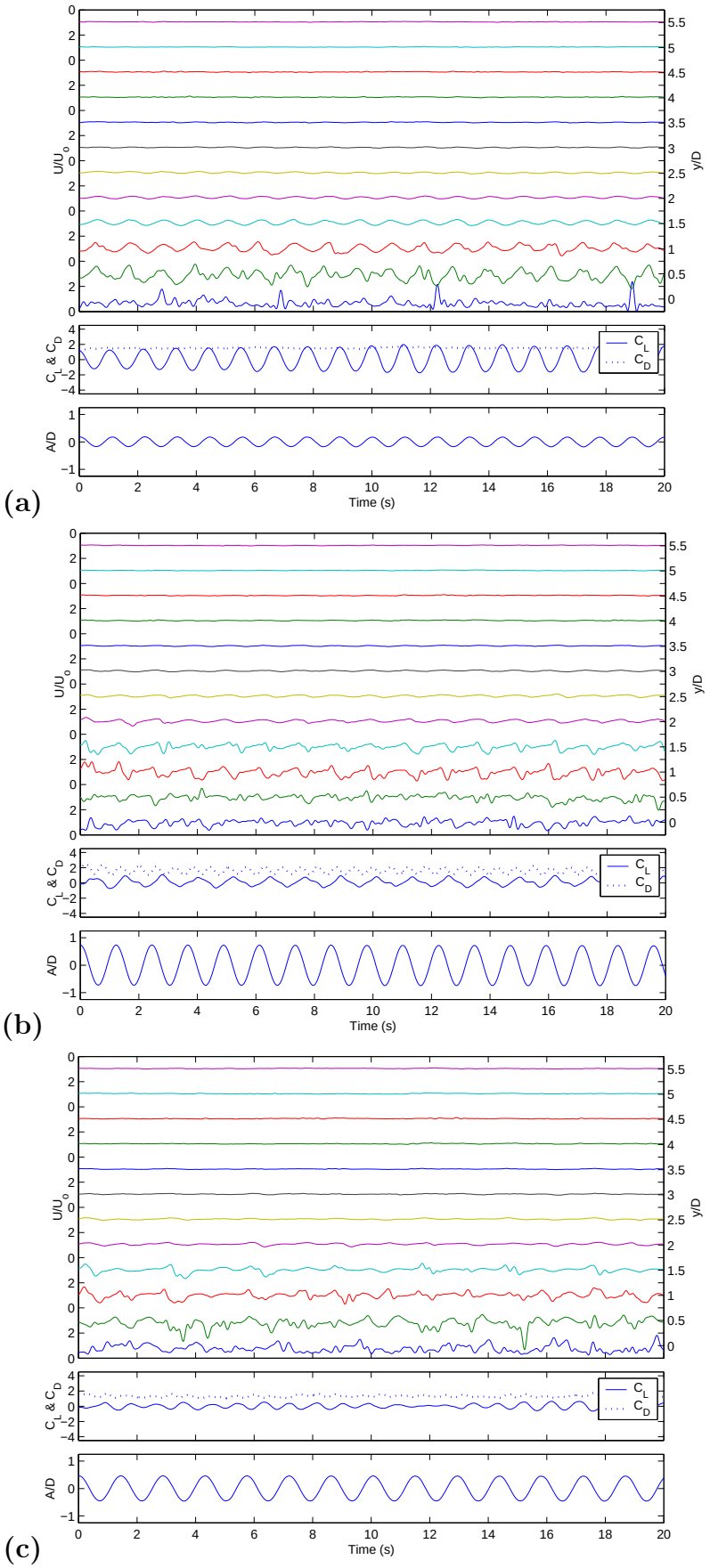

Figure A-2: Velocity profile at $\frac{x}{D} = 2$, lift and drag force, and cylinder displacement time histories for forced vibration at (a)$V_{rn} = 3.8$, (b)$V_{rn} = 6.3$, and (c)$V_{rn} = 8.8$

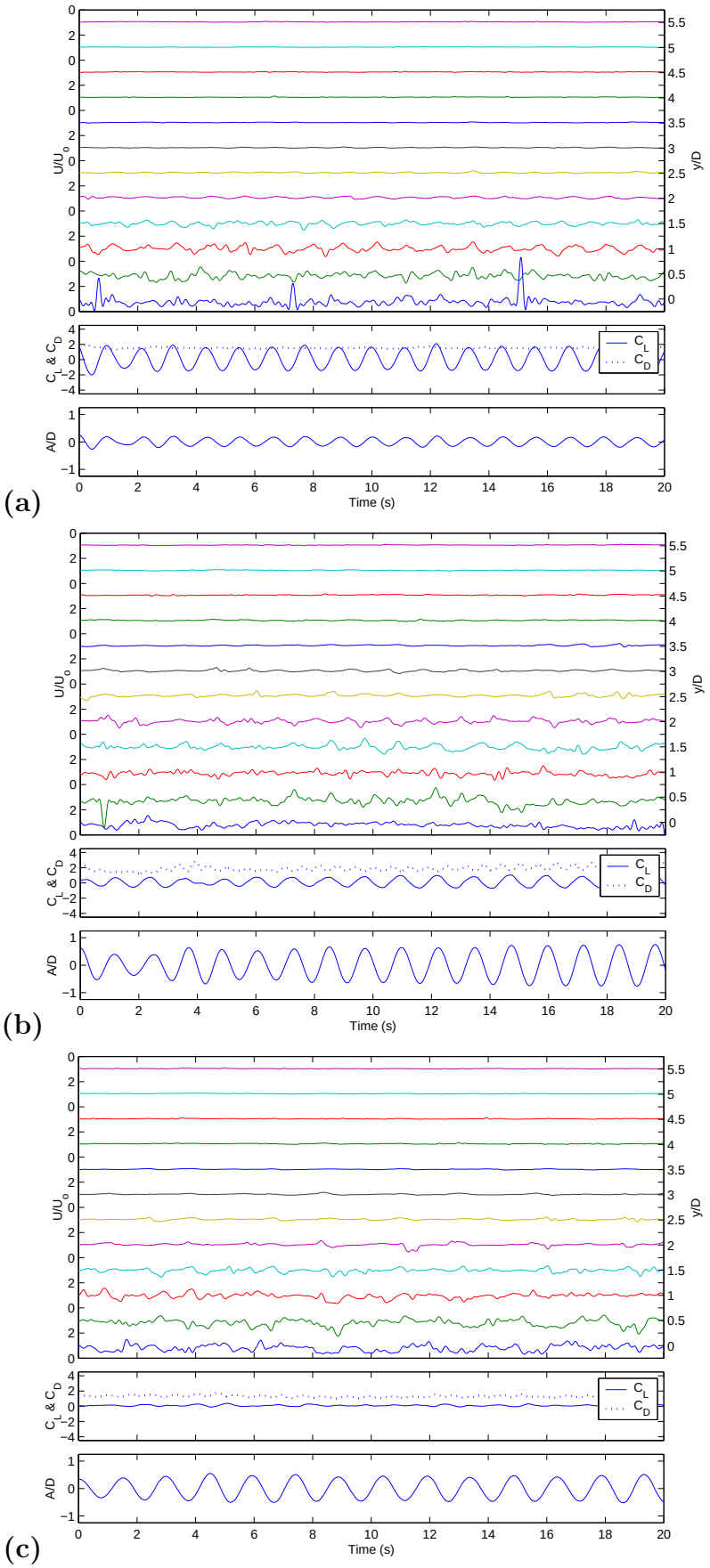

Figure A-3: Velocity profile at $\frac{x}{D} = 5$, lift and drag force, and cylinder displacement time histories for free vibration at (a)$V_{rn} = 3.8$, (b)$V_{rn} = 6.3$, and (c)$V_{rn} = 8.8$

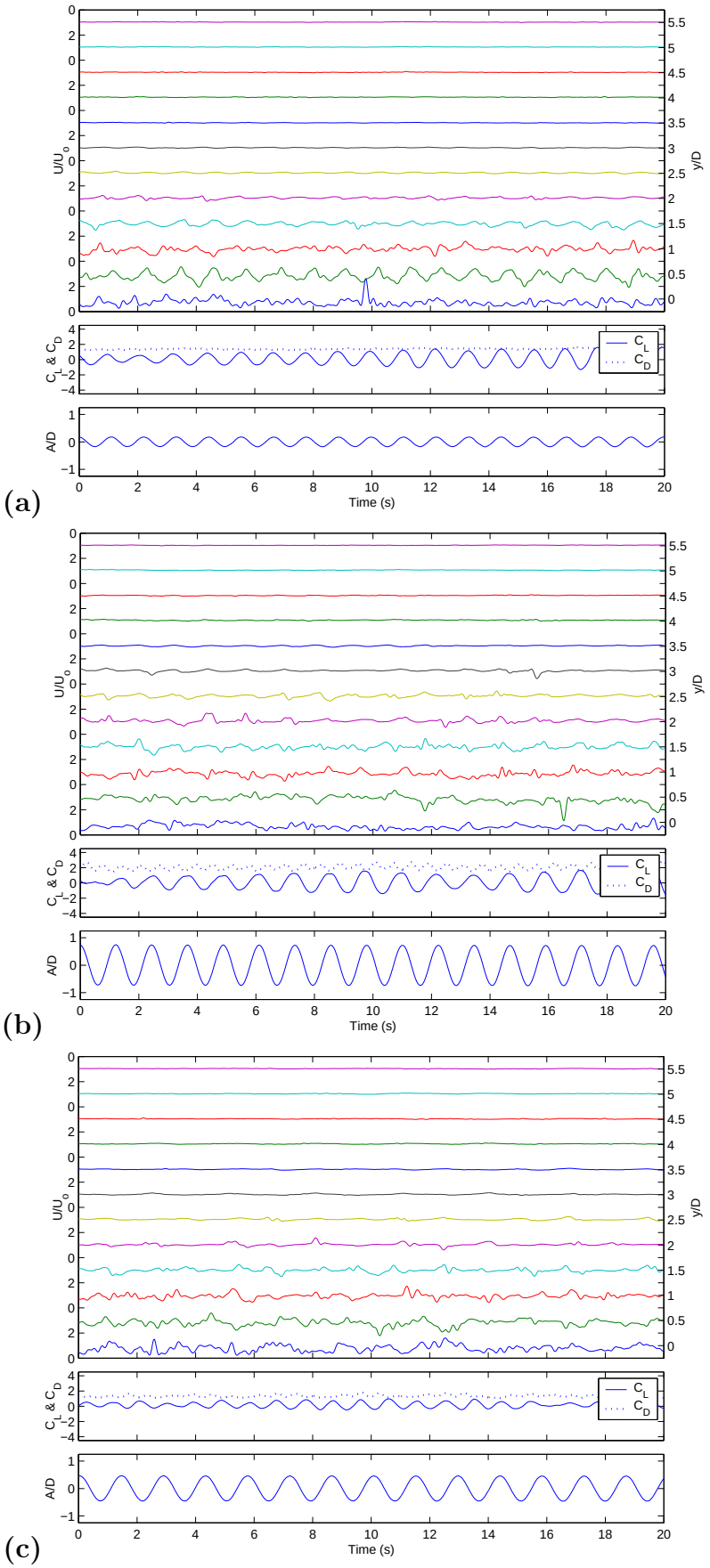

Figure A-4: Velocity profile at $\frac{x}{D} = 5$, lift and drag force, and cylinder displacement time histories for forced vibration at (a)$V_{rn} = 3.8$, (b)$V_{rn} = 6.3$, and (c)$V_{rn} = 8.8$

Appendix B

Frequency Domain Examples

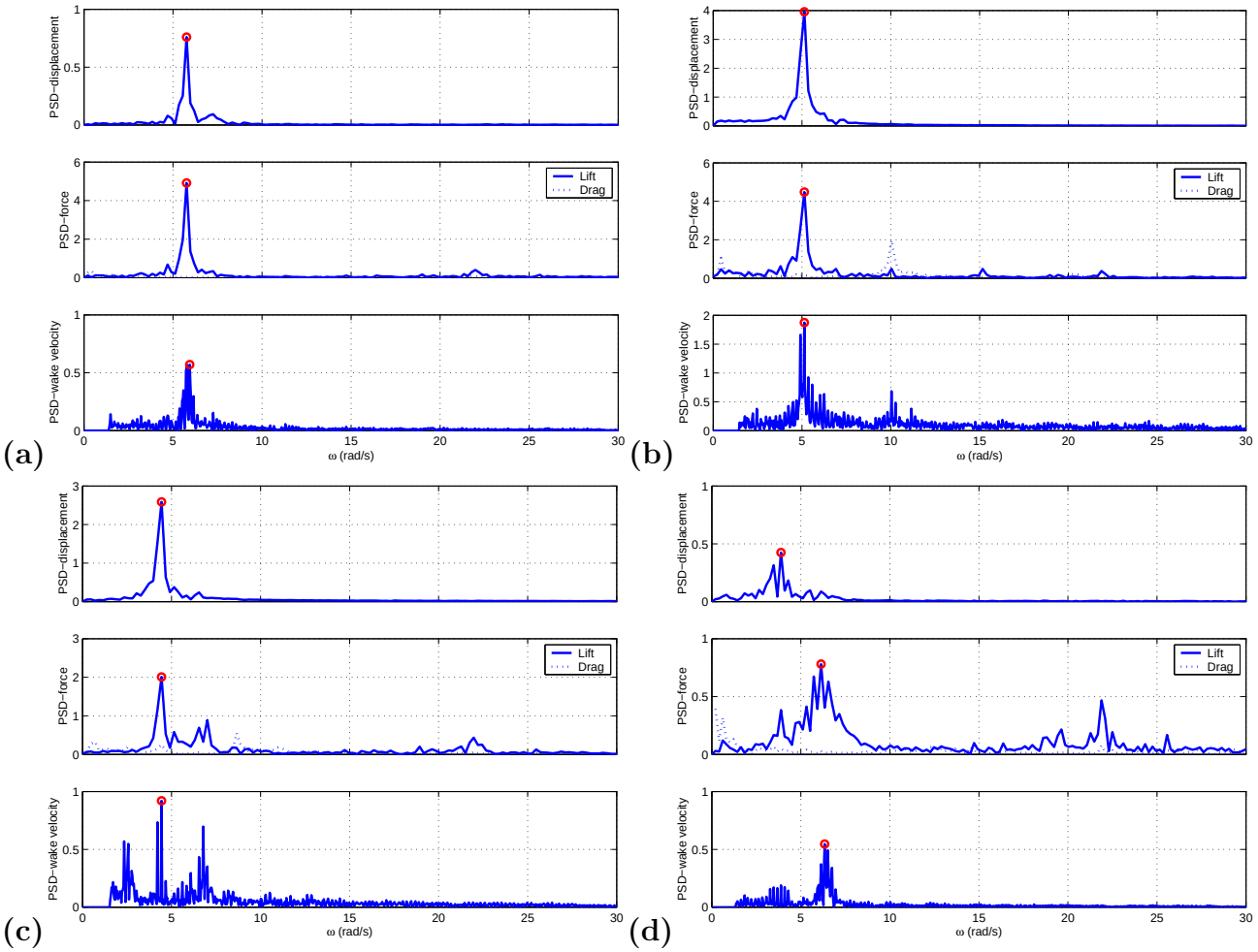

Figure B-1: Frequency spectra for cylinder oscillation, lift and drag force, and downstream velocity at $\frac{x}{D} = 2.0$, $\frac{y}{D} = 2.0$ for free vibrations at (a)$V_{rn} = 3.8$, (b)$V_{rn} = 6.3$, (c)$V_{rn} = 8.8$, and (d)$V_{rn} = 11.3$

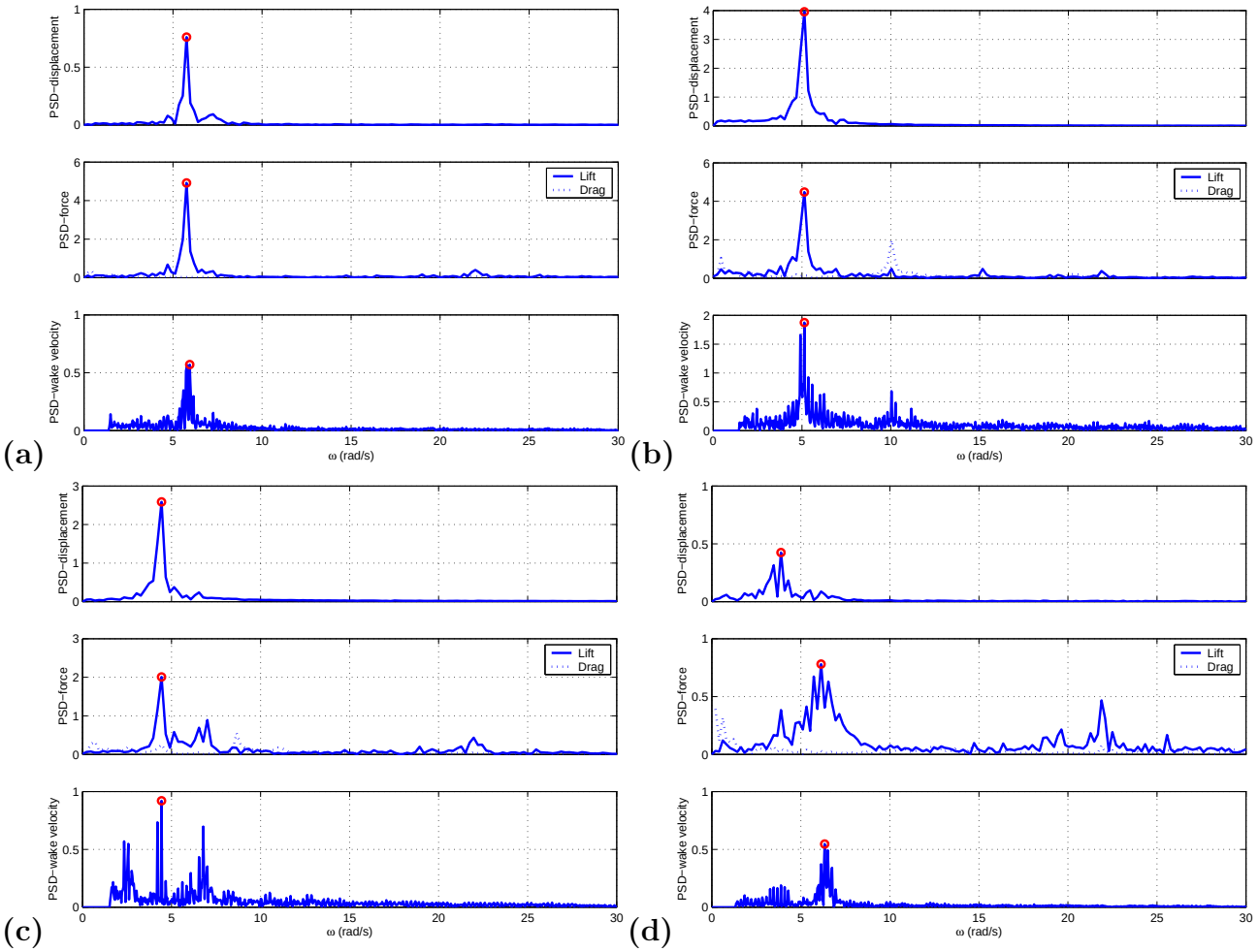

Figure B-2: Frequency spectra for cylinder oscillation, lift and drag force, and downstream velocity along the span at $\frac{x}{D} = 2.0$, $\frac{y}{D} = 2.0$ for forced vibrations corresponding to (a)$V_{rn} = 3.8$, (b)$V_{rn} = 6.3$, (c)$V_{rn} = 8.8$, and (d)$V_{rn} = 11.3$

Bibliography

[1] Robert D. Blevins. *Flow-Induced Vibration*. Krieger Publishing Company, Malabar, Florida, second edition, 1994.

[2] Brian Cantwell and Donald Coles. An experimental study of entrainment and transport in the turbulent near wake of a circular cylinder. *J. Fluid Mech.*, 136:321–374, 1983.

[3] Shoei-Sheng Chen. *Flow-induced vibration of circular cylindrical structures*. Hemisphere Pub. Corp., Washington, 1987.

[4] Ramnarayan Gopalkrishnan. *Vortex-Induced Forces on Oscillating Bluff Cylinders*. PhD thesis, Massachusetts Institute of Technology-WHOI, Department of Oceanographic Engineering, Feb 1993.

[5] H.L. Grant. The large eddies of turbulent motion. *J. Fluid Mech.*, 4:149–190, 1958.

[6] Michio Hayakawa and Fazle Hussain. Three-dimensionality of organized structures in a plane turbulent wake. *J. Fluid Mech.*, 206:375–404, 1989.

[7] F.S. Hover, S.N. Miller, and M.S. Triantafyllou. Vortex-induced vibration of marine cables: experiments using force feedback. *Journal of Fluids and Structures*, 11:307–326, 1997.

[8] F.S. Hover and M.S. Triantafyllou. Combined simulation with real-time forced feedback: A new tool for experimental fluid dynamics. In *System Theory: Modeling, Analysis, and Control*. Kluwer Academic Publishers, 1999.

[9] A. Kozakiewicz, B.M. Sumer, and J. Fredsøe. Spanwise correlation on a vibrating cylinder near a wall in oscillatory flows. *Journal of Fluids and Structures*, 6:371–392, 1992.

[10] Marcel Lefrancois and Boye Ahlborn. Enhancement of spanwise coherence in laminar vortex streets. *Phys. Fluids A*, 4(8):1851–1853, August 1992.

[11] The Math Works, Inc., Natick, MA. *Using Matlab*, fifth edition, 1999.

[12] A. Mukhopadhyay, P. Venugopal, and S.P. Vanka. Numerical study of vortex shedding from a circular cylinder in linear shear flow. Internet: http://www.mhpcc.edu/research/ab98/98ab01.html, September 1998.

[13] E.W. Nelson and J.A. Borgos. Dynamic response of conical and wedge type hot films: comparison of experimental and theoretical results. *TSI Quarterly*, 9(1):3–7, Jan-Mar 1983.

[14] J.N. Newman. *Marine Hydrodynamics*. MIT Press, Cambridge, Massachusetts, 1977.

[15] M. Novak and H. Tanaka. Pressure correlations on a vibrating cylinder. In K.J. Eaton, editor, *Proc. 4th Int. Conf. on Wind Effects on Buildings and Strucures*, pages 227–232, Heathrow, 1977. Cambridge University Press.

[16] A.E. Perry, M.S. Chong, and T.T. Lim. The vortex-shedding process behind two-dimensional bluff bodies. *J. Fluid Mech.*, 116:77–09, 1982.

[17] S.E. Ramberg and O.M Griffin. Velocity correlation and vortex spacing in the wake of a vibrating cable. *Journal of Fluids Engineering*, 98:10–18, March 1976.

[18] T. Sarpkaya. Vortex-induced oscillations: A selective review. *Journal of Applied Mechanics*, 46:241–258, 1979.

[19] B.M. Sumer, J. Fredsøe, and K. Jensen. A note on spanwise correlation on a freely vibrating cylinder in oscillaroty flow. *Journal of Fluids Engineering*, 8:231–238, 1994.

[20] Stefan Szepessy. On the spanwise correlation of vortex shedding from a circular cylinder at high subcritical reynolds number. *Phys. Fluids*, 6(7):2406–2416, July 1994.

[21] G.H. Toebes. The unsteady flow and wake near an oscillating cylinder. *Journal of Basic Engineering*, 91:493–505, September 1969.

[22] M.S. Triantafyllou. Vortex-indeuced vibrations and drag amplification in shear flow. tutorial paper, Department of Ocean Engineering, MIT, 1991.

[23] Frank M. White. *Fluid Mechanics*. McGraw-Hill, Inc., New York, 1986.

[24] C.H.K. Williamson. Vortex dynamics in the cylinder wake. *Annu. Rev. Fluid. Mech.*, 28:477–539, 1996.

[25] C.H.K. Williamson and A. Roshko. Vortex formation in the wake of an oscillating cylinder. *Journal of Fluids and Structures*, 2:355–381, 1988.

[26] J. Wu et al. Spanwise wake structures of a circular cylinder and two circular cyinders in tandem. *Experimental Thermal and Fluid Science*, 9:299–308, 1994.